A Flexible Micro Fuel Cell Fabricated using a Hybrid Fabrication Technique

by

Kevin G. Stanley
B.A.Sc. Simon Fraser University, 1997
M.A.Sc. Simon Fraser University, 1999

THESIS
SUBMITTED IN PARTIAL FULFILLMENT OF
THE REQUIREMENTS FOR THE DEGREE OF

DOCTOR OF PHILOSOPHY

In the
School of
Engineering Science

SIMON FRASER UNIVERSITY

Fall 2005

Approval

Name:	**Kevin G. Stanley**
Degree:	**Doctor of Philosophy in Engineering Science**
Title of Thesis:	**A Flexible Micro Fuel Cell Fabricated Using a Hybrid Fabrication Technique**

Examining Committee:

Chair: Dr. Shawn Stapleton
Professor, School of Engineering Science, Simon Fraser University

---

Dr. Ash M. Parameswaran
Senior Supervisor
Professor, School of Engineering Science, Simon Fraser University

---

Dr. William A. Gruver
Senior Supervisor
Professor, School of Engineering Science, Simon Fraser University

---

Dr. Marek Syrzycki
Supervisor
Professor, School of Engineering Science, Simon Fraser University

---

Dr. Steven Holdcroft
Supervisor
Professor, Department of Chemistry, Simon Fraser University

Dr. Q.M. Jonathan Wu
Supervisor
Associate Professor, School of Engineering Science, University of Windsor

---

Dr. Bonnie Gray
Internal Examiner
Assistant Professor, School of Engineering Science, Simon Fraser University

---

Dr. Karan V.I.S. Kaler
External Examiner
Professor, Department of Electrical and Computer Engineering
University of Calgary

Date Defended: Dec. 02/05

Abstract

Micro fuel cells are currently being investigated as replacement for both primary and secondary batteries. While many technological challenges remain in micro fuel cell research, the key issue for all micro fuel cells is the volume of the system. While significant advances have been made in reducing the number and size of required components, the cell itself is difficult to miniaturize. Many researchers have attempted to apply different variants of micro fabrication techniques to the fabrication of micro fuel cells. We have elected to pursue an unusual inside-out architecture, where the membrane is used as a substrate, and thick and thin film depositions are used to create the active layers of the cell itself. By using a combination of analytical and finite element analysis techniques, we were able to derive practical values for critical parameters including: the hydraulic diameter; electrode length; gas diffusion layer conductivity and porosity; and operating temperature of the fuel cell with respect to the environment. These values were used to create a new fuel cell fabrication technique and architecture, which used a hybrid fabrication technique where the tool and die were fabricated using micro fabrication techniques, but the cell itself was fabricated using traditional manufacturing techniques. To successfully fabricate these designs, a new stable supported membrane, and a particle based castable diffusion layer were required. These new materials had unusual mechanical properties, as well as their desired electrochemical properties. Testing the cell we found performance significantly lower than predicted. We traced the performance shortfall to a lower than required cathode GDL conductivity and porosity. Significant advances in GDL material design will be required to maximize the potential of the cell architecture.

Keywords:

MEMS, micro fuel cell, fabrication, modeling, proton exchange membrane

To my wife Regan,

for the rapid foot-based posterior encouragement

which set me on this path. I couldn't have done this without you.

Acknowledgements

I must thank many people for their contributions to this work. First, I must thank my committee for their encouragement throughout the process. I must thank Jonathan Wu in particular for encouraging me to pursue a PhD while working at NRC, and Ash Parameswaran and William Gruver for their patients in dealing with this unusual circumstance. I must recognize the contributions of Titichai Navessin, Ken Shi, Zhong Xie, and Robert Chow of the MEA group at NRC-IFCI for all their help in materials processing and fuel cell characterization. I would also like to thank Simon Liu, Datong Song and Qianpu Wang of the Modeling Group at NRC for their help in designing the FEA model. Mike must be recognized for editing above and beyond the call of duty. I would like to recognize the coop students I have worked with over the years, Zoë, Jodie, Joel, Lillian, and Keith for their help in the lab. Tom Vanderhoek, Francois Girard and Terrance Wong must be acknowledged for their consultation on the fuel cell architecture. Yanghua and Hengbing deserve recognition for their excellent ping-pong tutelage. Finally, I must extend my heartfelt thanks to Eva Czyzewska who has worked with me on this project from the beginning, and whose knowledge, skill and sense of humor have been critical to its success.

Table of Contents

List of Figures

List of Tables

List of Acronyms

AC	Alternating current
BOP	Balance of plant
CFD	Computational fluid dynamics
CV	Cyclic voltametry
CVD	Chemical vapor deposition
DI	Deionized
DMF	N,N-Dimethylformamide
DMFC	Direct methanol fuel cell
DRIE	Deep reactive ion etching
EDP	Ethylene Diamine Pyrocatechol
FEA	Finite element analysis
FEM	Finite element modeling
GDE	Gas diffusion electrode
GDL	Gas diffusion layer
MEA	Membrane electrode assembly
MEMS	Micro electro mechanical systems
NRC-IFCI	National Research Council of Canada Institute for Fuel Cell Innovation
OCV	Open circuit voltage
PCB	Printed circuit board
PDMS	Polydimethyl siloxane
PEM	Polymer electrolyte membrane
PEM	Proton exchange membrane
PFSI	Polyfluorosulfonated ionomer
PMMA	poly(methyl methacrylate)
PTFE	Polytetrafluoro ethylene
RH	Relative humidity
SBS	Styrene-butadiene-styrene
SEBS	Polystyrene-block-(polyethylene-ran-butylene)-block-polystyrene
SEM	Scanning electron microscope
SOFFC	Solid oxide fuel cell
SSC	Short circuit current
TMAH	Tetramethyl ammonium hydroxide
UV	Ultra violet

List of Symbols

Symbols

A	Area
c	Concentration
C_d	Drag coefficient
C_s	Surface tension coefficient
D	Diameter
D	Diffusion coefficient
D_h	Hydraulic diameter
D^K	Knudsen diffusion coefficient
d_m	Molecular diameter
F	Faraday's constant
F	Force
G	Flux
h	Height
I	Current
i_d	Current density
i_o	Exchange current density
k	Stoichiometric constant
K	Fluidic constant
k	Thermal conductivity
Kn	Knudsen Number
M	Molar mass
Ma	Mach Number
n	Number of moles
N_{cells}	Number of cells
P	Power
P	Pressure
p	Pressure
P_c	Contact length
Q	Charge
Q	Heat
Q_j	Current source
R	Gas constant
r	Radius

R	Reaction rate
R	Electrical resistance
Re	Reynolds Number
S	Enthalpy
S_c	Catalyst surface area
t	Time
T	Temperature
t	Thickness
u	Fluid velocity
V	Electrical Potential
v	Volume
w	Width

Greek Symbols

ρ	Density
μ	Viscosity
λ	Mean free path
σ_a	Accommodation coefficient
σ_m	Tangential accommodation coefficient
σ	Surface Tension
σ	Electrical conductivity
θ	Angle
γ	Reaction order
α	Reaction constant
σ_s	Stress
ε	Strain

Subscripts

a	Anode
av	Average
c	Cathode
c	Current collector
cat	Catalyst
d	Drag
eff	Effective
GDL	Gas diffusion layer
i	Input
m	Membrane
max	Maximum
MeOH	Methanol
Naf	Nafion
o	Operating
o	Output
q	Quiescent
r	Required
ref	Reference
s	Surface
SAT	Saturation
TF	Thin film

Chapter 1 Background and Problem Description

1.1 Introduction

Fuel cells are electrochemical reactors that directly generate electrical power through the controlled combustion of hydrogen or light hydrocarbons. A fuel cell creates a potential difference by separating the net reaction into two electrochemical half reactions, the oxidation of hydrogen or hydrocarbons and the reduction of protons in the presence of oxygen to create water.

Fuel cells were first discovered by William Grove in 1839, but they remained a scientific curiosity for over 50 years until the advent of the space program [1]. Because fuel cells are much lighter than batteries, and run on hydrogen fuel, their first practical application was in the Apollo orbiter. These fuel cells were based on an alkaline electrolyte, and used excessively high precious metal catalyst loadings. The material cost and lifetime of these fuel cells prevented them from moving beyond space exploration [1].

Recently, advances in materials have lead to a renaissance in fuel cell research [1]. Fuel cells have received significant attention from both researchers and industry because of the potential for clean electrical energy generated directly from the reduction of hydrogen or hydrogen bearing compounds. Lower catalyst loadings, new solid-state electrolytes and better architectures have moved fuel cells closer to industrial applications. Several competing fuel cell technologies have emerged, supplanting the alkaline, phosphoric acid and molten carbonate systems common during the early program [1]. At the present time there are two primary fuel cell technologies: proton exchange membrane (PEM) fuel cells and solid oxide fuel cells (SOFC). PEM fuel cells operate at moderate temperatures of between 20 and 120 C, and are based on solid-state polymer electrolytes. SOFCs operate at much higher

temperatures 600 to 1200 C and use solid-state ceramic membranes. Both fuel cells operate within a range of physical size, power output, and preferred fuel. Output powers from milliwatts to hundreds of kilowatts have been reported for both fuel cell architectures [1].

Although the preferred fuel for both fuel cell architectures is hydrogen, other hydrogen bearing fuel sources have been demonstrated. Almost all hydrocarbon fuels found in the petrochemical industry can be used in a fuel cell system in conjunction with a fuel reformer, which strips hydrogen molecules from the fuel prior to entering the fuel cell. Two hydrocarbon fuels, methanol and methane, can be directly reformed within the fuel cell itself. Methane can only be directly used in an SOFC because higher energy is required to break a stable hydrogen-carbon bond. For most micro fuel cell applications, PEM fuel cells are preferred over SOFCs because of their lower operating temperature.

1.1.1 PEM Fuel Cell Overview

Proton exchange membrane (PEM) fuel cells are characterized by an ion or proton conducting membrane separating the two half reactions. This membrane is permeable to positive ions, preferably only protons, and is impervious to liquids and gasses. PEM fuel cells are usually built around a polymer membrane such as Nafion from DuPont as shown in the schematic cross section Figure 1.

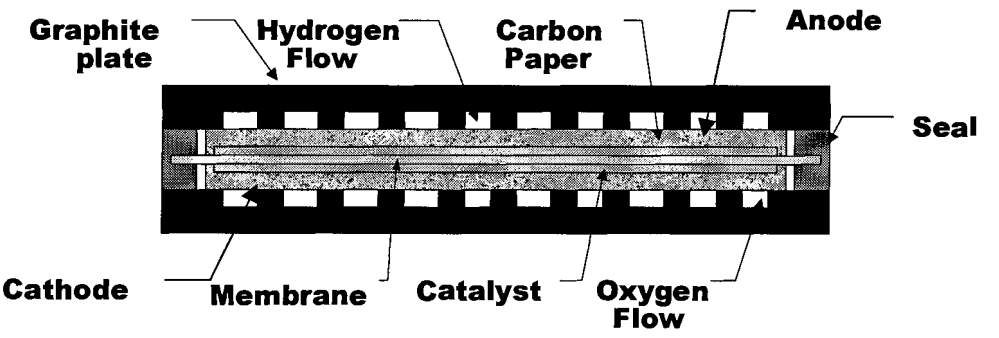

Figure 1: Standard PEM fuel cell structure in cross-section

The fuel and oxidant are routed through the fuel cell in a flow field usually made of graphite, although stainless steel or plastic flow fields have also been investigated. For bipolar fuel cell stacks, electrons are collected in the graphite plate and transported from the anode to the cathode within the stack, connecting the cells of the stack in series. In this case the flow field is referred to as a bipolar plate. In this thesis, we will use the term bipolar to refer to any architecture where electrons are conducted through the bulk of the flow field in a primarily vertical direction as opposed to laterally along the surface of the flow field towards the edges.

The active portion of a PEM fuel cell is known as the membrane electrode assembly (MEA) and is comprised of a gas diffusion layer (GDL), a catalyst layer and an electrolyte. The gas diffusion layer is usually a carbon cloth or felt. Fuel or oxidant diffuses through the pores in the layer, and electrons are conducted through the solid fibers. The catalyst in PEM fuel cells is usually nanoparticulate noble metals deposited on a high surface area carbon support. The membrane is a solid-state polymer, usually Nafion from DuPont, which is a perfluorosulphonic acid polymer, a Teflon backbone with sulfonal acid groups. Nafion is gas-impermeable but conductive to cations. The catalyst layer itself is a composite of the catalyst, the ion conducting polymer, and micropores, forming a three-phase interface where fuel or oxidant can enter, and protons, electrons and chemical products can leave. A conceptual diagram of the catalyst layer is shown in Figure 2.

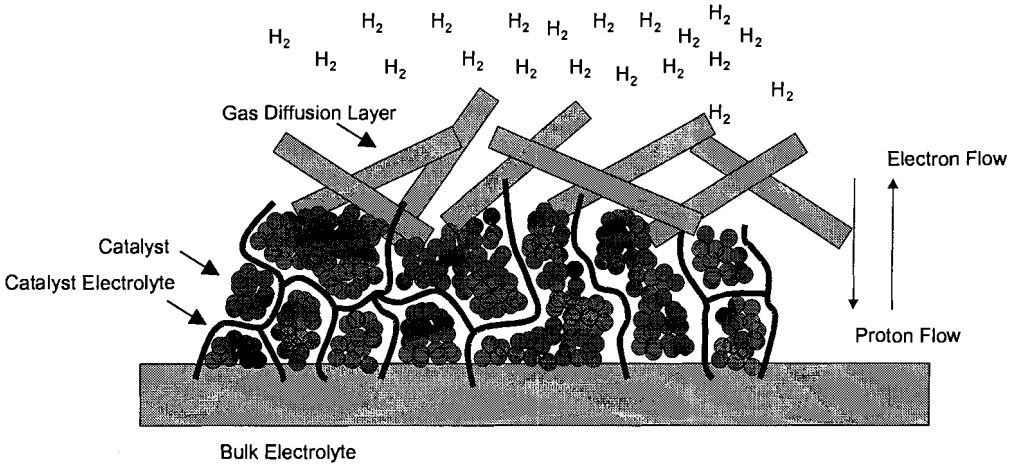

Figure 2: Conceptual diagram of a fuel cell active region

In Figure 2, the catalyst agglomerates are represented by the superimposed circles, the ion conducting channels by the solid black lines, and the tips of the carbon fibers with the solid grey boxes. Hydrogen diffuses through the catalyst layer, primarily through the larger pores between catalyst agglomerates, until it adsorbs onto a catalyst surface and is reduced to electrons and protons. Ion transport occurs through the bulk electrolyte ionomer dispersed throughout the catalyst. Electrons transfer from agglomerate to agglomerate until the bulk collectors of the GDL are reached. Proton and electron flow are illustrated in the right hand side of Figure 2. Proper fabrication and modification of this electrode structure are crucial to successful micro fuel cell design.

The formation of the three-phase interface is critically important for proper operation of the fuel cell. These phases are: gaseous, maintained through the pores; aqueous, maintained through the electrolyte; and solid conductivity, maintained through the carbon. Absence of any of these phases results in decreased fuel cell performance. Because fabrication techniques are empirical rather than derivative, realizing a practical of the three-phase interface is more of

an art than a science. The techniques used to fabricate the fuel cell presented in this thesis are presented in chapter 3.

Pathways for all three phases must be maintained during fuel cell operation as well as during fabrication. Water management in particularly important because insufficient water increases the impedance of the electrolyte layer to prohibitively large values, and an excess of water fills the micropores in the catalyst layer with liquid water, eliminating the path for gas transport. Details of micro fuel cell design for water management are presented in chapter 2.

Fuel cell performance operation and performance is characterized by three key operating regimes and is denoted by the dominant loss mechanism in that regime. A polarization curve depicting voltage loss versus current is typically used to denote the performance of the fuel cell. The first regime is called the kinetic region, and includes losses due to chemical processes such as fuel crossover, electrode kinetics, and activation losses. The kinetic region gives rise to the difference between the theoretical and practical open circuit voltage (OCV) for the cell. The second operating regime is known as the Ohmic or linear region. Kinetic losses decay exponentially, so at a sufficient current density the kinetic loss can be regarded as constant. At higher current densities, Ohmic drops due to the conduction of protons and electrons from anode to cathode become significant. With additional current density, reactants cannot reach the catalytic sites quickly enough, and mass transport limitations begin to dominate. The point where the potential is minimum and current maximum is called the short circuit current (SCC). An example polarization curve with each operating regime notated is shown Figure 3.

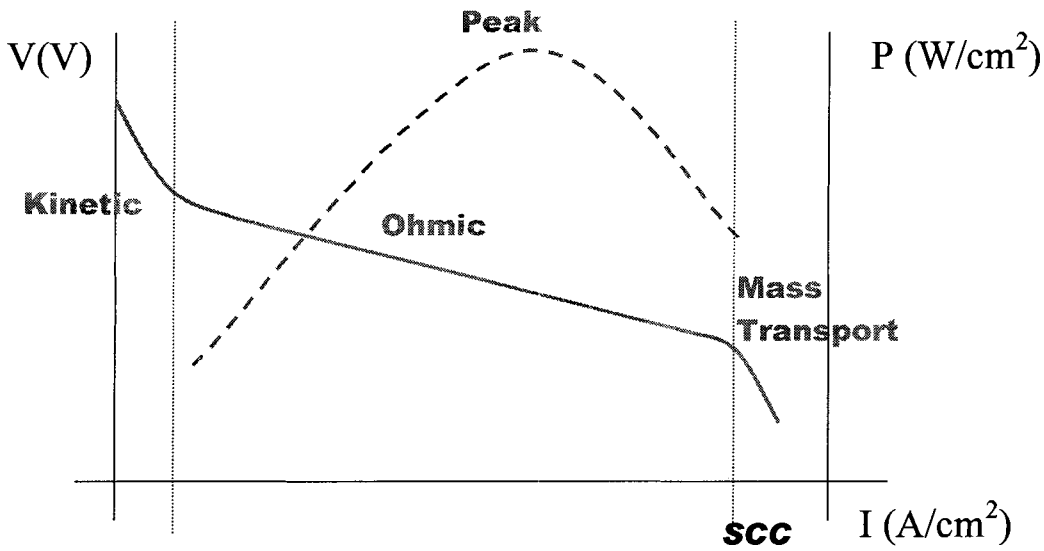

Figure 3: Denoted polarization curve

In Figure 3, the left vertical axis represents potential and the right vertical axis is power or power density. The horizontal axis is current or current density. The polarization curve is shown with a thick solid line and the power curve is shown with a thick dashed line. The operating regimes of kinetic, Ohmic and mass transport are segmented with thin dashed lines. The open circuit voltage (OCV) is the potential produced by the fuel cell when presented with a high impedance load. Peak power occurs when the voltage loss due to incremental current changes is greater than the power gained by consuming more fuel. The short circuit current is the maximum current that a fuel cell can produce, which is often linked to the onset of flooding. Partial flooding can result in an exponential decline in the potential. Once the catalyst layer becomes completely flooded, both current and voltage drop to zero. For larger fuel cells with high flow rates at the cathode, flooding can be prevented entirely, and the short circuit current occurs when the mass transport limited decline reaches zero. Theoretical polarization curves produced with simulations are presented in chapter 2. Actual polarization curves from micro fuel cell prototypes are presented and discussed in chapter 4.

1.1.1.1 PEM Fuel Cell Chemistry

For a hydrogen fuel cell the half reactions are

$$H_2 \rightarrow 2H^+ + 2e^- \quad (1)$$

$$4H^+ + O_2 + 4e^- \rightarrow 2H_2O \quad (2)$$

The maximum electrical potential generated by the electrochemical reaction can be determined from the Gibbs free energy. The half-cell potential of hydrogen oxidation is defined by international convention to be zero. The half-cell potential for the formation of water at the cathode is 1.23 V. The Gibbs free energy calculation gives an ideal maximum potential for a hydrogen fuel cell; however, actual fuel cells' kinetic, Ohmic, and mass transport losses reduce the actual potential of the fuel cell [1].

Some PEM fuel cells operate by directly oxidizing methanol at the anode to produce hydrogen ions, and carbon dioxide [1]. Methanol has the advantage of easier storage at room temperature, but suffers from slower reaction kinetics, more complicated waste management, and methanol crossover, as most polymer membranes are not impermeable to aqueous methanol. The electrochemical mechanism for the catalytic reduction of methanol to protons and carbon dioxide is not precisely understood, however, the net anode chemical reaction is

$$CH_3OH + H_2O \rightarrow 6H^+ + CO_2 + 6e^- \quad (3)$$

The cathode reaction is identical to the standard PEM fuel cell case. Although six electrons are created for every molecule of methanol consumed, the sluggish kinetics of the methanol reduction reaction result in activation losses for methanol fuel cells to be larger than in hydrogen PEM fuel cells.

1.1.2 Direct Methanol Fuel Cells

The direct methanol fuel cell (DMFC) uses methanol at the anode, as described in the previous section. Methanol as a fuel is applicable to a range of fuel cells from portable micro fuel cells, to automotive, to remote stationary applications [1].

Methanol, a liquid at room temperature, yields much higher volumetric energy density than hydrogen. Furthermore, methanol is easier to handle and contained than hydrogen and is readily available both from the partial oxidation of methane or through a brewing process from biomass. However, methanol has a serious disadvantage, because the methanol reduction reaction is much more sluggish than hydrogen reduction, seriously impacting the utility of the DMFC. First, significantly higher catalyst loading (mg of catalyst per geometric area of electrode) is required to achieve useful power densities. Typical noble metal catalytic loading for a hydrogen fuel cell is 0.5 mg/cm^2, whereas catalyst loading for a direct methanol fuel cells are closer to 4 mg/cm^2. The incremental cost of the additional catalyst makes the use of DMFCs for larger fuel cells economically prohibitive. The higher activation losses lead to less efficient practical fuel cells than hydrogen fuel cells. Most common solid polymer electrolytes are permeable to methanol as well as protons. Although protons are typically transported through the membrane faster than methanol, the electrochemical oxidation of methanol at the cathode further reduces the potential of the fuel cell. Methanol crossover has a double impact on fuel cell efficiency: first, on the efficiency of the cell by reducing the potential; and second, through methanol losses to direct oxidation without generating current. Finally, DMFCs produce carbon dioxide as part of the anode reaction. Unlike a hydrogen fuel cell, a DMFC has two-phase flow at both the anode and cathode. While carbon dioxide has

little environmental impact if the methanol is sourced from biomass, it complicates reactant management, as carbon dioxide must be removed from the anode fuel stream.

DMFCs have significant disadvantages that would seem to limit them to scientific curiosities. However, for small portable fuel cells, the impact of the higher cost of the catalyst is significantly less than the impact on larger fuel cell systems. The following table shows the estimated materials cost of a DMFC systems for a given output power. Two typical catalyst configurations are considered: 20% platinum on carbon for the cathode, and 40% platinum-ruthenium on carbon for the anode. Catalyst prices were obtained from E-Tek Inc. Nafion prices were obtained from Alfa Aeser.

Table 1:Material cost per kilowatt

Material	cost/cm2	1 mW	10 mW	100 mW	1W	1kW	100kW
Pt 20%	$0.04	$0.00	$0.02	$0.21	$1.91	$381.25	$38,125.00
PtRu 40%	$0.34	$0.02	$0.17	$1.86	$16.94	$3,387.50	$338,750.00
Nafion	$0.12	$0.01	$0.06	$0.65	$5.88	$1,175.43	$117,543.34
Total		$0.02	$0.25	$2.72	$24.72	$4,944.18	$494,418.34

While the relative cost impact remains constant, as expected, the total dollar difference is significantly less for small fuel cell systems. For a system operating below 100 mW, the manufacturing cost will typically be significantly larger than the materials costs, further reducing the impact of catalyst costs.

Methanol crossover may be mitigated in two ways: by using newly developed membranes, which have much lower methanol crossover rates; or by reducing the concentration of methanol at the cathode, which reduces the concentration difference across the membrane and therefore the rate of diffusion. Given that the shortcomings of the DMFC can be overcome, and significant improvements possible in volumetric energy density, DMFCs may be a viable option for micro power applications.

1.2 Micro Fuel Cell Overview

Micro fuel cell systems are small fuel cells targeted for conventional battery replacement. These fuel cells generally produce between 0.5 and 50 W of power. The term micro fuel cell can also be used to describe a fuel cell that is fabricated using micro electromechanical systems (MEMS) technology. In this thesis the term micro fuel cell refers to a fuel cell smaller than 10 cm^3, the practical volume limit for plate and frame fuel cell construction illustrated in Figure 1.

The driving force behind micro fuel cell research is the requirement for higher energy density portable power. Unlike transportation where mass energy density is important or stationary power where efficiency and lifetime are crucial, volume is the single most important parameter for micro fuel cells. There are several opportunities for reducing fuel cell system volume. Volume reductions over normal PEM systems can be achieved in the fuel density, balance of plant (BOP) and the fuel cell itself.

The first, and most obvious volume reduction, is to use a liquid fuel, such as methanol, in place of hydrogen. While hydrogen is very light, it is also one of the least dense, the hardest to liquefy, and most difficult to contain compounds. Further improvements in fuel energy density can be obtained by recirculating water produced at the cathode back to the anode, removing the requirement for water to be stored in the fuel tank to satisfy the reaction [1].

The balance of plant consists of all the remaining components of the fuel cell system that are not the fuel cell or the fuel, including: flow control devices, such as valves, fans and pumps; electronic conditioning components such as inverters or battery charging circuitry; and packaging and insulation. The energy density of the BOP is maximized by eliminating all BOP components. This approach is not practical and conflicts with the previous requirement

to store only pure methanol as a fuel. Practically, balance of plant energy density is maximized by reducing the number of components, and minimizing the size of those components through MEMS techniques, or other related miniaturization approaches.

The final component available for optimization is the fuel cell itself. Unlike some MEMS devices such as sensors, a micro fuel cell cannot benefit directly from reduction in patterning line-width. The surface area of the fuel cell is determined by the output power required, the activity of the catalyst, and the efficiency of the fuel cell. The ability to pattern smaller features cannot alter this relationship. However, MEMS techniques and microfluidic theory can be used to minimize the thickness of the fuel cell, and hence the overall fuel cell volume.

Because the surface area of the fuel cell can only be reduced by improvements in catalytic chemistry and electrode design, therefore any volumetric gains must be made by reducing the thickness of the fuel cell system. Table 2 illustrates some typical thicknesses for common fuel cell components.

Table 2:Common Fuel Cell Thicknesses

Component	Unit Thickness (μm)	Total Thickness (μm)
Membrane	200	200
Catalyst Layer	20	40
Gas Diffusion Layer	200	400
Flow Fields	3000	6000
Gaskets	750	1500
End Plates	5000	10000

The most significant and practical reduction in volume may be achieved by reducing or eliminating the endplates, gaskets, flow fields and GDLs. The reduction of thickness has been the primary goal of micro fuel cell research even if some authors do not specifically state it [2-

32]. Most of the reduction can be realized by redesigning the flow fields, gaskets, and end plates. Reducing the flow field volume is straightforward, from a fabrication point of view. Limitations on the size of the flow field are given in chapter 2. Gaskets can be replaced with adhesive seals. End plates, however, present a substantially different problem.

Endplates are the most desirable component to eliminate because they perform the purely mechanical function of holding the fuel cell together, while consuming significant volume. However, this function has a greater impact than merely assuring that the fuel cell is sealed. Compression reduces the contact resistance between the various layers, making bipolar current collection possible, and reducing the impedance of the catalyst layer by lowering the particle-to-particle contact resistance. While it is relatively straightforward to replace the mechanical seals with adhesive seals in a small fuel cell, current collection becomes substantially more difficult to implement.

Researchers have investigated the microfabrication of all of the components of micro fuel cells, beginning with flow fields, and working toward all layers of a fuel cell system [2-32]. However, a practical micro fuel cell requires investigation of methods for fabricating the electrodes for compressionless operation in an ambient environment.

1.2.1 Micro Fuel Cell Literature Review

The first potential micro fuel cell reported in the literature was not intended for micro power applications; it was realized as a laboratory experiment to give a segmented MEA architecture for measuring the current performance of the cell [2]. The authors used photolithographic patterning of printed circuit board material to make segmented flow fields with thin film gold current collectors and standard MEA materials and assembly techniques

for the rest of the cell. They monitored the current collected on 18 isolated segments within the cell to determine how current was distributed under varying gas flow conditions.

The birthplace of the direct methanol micro fuel cell is generally regarded to be the Los Alamos National Laboratory. In a 2000 paper, they outlined the current state of the art of DMFC research at Los Alamos [3]. Under optimal conditions they achieved an open circuit voltage of approximately 0.65 V and a short circuit current density of approximately 0.7 A/cm^2. However, these results were obtained with catalysts loadings of nearly 10 mg/cm^2 that is not commercially viable.

McLean *et al.* analyzed fuel cell systems and micro machining techniques and investigated for areas of synergy and potential applications [4]. They concluded that micromachining techniques could lead to "increased power density, heat and mass transfer and catalyst utilization; enhanced efficiency; reduced system complexity and opportunities for new fuel cell applications." However, their analysis only included traditional micro machining techniques and focused primarily on plate and frame fuel cell topologies and assembly processes.

Kelly, Deluga and Smyrl reported a truly micro fabricated fuel cell in 2000 [5]. By creating a micromachined selectively porous silicon substrate, they formed simple, 5 mm cells. They hot pressed the gold-coated silicon substrate into a previously catalyzed Nafion membrane, creating a cell. They reported a short circuit current density of 0.55 A/cm^2 and an open circuit voltage of 0.6 V with 0.5 M methanol at 0.2 L/min and air forced at 0.2 L/min.

Hockaday *et al.* described a fuel cell system, which reduced the cost of previous fuel cells systems by using vapor deposition techniques directly on the MEA [6]. They also segmented their MEA by selectively depositing proton-conducting membranes within a porous substrate,

increasing the performance. Until recently, Hockaday's cell was considered the most mass-production and cost friendly micro fuel cell design.

Sim *et al.* proposed that a very small micro machined fuel cell could be used to power medical micro-sensors [7]. They used two gold-plated silicon plates etched as flow fields and pressed into a Nafion membrane similar to the Kelly cell, but with channels instead of pores. Their gold acted as both a current collector and catalyst. They reported very poor performance, likely because they did not use an appropriate catalyst, and because their stochiometric (1:1) methanol-water solution would have lead to massive methanol crossover. They concluded that a DMFC would likely not be an ideal embedded power source because of safety concerns over methanol, which is quite toxic.

Lee *et al.* proposed a new "flip-flop" micro fuel cell design where both anode and cathode are present on a single face [8]. While the flip-flop design does provide ease of manufacturing for solid-state systems, allowing in-plane electrical connectivity, it complicates the gas manifolding substantially. Instead of electrons being routed from front to back, gasses must be routed in crossing patterns. Individual cells achieved peak power densities of approximately 20 mW/cm^2. However, the cells were successfully connected in series to create a stack, with a short circuit current density of 200 mA/cm^2 and an open circuit voltage of approximately 3 V.

Meyers and Maynard gave an overview of different micro fuel cell design trade-offs [9]. In particular, they analyzed the theoretical limitations of in-plane fuel cells, where the anode and cathode are side-by-side, with an ionic bridge between them, similar to a field effect transistor configuration. While this form of fuel cell is very easy to manufacture using solid-state technology, they showed that its performance was inherently limited, and had much

poorer performance than a through plane connected cell. They found that the monolithic, side-by-side design was limited to less than 5 W/cm^3, compared to the more traditional top and bottom design, which was limited to about 12 W/cm^3.

Min *et al.* recently published a variant of the design first published by Lee *et al.* where they maintained the same general "flip-flop" configuration, but used a spin-on form of Nafion to create the ionic conduction path [10]. They reported poor results, with current in the microamps range, and voltages below 0.4V. While their fabrication technique was a slight advance on the original design first published by Lee, it provided insufficient performance and reliability.

Heinzel *et al.* report a small fuel cell, carefully constructed out of traditional fuel cell materials such as carbon paper and graphite, can that achieve a peak power density of 55 W with a four-cell stack, 20 ml/min hydrogen, and 50 ml/min air [11]. They achieve currents of approximately 80 mA/cm^2 before the performance begins to degrade, but do not report the short circuit current. While their power output was impressive, the cell was quite large, over 0.5 L in volume and weighing over 1 kilogram. This cell could be taken as approaching the limits of traditional manufacturing techniques for fuel cells.

Recently, Kelly *et al.* have published an updated article on their micro-pore based fuel cell topology [12]. Using their system, they tested several new catalysts, and found, predictably, that high platinum loading lead to better performance. They also demonstrated that micro fuel cells competed very well with their larger fuel cells reported in the literature with respect to current density.

Ishida *et al.* used a fiber optic inspired technique and created a micro fuel cell based on a Flemion tube [13]. The cathode was inside the tube and the anode was on the external face.

Although a very novel design, they achieved poor power densities of less than 1 mW/cm^2 with methanol and air.

D'Arrigo *et al.* deposited porous silicon using chemical vapor deposition (CVD) on top of a previously etched wafer, and spun-on Nafion in the resulting matrix to create a cell that required no assembly steps [14]. While they were successful in creating a cell-like structure, no performance data was given. Even though they do not require assembly, their fabrication process is long and complex requiring several sensitive CVD processes to fabricate properly supported porous silicon.

Although this overview has primarily concentrated on PEM based micro fuel cells, work on SOFC based micro fuel cells has progressed as well. Micro SOFCs are simpler to fabricate because of their all-solid-state construction. However, the prohibitively high operating temperatures (> 500 C) required for sufficient oxygen diffusion through the exchange membrane limit the use of micro SOFCs for portable applications. Jankowski *et al.* reported a micro–SOFC. They found that the peak output power of the micro SOFC was an order of magnitude lower than the PEM, even at elevated temperatures. Tomsett *et al.* designed a compact tubular SOFC using traditional machining techniques for the purpose of evaluating different catalyst systems for direct methane reforming, however they did not attempt to design the system for portable use [16].

Yu *et al.* described a plate and frame cell with a slight modification to the current collectors [17]. By sandwiching copper between layers of gold, they were able to decrease the internal resistance of the thin film current collectors, which corresponded to an increase performance of the fuel cell, achieving 193 mW/cm^2 with H_2 and O_2.

Shah *et al.* described a fuel cell similar in concept to our design but very different in implementation. In their implementation, sets of fuel cells are constructed on a bulk Nafion substrate by sequential depositions through a set of polydimethylsiloxane (PDMS) stencils [18]. The flow channels for the cell were subsequently produced by casting PDMS over a micromachined mold, and adhering the flow channels to the substrate. While their techniques were similar to ours, they only achieved 0.3 mW/cm^2, primarily due to the structure of their electrodes.

Seo and Cho [19] proposed an alternative fabrication method for the flip-flop architecture of Lee [8]. Their proposal attempts to use MEMS techniques to fabricate the catalyst by used an array of micro-rods coated with platinum as the catalyst. While their research is an excellent example of the potential of micro machining, micro-rods make poor catalysts because their surface area is low compared to the nanoparticulate platinum normally used in fuel cell electrodes. They were only able to achieve sub-milliwatt power with the electrodes they had fabricated.

The Stanford research team has developed a number of PCB based fuel cells [20] similar to those developed at Fraunhofer [11] or the original cells built at Los Alamos [2]. They have done a significant amount of engineering on the flow and current collection and have achieved power densities similar to those reported by Fraunhofer. They used gold plated copper as their electrodes, which presented the best short-term solution, but is prone to corrosion over the long term. Testing with hydrogen and oxygen they achieved results consistent with large-scale fuel cell systems, with power densities between 500 and 700 mW/cm^2. When using air instead of oxygen, they achieved power densities of approximately 200 mW/cm^2. The long-

term chemical compatibility of the gold-copper electrodes and the polymers used in the substrate is the primary concern for this design approach.

Using a different approach, the team from the University if Illinois at Urbana-Champaign designed a formic acid fuel cell [21]. Formic acid cells are similar to direct methanol cells, with formic acid having lower energy density, but better reaction kinetics than methanol. They built a fuel cell design similar to Kelley's, using deep reactive ion etch (DRIE) etching to form the diffusion pathways in the silicon substrate, and an electroplating technique to deposit the catalyst. They report power densities of approximately 17 mW/cm^2, which is respectable for a passive air-breathing fuel cell.

Some of the best verifiable results for micro DMFC operation have come from the University of California at Los Angeles, where they achieved 40 mW/cm^2 using methanol and forced air [22]. They employed DRIE to form bipolar plates in silicon, and then deposited a Ti/Cu/Au electrode with 3 μm of copper forming the bulk current collector. This system is similar in architecture to the Stanford system but uses silicon instead of polymers as the substrate for the fuel cell. While a substrate such as oxidized silicon is stable, the electrodes themselves are subject to corrosion over longer operating times.

Kubo, from NEC Research recently described their efforts to create a direct methanol micro fuel cell around a carbon nano-horn (a truncated nanotube) as a catalyst support instead of the high surface area carbon usually used in fuel cells [23]. They suggest that increased performance due to increased surface area can lead to better power density and, therefore, smaller fuel cells. Peak power data of 1W and 12W for each fuel cell were shown, but the fabrication method, architecture, and size of the fuel cell were not disclosed.

Qiao *et al.* investigated a platinum plating process for the fabrication of a micro tubular DMFC [25]. Flemion tubes were used as the substrate. The platinum black electrodes were deposited using a modified electrochemical plating process. A peak power density of 2 mW/cm^2 was recorded. The cyclic voltametry (CV) analysis indicates that the platinum black is chemically active but the polarization curve indicates high activation and Ohmic losses.

Young and Young from KASIT described the fabrication of a micro pillar support for PEM cathodes [26]. The columns are fabricated using DRIE in silicon to fabricate electrodes. Platinum is sputtered on the columns to form the electrodes and the entire assembly is pressed into a bulk Nafion substrate. They compare the performance of their new electrode to the performance of a planar electrode. The planar electrode produced 5 $\mu W/cm^2$ and the microcolumn electrode produced 122 $\mu W/cm^2$ peak power. It is difficult to exceed the total active surface area of a porous electrode, as porous electrodes have been extensively researched in both fuel cell and chemical engineering. Poor performance of non-porous electrodes in the literature has led us to conclude that the practical fuel cells should employ standard porous electrodes.

The high aspect ratio UV-curable epoxy SU-8 was used by Hsieh *et al.* to create flow fields on a copper plate [27]. A copper sheet is coated with SU-8, which was patterned into flow fields. Silver was deposited on and around the flow field risers to provide current collection from the top of the flow field rib to the copper substrate. Thin film of Pt on Nafion was used as an electrode. The Pt-Nafion-electrode assembly was physically attached to the flow fields using plastic endplates. They report power densities of between 20 and 30 mW/cm^2 using hydrogen as a fuel and forced and passive air at the cathode respectively. Although using bulk metals such as silver and copper can reduce the Ohmic losses due to edge collection, neither is

electrochemically stable at the cathode and copper is a known poison for water-based solid ionic conductors.

Cohen *et al.* have taken a radically different approach to fuel cell design [28]. Rather than using a solid electrolyte, the fuel cell takes advantage of the properties of laminar flow in microchannels. By using narrow channels with laminar flow, fuel, and deionized (DI) and oxygenated water can be produced as three laminar streams. By depositing the electrodes on the sidewalls of the channel, a fuel cell is formed with the DI water serving as the insulating electrolyte. As long as the fuel stream exists, the system prior to the diffusive mixing of the fuel and electrolyte streams, the system functions as a fuel cell. However, to maintain laminar flow, constant fluid motion is required, increasing the pumping loads, and decreasing efficiency. The oxygen content of water is too low to sustain high current densities, limiting the overall volumetric power density of the cell. While the approach is theoretically interesting, it is not practical for a practical system.

Employing a system similar to [17], Chan *et al.* use flow fields micro machined in a spiral pattern using micro laser ablation of poly(methyl methacrylate) PMMA [29]. After ablation, gold is sputtered on the PMMA to provide a bulk current collector. Silver paint is deposited through a stencil on the surface of a carbon paper electrode in a grid pattern to improve the conductivity of the electrodes for edge collection. Peak power densities of 80 and 300 mW/cm^2 were reported for hydrogen and air, and hydrogen and oxygen, respectively. These are respectable values for micro fuel cells, but average for bipolar compressed cells.

Using a cathode supported approach borrowed from the design of solid-oxide fuel cells, Frey *et al.* built a fuel cell with sequential layer deposition [30]. The cathode catalyst was spray deposited directly on the substrate, and Nafion was used as an electrolyte. However,

instead of hot pressing the cathode into a bulk Nafion, a Nafion ionomer was spray deposited on the cathode. A solvent substation and dilution to DI water was required to avoid explosion risks. A series of vacuum drying steps was required after each coat to create a defect free membrane. The anode catalyst and current collector was deposited on the spray deposited membrane. They achieved a respectable power density of approximately 20 mW/cm^2 with 0.5 M methanol and a passive cathode. At the end of their paper they discussed the possibility of a serial strip cell system, which presages our design. They discussed possible current collectors and conclude, that gold is the most appropriate current collector.

1.2.1.1 Themes in Micro Fuel Cell Design

A limited number of viable design options exist for micro fuel cells, and most have been explored over the last five years by a number of researchers. In fact, a taxonomy of micro fuel cell design is missing in the literature, and the vocabulary used to describe architectures is confusing. In this section, we present a set of micro fuel cell architectural classifications, and then describe each of them within the context of this taxonomy. Generally, micro fuel cells can be divided into four architectural and four fabrication classes, as shown in Figure 4.

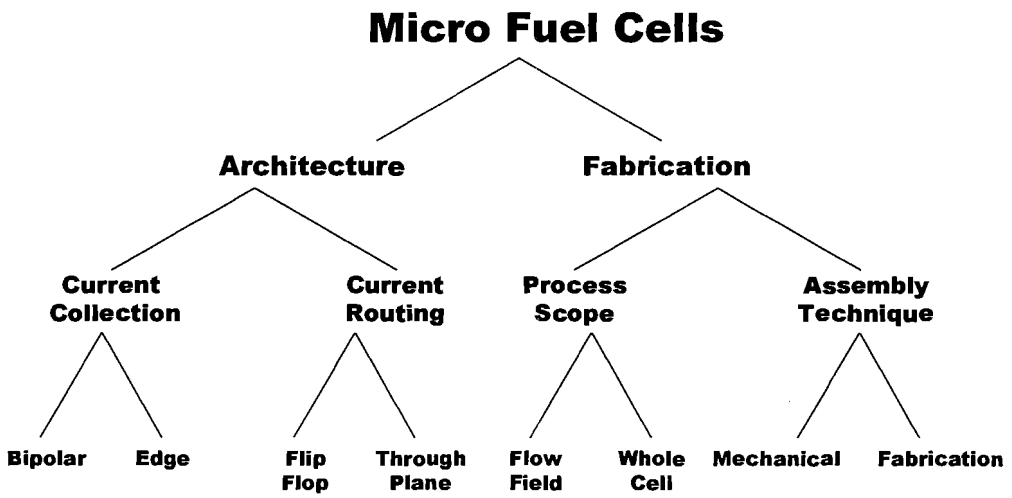

Figure 4:Micro fuel cell taxonomy

The tradeoffs between the current collection architecture and the fabrication process yield the final design of the fuel cell, and ultimately its theoretical performance limits. The architecture determines the potential performance, while the fabrication technique determines how well the architecture is realized.

1.2.1.2 Architecture

The architecture of micro fuel cells primarily addresses the transport of fuel, oxidant, electrons, and protons through the solid and liquid phases of the fuel cell. This classification should not be confused with the micro architecture of the electrode itself, as discussed in chapters 2 and 3, or the system level architecture which is primarily concerned with the control of fuel, oxidant and reaction products entering and leaving the fuel cell. Fuel cell architecture is primarily concerned with the routing of fuel, oxidant, electrons and protons within the cell, as well as from cell to cell in a potential stack. Plate and frame bipolar current collection is the standard design for large fuel cells; however, the scale of micro fuel cells makes other architectures feasible and potentially valuable.

1.2.1.2.1 Current Collection

One of the most important considerations in micro fuel cell design is the method of current collection. In most large-scale systems, the current is collected primarily in a bipolar manner through the stack. In bipolar collection, the current is primarily perpendicular to the cell, minimizing the path length for the current. Current through the stack is constant, and voltage accumulates cell to cell. At each end of the stack, current must be collected from a single point, and current flows parallel to the plate. Most large fuel cell stacks use highly conductive endplates, such as gold plated copper for this purpose. In edge collection, fuel cell electrodes are arranged in an array on the surface of the electrolyte. Current travels primarily parallel to

the electrode. Where series connections are required, current travels perpendicular to the membrane. Cylindrical or tubular fuel cells are an example of large-scale edge collected systems. Figure 5 illustrates the perpendicular and parallel current routing in edge and bipolar current collection.

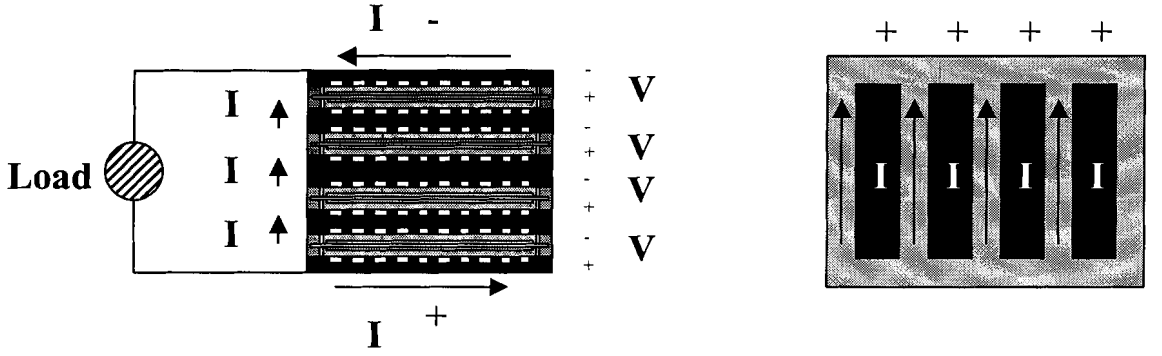

Figure 5: Bipolar (left) and edge (right) collection in fuel cells

For most large fuel cells, bipolar collection is the only viable choice. At significantly higher current densities, the additional Ohmic losses due to the longer path due to edge collection are intolerable. However, for micro fuel cells, running at lower current densities and with significantly shorter length scales, edge collection may indeed be viable. Most micro fuel cells use edge collection because edge collected designs are more compatible with MEMS processes. Bipolar collection requires that the bulk material of the bipolar plates be conductive. Only metal foils are an appropriate material for fabricating very small conductive flow fields. However, most common metal foils are not compatible with a fuel cell operating environment, because the combination of available potential and oxygen or hydrogen can lead to corrosion in most metals or alloys.

Because edge collected fuel cells are much easier to fabricate at small scales, they predominate in the literature. The poor performance of micro fuel cells reported in much of

the literature can be traced to poorly designed edge collected cell architectures. Particular attention must be paid to the conductance of the thin or thick film electrodes to ensure that losses from the edge collection system are not dominate. The behavior of edge collected fuel cell systems, and their impact on performance is described in detail in chapter 2.

1.2.1.2.2 Current Routing

Current collection, as described in the previous section, describes the predominant path of the current: parallel or perpendicular to the electrode. By current routing we refer to the method by which cells are wired in series to accumulate potential. In traditional bipolar stacks, potential is always accumulated perpendicular to the electrode, which is an inherent effect of the bipolar design, and relatively simple to achieve in edge collected systems. However, as first proposed by Lee [8], an architecture inspired by micro electronics can connect fuel cells in series without the need for through plane connections. The flip-flop connection scheme has the advantage that all of the electrodes are on a single face, dramatically simplifying the fabrication of electrodes. Through-plane edge collected and flip-flop current collection techniques are shown in Figure 6.

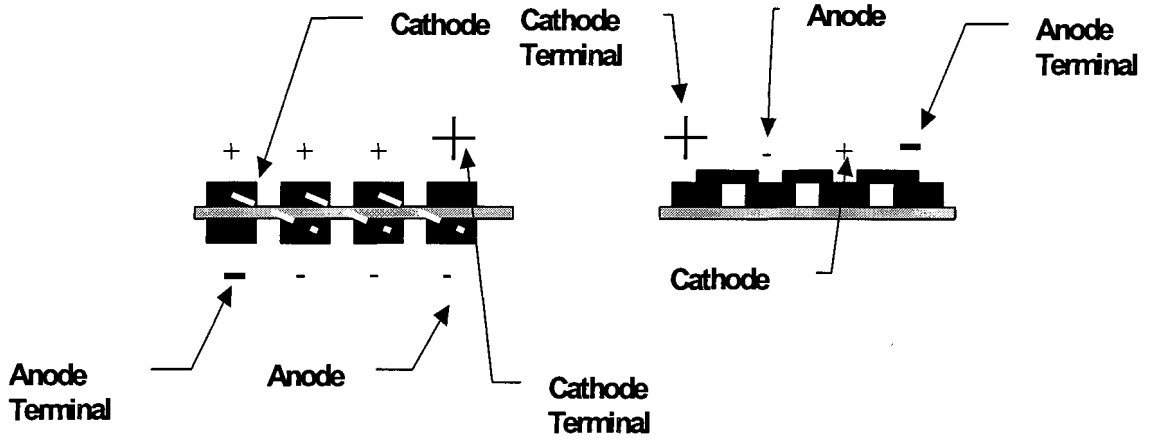

Figure 6:Through-plane (left) and flip-flop current collection (right)

In the above diagram, the gray substrate is the electrolyte, and the black boxes are electrodes, labeled "+" for the cathode and "—" for anode. The large "+" and "—" symbols indicate the terminals for the stack. In the through-plane system, current must follow the (white) dashed lines from the anode to the cathode either through the electrolyte or around its edge, to wire the cells in series. In the flip-flop system, current can follow the thin black rectangles in series from cell to cell. On the surface it appears that the flip-flop design is an obvious choice for micro fuel cells because of the simplicity of the current routing. However, the flip-flop design has two major flaws. First, protons must travel laterally through the electrolyte instead of vertically, potentially increasing the proton path length. Because the conductivity of the electrolyte is several orders of magnitude lower than the electrical conductivity of a thin film current collector, this is a poor trade-off. Second, the routing of fuel and oxidant is substantially more complicated in the flip-flop case, as both must be manifolded in complex three dimensional crossing patterns to ensure the fuel and oxidants can be supplied across the entire surface without mixing.

While the flip-flop design is an interesting academic architectural exercise, it is ultimately a dead end in practical fuel cell design. While the complexities of the fuel and oxidant routing can be solved with appropriate engineering, the losses due to the membrane impedance are not as easily overcome. The flip-flop architecture imposes a significant impedance penalty at high current densities by requiring the current pass laterally through a very small thickness. Even if the electrodes are made very thin to minimize the current passing through the electrolyte, the volumetric energy density of the flip-flop design is significantly less than the through plane case as described by [9].

1.2.1.3 Fabrication

Fabrication of micro fuel cells entails two primary constraints: first, to minimize the volume by reducing system thickness to an absolute minimum; and second, to create a fabrication process which is efficient and inexpensive. Fabrication approaches can be divided broadly into two categories, those which fabricate the flow fields and current collectors using MEMS or PCB inspired techniques and use commercial MEAs, and those which seek to fabricate the entire fuel cell. In both cases, the final assembly can occur at the end of the process or occur implicitly as part of the fuel cell fabrication process.

1.2.1.3.1 Fabrication Scope

Many researchers are content to concentrate on the flow field and current collectors. The focus of the research is less on the fabrication of the fuel cell, but on finding a sufficiently conductive thin film current collector. By using commercial membrane electrode assembly's researchers can focus on the fabrication of the current collectors. However, this approach has the serious disadvantage of requiring manual assembly. While for large micro fuel cells producing more than 20 W, manual or automated assembly is not prohibitive. For very small fuel cells, manual assembly becomes a serious cost and technical limitation. Any cell manufactured as separate flow fields and MEA will require compression to reduce the contact resistance between the MEA and the bipolar plate. For larger systems the volume fraction of the compression plates is sufficiently small to justify their use. For smaller cells, the size of the compression plates dominates, severely impairing the volumetric power density.

By examining the entire fuel cell, including MEA structure and fabrication, sealing, current collection, and flow fields, the volume can be significantly reduced, by removing all non-essential components. However, all of the fuel cell design problems must now be solved

again for the new MEA. Two approaches to full fuel cell fabrication have been examined: (1) all-MEMS techniques and (2) hybrid techniques. All-MEMS techniques attempt to form and pattern catalyst and gas diffusion layers using thick and thin film vacuum deposition processes, whereas hybrid techniques use existing or modified techniques to form the active layers and use MEMS techniques for the current collection and flow. The fabrication techniques described in this thesis are the most hybrid of all the approaches reviewed here. In our approach, we only micro fabricate the tool and die and use high-speed manufacturing processes for the actual fuel cell.

1.2.1.3.2 Assembly Technique

Closely related to the fabrication scope is the final assembly technique. In an ideal micro fabricated fuel cell, no assembly would be required, and the fuel cell would be fabricated layer by layer until the desired structure was reached. Practically, this is problematic because the materials of the fuel cell are not compatible with standard methods of fabricating closed channels. Most fuel cells require a small amount of assembly to form channels for the fuel and oxidant flow. Figure 7 shows the three most common techniques for micro fuel cell assembly.

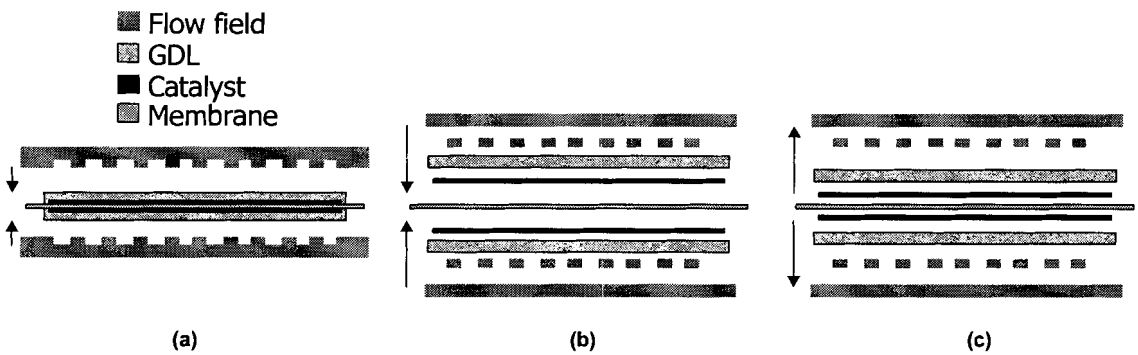

Figure 7:Common assembly techniques, arrows denote fabrication flow: Commercial MEA, fabricated plates (a), fabrication membrane outward (b), and fabrication flow fields inward (c)

Figure 7 (a) is the design described in the previous section, where only the flow fields and current collectors are micro fabricated and the fuel cell is assembled and held together with compression. While this is the simplest conceptually, mating the thin rigid flow fields with the flexible MEA is difficult in practice.

Figure 7 (b) shows a moderately popular approach for all-MEMS fabrication process and assembly. In this approach, the flow fields and GDL are fabricated using MEMS processes, a catalyst layer is applied to the top of the GDL, and the entire flow field/GDL system is pressed into the electrolyte, or the electrolyte is applied in a solvated form, and allowed to dry between the layers. This approach is intellectually appealing but has several disadvantages for practical systems. The processes used to create the on the channels GDL are usually very complex, expensive, and difficult to repeat. Depending on the electrolyte to hold the system together over a long period of time, especially if the electrolyte is exposed to a changing relative humidity, is unadvisable. The electrolyte will tend to delaminate from the catalyst layers if the entire system is not held under compression.

Figure 7 (c) shows the least common fabrication approach where, the membrane is used as a substrate, and the layers are built sequentially outward. This approach is problematic because fuel cell membrane materials are not rigid structures. Not only are they flexible, they deform up to 30% in volume with changes in relative humidity [94]. This approach places a great deal of stress on the subsequent layers. The assembly of the cell is either the final cap placed on the flow fields or the flow fields laminated onto the fabricated MEA. The design described in this document is the only practical membrane-out fabricated fuel cell. A description the fabrication process used to overcome the inherent shortcomings of the design is presented in chapter 3.

1.2.1.4 Placement of Micro Fuel Cells within the Taxonomy

Of the thirty-four contributions to fuel cell architecture and fabrication described in this document, most fit within the taxonomy. The categories in the table conform to the bottom level of the diagram shown in Figure 4. Publications are listed in the first column and their occupancy indicated with a check mark. For authors with multiple publications on a single architecture, only the first instance was included to avoid confusion.

Table 3: Taxonomy Occupancy for Fuel Cells in the Literature

Author	BP	Edge	Flip Flop	TP	Flow Field	Cell	Mech	Fab.
Cleghorn et al. [2]	✓						✓	
Ren et al. [3]	✓						✓	
McLean et al. [4]	✓			✓		✓		✓
Kelly et al. [5]		✓				✓		✓
Hockaday et al. [6]		✓		✓		✓	✓	
Sim et al. [7]		✓			✓		✓	
Lee et al. [8]		✓	✓		✓		✓	
Meyers et al. [9]		✓	✓		✓		✓	
Min et al. [10]		✓		✓	✓		✓	
Heinzel et al. [11]	✓				✓		✓	
Ishida et al. [12]		✓		✓		✓		✓
D'Arrigo et al. [13]				✓		✓		✓
Jankowski et al. [15]		✓		✓	✓		✓	
Tompsett et al. [16]		✓		✓		✓		✓
Yu et al. [17]		✓		✓	✓			
Shah et al. [18]		✓		✓		✓		✓
Seo et al. [19]		✓	✓			✓	✓	
O'Hayre et al. [20]		✓		✓	✓		✓	
Mozsgai et al. [21]		✓				✓		✓
Yen et al. [22]		✓			✓		✓	
Kubo [23]							✓	
Choban et al. [24]		✓				✓	✓	
Qiao et al. [25]		✓				✓		✓
Young and Young [26]	✓					✓		✓
Hsieh et al. [27]		✓			✓		✓	
Cohan et al. [28]		✓						✓
Chan et al. [29]		✓		✓	✓		✓	
Frey et al. [30]	✓			✓		✓	✓	

With the exception of Shah, Heinzel, Choban and Ishida these cells are based on silicon micromachining. In the case of Heinzel's architecture, micromachined metal foils are used, allowing bipolar collection in a micro stack. In Ishida's and Choban's case, microtubular architectures are used. In Shah's case, soft lithography and thin film techniques are used.

1.3 Motivation

Past research on the design and fabrication of micro fuel cells has been primarily concerned with scale without sufficient attention to the active components of the fuel cell itself. While most researchers have found a variety of methods to reduce the scale of fuel cells, few have managed to achieve the same energy density as current portable power technologies of 400 Wh/L. This disadvantage is primarily because the focus on micro fuel cells, and in particular MEMS techniques, have left performance and fuel cell behavior as a secondary consideration.

1.3.1 Application

Because fuel cell systems are very sensitive to operating conditions such as temperature, humidity, and load characteristics, designing a fuel cell for a particular application is critical. It is not possible to design a fuel cell that is suitable for all applications. Portable electronics is often discussed as the preferred initial application for micro fuel cells [1]. However, this application has more to do with market pull and financial considerations than the technical capabilities of micro fuel cell technology. Instead of considering portable electronics as the target application, we have designed our fuel cell with micro stationary power in mind. Micro stationary power includes data loggers, wireless telemetry, and remote monitoring technology. In this case, total power is low, punctuated by brief pulses of higher consumption as the RF transmitter sends data to the central logger.

Wireless telemetry has several advantages over portable electronics as a market. The system is stationary, leading to predictable operating conditions. In many applications these systems will be employed in interior spaces, so weather variations will have a limited impact on the performance of the system, in fact, these systems often monitor controlled environments such as storage facilities in hospitals where the operating environment is well understood and the impact of environmental variables can be easily mitigated. In addition to fixed or predictable operating conditions, stationary micro fuel cells can also be deployed in a fixed position and orientation, while portable micro fuel cells must be orientation independent and mechanically robust. This independence simplifies BOP considerations and the design of the surrounding packaging for oxidant flow.

Wireless telemetry systems have very predictable power consumption profiles. For the majority of the duty cycle the system is in a quiescent mode, drawing less than approximately 1 mW. During short bursts, the power will peak at 100-250mW as the wireless transmitter sends the data to the receiving station. This pulse-powered system is not compatible with fuel cell operation, but is ideally suited for hybrid systems. In a hybrid system, the fuel cell produces a constant power slightly higher than the quiescent, trickle charging a battery or supercapacitor. During the on cycle, current is dumped from the supercapacitor or battery into the transmit circuit. In this case, the fuel cell always runs at a constant power density, a preferred mode of operation, which is also advantageous for a micro fuel cell because it allows the fuel cell to be operated open loop, minimizing the balance of plant requirements for adjusting fuel flow to compensate for varying loads. For other applications, fuel cell size and cost would be dwarfed by the scale and price of active components, such as valves and pumps.

1.3.1.1 Design Targets

As outlined in the previous section, micro fuel cells generally can be divided into two categories of architecture and two categories of current collection. Assembly and fabrication can be performed after the fabrication of the flow fields and MEA, creating a compressed fuel cell, which increases the current output, but requires larger volume for the compression plates. In uncompressed cells, fabrication and assembly can occur simultaneously, simplifying the manufacturing process, and reducing the volume, but generally decreasing the performance of the fuel cell. Bipolar current collection uses the entire flow field volume to conduct electrons away, reducing the electrical impedance, but restricting the choice of current collector materials to those that are difficult to machine at the scale required for micro fuel cells. Metal foils can be used, as in [11], however, these foils tend to corrode in fuel cell operating environments. Based on the review of the existing literature, we have concluded that the following design targets are key concerns for fuel cell design in the previously described market:

1. *Uncompressed.* The volume required for a compressed fuel cell is not compatible with the target application of power for wireless telemetry devices. The lack of compression will increase losses due to electrical conduction through the catalyst layer, and will dramatically increase the resistance between the MEA and a flow field current collector. Particular attention must be paid to the electrode design to mitigate these losses.

2. *Edge Collected.* Edge collection can ameliorate the impact of uncompressed fuel cells removing the need to collect the current through the flow field. Current can instead be collected through the edge of the gas diffusion layer. However,

collection through the MEA requires that the conductivity of the MEA be much higher than a standard micro fuel cell.

3. *Volume.* The volume of the fuel cell must be minimized by minimizing thickness. Major volume reduction can be realized by eliminating compression, as already indicated. The remaining volume must be reduced by minimizing flow field and MEA volume. Flow field volume is fixed by mass transport requirements. MEA volume is dominated by the gas diffusion and membrane material properties.

4. *Fabrication.* Micro fuel cells can be fabricated with MEMS techniques; however, they do not produce fuel cells that are economically viable. For mass production, the fuel cell should use standard manufacturing techniques wherever possible.

Given the four design targets in the previous section, we now have a template for a novel fuel cell design to meet the requirements of wireless telemetry. Edge collection, compression and volume all entail performance design tradeoffs discussed in the next chapter. The specifics of the design are described in chapter 2, as theory and finite element analysis (FEA) is applied to the general design constraints to reach specific targets for the fabrications process. The fuel cell and material fabrications processes are outlined in chapter 3 and merge the theoretical design targets with constraint 4, which is fabrication specific.

1.4 Summary

While micro fuel cells have received a significant amount of research attention, the performance level, manufacturing cost, and reliability are still too low for successful micro fuel cell commercialization. Volume requirements for fuel cells below 100 cm^3 are very difficult to meet in practice. Compressed fuel cell designs using standard MEA topologies

benefit from reduced impedances in the catalyst layer and well-understood electrode dynamics. Novel uncompressed designs that can achieve smaller volumes and theoretically higher power densities have been plagued by poor performance because of poorly designed or poorly understood electrodes. The few researchers who have achieved a reasonable performance, such as Kelly *et al.*, use expensive and difficult manufacturing processes and have dubious reliability. For small, practical fuel cells, an uncompressed design with fully characterized electrodes and low cost manufacturing techniques is required.

Chapter 2 Theory and Simulation

2.1 Introduction

Fuel cells are complex systems, combining elements of mass transfer, electrochemistry, heat transfer, and electronics in a single physical system. These parameters are all interdependent, linked through the governing electrochemical equations. This strong coupling makes analysis of fuel cells a challenging task. General analytical solutions do not exist because the system of nonlinear equations is transcendental. Because it is impossible to uniquely determine the optimal design of a fuel cell, most fuel cell research has focused on empirical methods of fuel cell design. Most fuel cell simulation research has focused on creating better models of the fuel cell to accurately represent the internal state.

Fuel cell design is a classic over constrained engineering optimization problem. There are more variables that must be controlled and optimized than there are design variables, which can be altered to address them. For a given set of operating parameters, a best compromise must be chosen to ensure the fuel cell system meets the design requirements. These variables include non-performance criteria such as size, materials, and manufacturing cost.

Micro fuel cells are dominated by size requirements; volumetric energy and power density are crucial measures for micro fuel cell systems. Volume measures are affected by both the size of the system and the efficiency of its operation. System size is determined by fabrication technology and mass transport limitations. Fuel cell efficiency is determined by the microstructure of the electrodes and the electrochemical operating conditions, such as temperature, conductivity, and catalyst surface area.

In this chapter, micro fuel cell design is motivated through a combination of analytical, finite elements, and computational fluid dynamics (CFD) techniques. In maximizing volumetric power and energy density of the fuel cell, the volume can be reduced or the performance can be increased. Volume is dominated by fuel choice, flow field dimension, and cell architecture. Performance is determined by catalyst and electrode microstructure, and operating conditions. In practice, all the design parameters of a fuel cell are linked; however, volume and performance can be logically separated for most analysis. In this analysis, we consider the volume effects and performance effects separately.

As outlined in the previous chapter, we have suggested that a very thin uncompressed fuel cell to be the best solution for wireless sensor power. Because we have already eliminated compression plates and seals, the thickness of the fuel cell will be primarily determined by the size of the flow fields. First, we derived the limitations on flow field dimension from the effects of laminar and micro flow phenomena. Next, the impact of the design decisions on the electrochemical operation of the cell are examined from a cell efficiency and parasitic load point of view. Finally, the microstructure and operating conditions of the fuel cell are examined in the context of water management at the cathode. Micro structural properties of the electrode are derived using FEA analysis. A complete, quantified specification for the micro fuel cell is motivated from theory.

While these general theoretical investigations can be informative, one must be cautious when assigning meaning to the results. Based on our experience, the design of a typical fuel cell has over 25 coupled degrees of freedom, and the fabrication process has at least an additional 50 degrees of freedom. Obviously it is impossible to do an exhaustive study of the degree of coupling by crossing all the degrees of freedom to achieve an optimal design.

Instead, general analysis must be used to narrow the design space, and specific enquiries for specific designs can be undertaken. The following analysis focuses on general trends, in an attempt to generate basic engineering guidelines for the design of micro fuel cells. We do not claim that the guidelines are optimal, or even unique, only that by following these guidelines, the resulting micro fuel cell will have an acceptable level of performance as defined in chapter 1. The specific values derived for individual design parameters are only guidelines and only valid under the specific geometries and operating conditions considered.

2.2 Volumetric Constraints

The micro fuel cell is intended to replace conventional batteries in wireless sensor networks and other application where small volume is important. Therefore, the system must posses a performance and/or cost advantage over existing battery technology. Because fuel cells are less convenient than rechargeable batteries and because they must be refueled instead of simply recharged, the performance advantage must be significant.

Unlike batteries where the fuel is contained within the reaction chamber, fuel cells require a separate the fuel reserve from the reaction chamber. As such, the analysis of size and cost constraints on the fuel cell can be performed in two separate steps: first, the minimum size of fuel cell to generate sufficient power for the intended device; and second, the minimum volume required to meet the energy (lifetime) requirements of the device. Area (power) requirements are dictated by the application whereas volume requirements are dictated by the incumbent technology (batteries).

The volume requirements for a fuel cell are dictated by the current state of the art in battery technology. Energy density is usually expressed as power supplied over a unit of time per unit of volume (Wh/L). Dyer gives the operational energy density of a lithium-ion battery as 300

Wh/L [82], and the theoretical energy density of methanol as 4900 Wh/L. However, this comparison is irresponsible because completely recovering the theoretical energy density of methanol is impossible by the second law of thermodynamics. A more appropriate comparison would be between the operational energy density of a direct methanol fuel cell and a lithium ion battery.

2.2.1 Fuel Efficiency and Volume

The actual energy density efficiency of a direct methanol fuel cell can be found by integrating the power-supplied curve over time and calculating for the amount of methanol consumed. Conservation of mass demands that electrons, which are generated to do work, must be consumed at the cathode. By knowing the number of electrons required to meet the power demands of the device (amps sourced over time at a given voltage) the amount of methanol consumed is known, neglecting direct losses to leaks or methanol crossover. This method directly calculates the efficiency of the fuel cell by using the operational potential instead of the theoretical potential.

Power (P) in electrical devices is given by

$$P = VI, \tag{4}$$

where V represents voltage and I represents current. Many electronic devices operate at a constant voltage, or in a pulse-powered mode, which is piecewise constant, even in a quiescent or standby mode. Therefore, any change in the power drawn over time is given by changes in the amount of current. The number of cells wired in series required to meet this requirement is given by

$$N_{cells} = ceil\left(\frac{V_r I_{\max}}{P_{\max}}\right), \tag{5}$$

where *ceil* is the ceiling operator, V_r is the required voltage, I_{max} is the maximum current draw and P_{max} is the maximum power requirements. The total current drawn from all cells is

$$I_T(t) = \frac{P(t)}{V_r} N_{cells}, \tag{6}$$

where *P(t)* is the power drawn by the load and *I(t)* is the instantaneous current. The number of moles of fuel consumed is related to the number produced through Faraday's constant

$$n_{fuel} = \frac{Q}{kF}, \tag{7}$$

where Q is the total charge produced, F is Faraday's constant, and k is the stochiometric relationship between the consumed fuel and liberated electrons. For methanol and water at the anode $k = 6$.

The volume (v) of methanol required to source a given charge is easily derived from the molar mass of methanol (M_{MeOH}) and the density of methanol (ρ_{MeOH})

$$v_{MeOH} = \frac{n_{MeOH} M_{MeOH}}{\rho_{MeOH}}, \tag{8}$$

where n_{MeOH} is the number of moles of methanol consumed. The above relationship assumes that water is recycled at the cathode for use in the anode reaction. If a premixed water-methanol fuel is used, then the molar mass and density must be modified to reflect the mixture.

By definition

$$Q = It\,. \tag{9}$$

Combining these relationships it is possible to derive expressions relating the volume of fuel required to meet power supply lifetime requirements for a given fuel cell's V-I performance.

$$v_{MeOH} = \frac{N_{cells} M_{MeOH}}{V_r k F \rho_{MeOH}} \int P(t)dt\,, \tag{10}$$

where *P(t)* is the power consumption profile for the device. For constant power consumption

$$v_{MeOH} = \frac{N_{cells} M_{MeOH}}{V_r k F \rho_{MeOH}} Pt\,. \tag{11}$$

This relationship can be inverted to determine the length of time a given volume of fuel would last for a given duty cycle and fuel cell efficiency. If the application requires pulse-powered operation, the power consumption is given by

$$P(t) = \begin{cases} P_q & t \bmod T < \alpha T \\ P_o & t \bmod T > \alpha T \end{cases}, \tag{12}$$

where P_q is the quiescent power draw, P_o is the on cycle power consumption, T is the duty cycle period, and α is the fraction of the duty cycle in quiescent mode. The average power consumption is given by

$$P_{av} = (1-\alpha)P_o + \alpha P_q\,. \tag{13}$$

A schematic of this power consumption profile is shown in Figure 8.

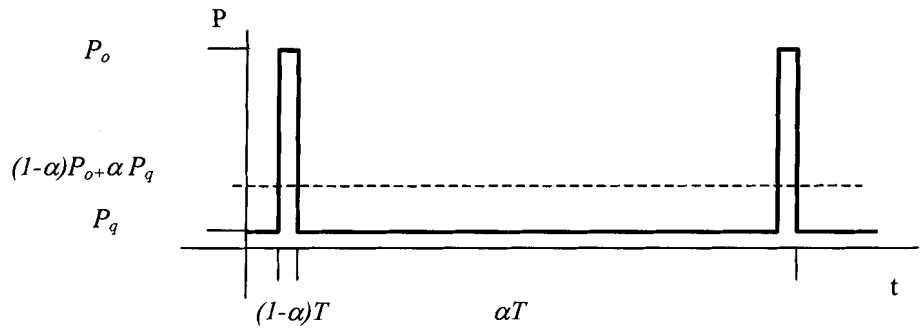

Figure 8: Pulse-power profile

Because fuel cells are not suited to rapid load cycling, due to mass transport limitations, fuel cells for portable electronics devices are usually linked with a small lithium-ion battery or supercapacitor to provide peak power. In this configuration, the fuel cell supplies P_{av} constantly, charging the battery or supercapacitor during the quiescent cycle. The volume of methanol for a fuel cell for a pulse-powered load is

$$V_{MeOH} = \frac{N_{cells} M_{MeOH}}{V_r k F \rho_{MeOH}} P_{av} t \,. \qquad (14)$$

In the above equation, the voltage, power and operating time are fixed by the application, the molar mass and density of methanol and k are physical constants, and the volume is dictated by the energy requirement. Hence fewer cells are required to supply the same potential if the performance of the fuel cell is improved.

Storage density is maximized when pure methanol is stored. However, methanol must be combined with water in a one-to-one molar ratio for the reduction reaction to proceed. Furthermore, commercially available polymer electrolyte membranes are permeable to methanol, resulting in high fuel crossover and low fuel cell efficiency. Generally, methanol is constrained to a 1 M (~5%) solution at the anode to reduce the effect of crossover. Using water recycling from the cathode, and BOP to manage methanol concentration pure methanol

can be stored and a 1 M solution can be presented to the anode electrolyte. These methods are outside the scope of this dissertation, which focuses exclusively on the fuel cell itself.

Beyond the direct impact of the fuel cell storage volume, the efficiency of the fuel cell has a significant impact on the volume of the fuel. When designing the cell, additional voltage losses will require more and larger cells. Therefore, the impact of Ohmic losses on the performance of the cell must be mitigated, not only to decrease the size of the cell, but also to decrease the size of the fuel reservoir required to supply the energy demands of the system.

2.2.2 Flow Requirements and Flow Field Volumes

Micro fluidic systems have been studied for over twenty years. The discipline of microfluidics has grown in conjunction with MEMS in an attempt to describe the behavior of fluid flow in small dimensions. Micro fuel cells are one of the latest additions to micro fluidic systems. However, micro fuel cells have not received the same scrutiny as other micro fluidic devices.

Micro fuel cells are unique in micro fluidic systems. While the channel diameters, methods of fabrication, and materials are often the same as other micro fluidic devices, the key fuel cell parameter, the required surface area of the catalyst, is a macroscopic quantity. For example, a fuel cell producing a modest 50mW/cm^2 requires 20 cm^2 electrode area to generate 1 W of power. The required area is determined by the reaction kinetics and is not reducible in the same manner as other MEMS devices. This macroscopic restriction implies that micro fuel cells will have long length scales compared to the dimension of the channel hydraulic diameter.

Considering a typical PEM planar fuel cell 5 cm wide and 10 cm long, slightly larger than a standard business card. Assuming peak power operation at 100 mA/cm^2 and 0.5 V then the fuel cell produces 2.5 W, with an equivalent current draw of 5 A. Furthermore, assume that the channel width and pitch is always 1 mm, but the channel height varies according to manufacturing practices. There are a total of 25 channels, each 10 cm long, for a total length of 2.5 m of fluidic travel. The total volume depends on the height of the channel, varying linearly between 0.25 ml and 2.5 ml for heights of 0.1 mm to 1 mm.

Because the fuel cell is running at an equivalent current of 5 A, it will draw approximately 43 μmol of electrons every second. Some simple arithmetic shows that a flow of 1 ml/min of 0.5 M methanol provides 50 μmol/s, assuming 100% fuel utilization. As a simple approximation, we will assume that 1 ml/min is sufficient to operate the fuel cell in steady state. In practice, the required rate is strongly dependant on the flow field geometry; however, for the purposes of this high-level analysis we will neglect geometric effects.

The effect of the catalyst area requirements on the overall system performance is profound. Micro fuel cells operate on length scales of hundreds of centimeters, while traditional micro fluidics have been practiced on length scales of centimeters. Although the hydraulic diameters may be equivalent, the much longer length scale of micro fuel cells imply that local micro fluidic effects such as surface tension, which have a profound impact on standard micro systems, will be secondary to cumulative effects such as pressure losses in micro fuel cell systems.

2.2.2.1 Cumulative Effects

Macroscopic internal pipe flows have been well understood for over 100 years [67]. The fundamental behavior of fluids in long pipes, including pressure losses due to frictional effects

is well documented. For micro fuel cell systems, all flows can be considered laminar as Reynolds numbers are generally less than 10. Even though the onset of turbulence occurs earlier in micro fluidic systems, the flow rates for turbulent flow in small channels exceed realistic flow rates for fuel cells.

The dominant fluidic forces in micro fuel cell systems are the normal continuum forces associated with normal fluid flows. However, because the required pressure scales as the square of the channel diameter, the behavior of these equations is somewhat different. The following sections outline the effect on standard laminar flow at small scales, and discuss, in the case of gasses, under what situations these flow conditions will depart from standard models.

2.2.2.1.1 Fluid Flow

Continuum models of liquid micro flows hold true physical dimensions above 100 nm [41]. Unlike gaseous flows in microchannels, liquid micro flows do not exhibit unusual characteristics because they exhibit non-Newtonian behavior, but because Newtonian flow yields potentially problematic solutions when the channel diameter is small. With viscosity values several orders of magnitude higher than gasses, the pressure drop effects in micro channels become acute [32]. According to standard laminar flow models, the pressure drop across a given length and hydraulic diameter is

$$\Delta P = \frac{uK\mu L}{D_h^2}, \qquad (15)$$

where ΔP is the pressure drop, u is the fluid velocity, K is a constant depending on the cross-section of the duct, μ is the dynamic viscosity of the fluid, L is the channel length, and D_h is the hydraulic diameter. In fuel cells, μ varies from 9 – 21 μPas for gasses and 350 – 540 μPas

for liquids [33]. Equation (15) determines the pumping pressure required for fluidic systems. For some micro fluidic applications, such as medical equipment, this pumping requirement is of limited concern because power is supplied from the grid. However for portable fuel cell systems, the pumping requirements represent a parasitic load, and must be minimized.

The following equation can be used as an initial estimate of the hydraulic diameter for rectangular channels.

$$D_h = \frac{2wh}{w+h}, \tag{16}$$

where w is the width and h is the height.

Figure 9 shows the greater back pressure required to drive water through channels of decreasing hydraulic diameter, with the dimensions described in section 2.2.2 and a flow rate of 10 ml/min. To maintain a constant volume flow rate the pressure drop scales as D_h^4 because of the additional surface flux term in the volume flow rate.

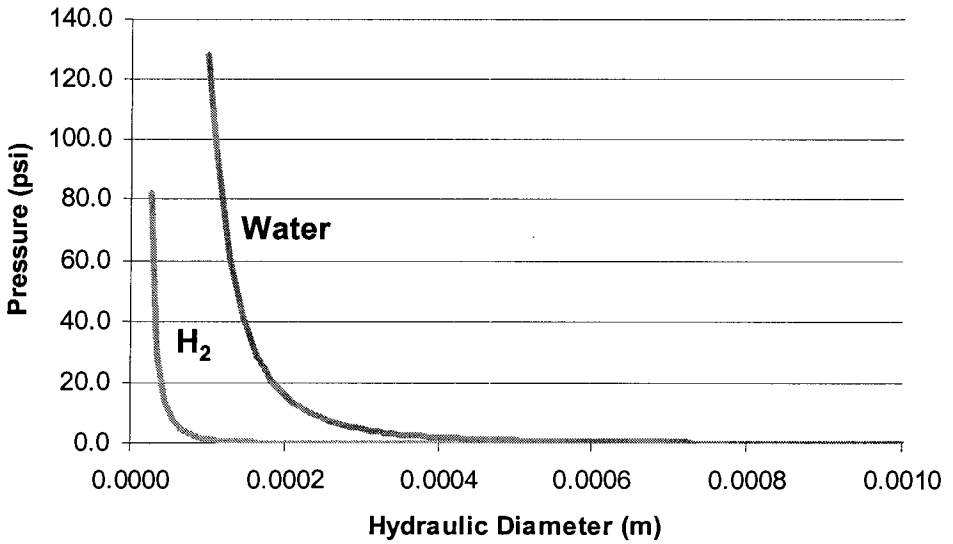

Figure 9:Pressure loss vs. hydraulic diameter for water and hydrogen

There is a pronounced elbow at 180 μm in hydraulic diameter, the water curve, where the pressure drops rapidly from over a 100 psi to 20 psi. For dimensions greater than 500 μm, the pressure drop is a modest 1 psi. For a channel with a more traditional micro fluidic length scale of 1 cm, the pressure drop at 100 μm would be only 4.5 psi, closer in magnitude to the local surface effects; however, for the length scale in the graph, the pressure drop is an order of magnitude larger. The gas pressure drop is significantly lower than the liquid pressure drop, reaching the rapid increase in pressure at 50 μm, and rapidly falling to less than 1 psi for larger diameters. Although the above graph is not entirely accurate for fuel cell operation, because the required flow rates would strongly depend on the operating conditions of the fuel cell it, however, does illustrate the impact of fluid viscosity on pressure drop. For larger micro fuel cells, with longer channels, the elbow will occur at larger hydraulic diameters. Figure 10 shows the pressure loss versus channel diameter for a fuel cell with a 10 m channel length.

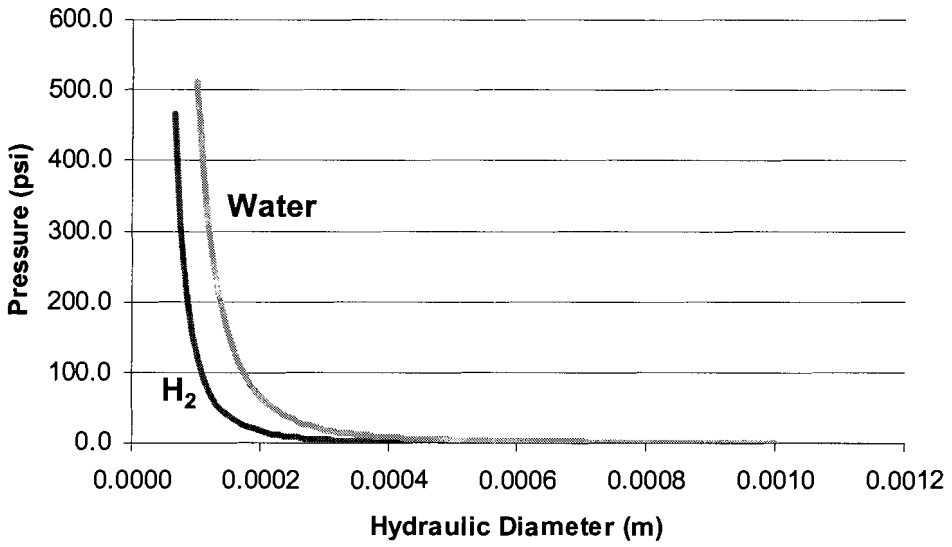

Figure 10:Pressure drop vs. hydraulic diameter channel length = 10 m

In the case of the longer fuel cell, the elbow occurs at 200 μm instead of 180 μm, and nearly 400 μm are required to reach pumping loads consistent with micro pumps, which typically cannot develop more than 4 psi of backpressure. This effect is as expected because the change in length will have a multiplicative rather than exponential effect on the curves.

While these calculations are straightforward, they illustrate that generating pressure driven liquid flows in micro channel fuel cells is not trivial. The pressures required to create even modest fuel flows through even moderately sized micro channels puts severe limitations on the balance of plant and fuel cell construction. It is conceivable for some current densities to build these cells as hybrid systems based primarily on diffusion transport, removing the pressure requirements.

2.2.2.1.2 Slip Flow

In laminar flow, the no-slip boundary condition assumes that the velocity approaches zero smoothly at the channel walls. Although this is a valid assumption for larger channels, there is a finite boundary region where the velocity profile is not parabolic. When the channel becomes small enough that the impact of this boundary layer is significant, the slip flow regimes must be considered.

Microfluidics is the study of fluid flows at channel diameters below 1 mm. It is distinguished from the research in chemical engineering pertaining to micro flows in fluidized beds and similar porous media because transport occurs in a single defined channel rather than in parallel across several micropores. While flow through a bed of random micro channels is modeled statistically, flow in a single smooth micro duct should be treated in the same manner as macroscopic duct flows, because smooth laminar flow develops.

The general behavior of a Newtonian fluid flowing in a duct is often derived from the Reynolds number, a dimensionless quantity which relates the viscous to the inertial forces in a fluid flow.

$$\mathrm{Re} = \frac{\rho u D}{\mu}, \tag{17}$$

Where D is the characteristic dimension of the duct and μ is the dynamic viscosity of the fluid. The Reynolds number reflects the relative influence of viscous and inertial forces. For large *Re* values, the momentum or external forces predominate. For small *Re*, viscous or internal forces predominate. For high velocity flows in large ducts, the flow is dominated by inertial forces and is usually turbulent. As D and u diminish, the viscous forces acting on a fluid will increase in relevance. At micro scales, viscous forces predominate, and flow behaviors change.

The assumptions leading to laminar flow become invalid as the characteristic dimension of the duct begins to approach the micron range. Exactly how the flow diverges from laminar flow, and at what point the divergence begins, has been a focus of study for over 15 years.

Harley *et al.* [34] and Pfahler *et al.* [35] were among the first to examine the behavior of a fluid in long micro channels. They observed a departure from the Poiseuille theory but were unable to definitively address the physical cause of the departure. Flockhart and Yang [36] performed numerical simulations and analysis and compared it to the data generated by Pfahler, and found it to be within error of classical predictions. Work continued in this area, but given the sensitivity of the measurements, it was difficult to satisfactorily determine the actual behavior. Arkilic, Schmidt and Breuer [37] devised a more accurate experiment, and a first order approximation of slip flow at a boundary. They determined that for different

regimes of the ratio of *D/L* or characteristic length of channel length, the fluid could enter slip or even molecular flow. Their approximation (presented below) allowed the changeover point to slip flow to be estimated. This pioneering work was updated in [38]. Papautsky *et al.* [39] attempted to derive the behavior from first principles by examining deformable fluid elements. Finally, Gad-el-Hak [40][41] created a complete framework for microfluidic theory based on the Knudsen number of the flow. This seminal paper is the basis for most modern micro fluidic research. Mala and Li [42] used extremely sensitive experimental techniques, which verified Gad-el-Hak's theoretical framework. With a solid foundation, micro fluidics began to receive attention from the chemical engineering community who had first pioneered research on microfluidics for use in porous beds almost 50 years earlier [43].

Arkilic and Gad-el-Hak have proposed similar schemes for the classification of micro flow regimes based on the Knudsen number. Gad-el-Hak's system is reported because it is more thoroughly developed than Arkilic's system.

The Knudsen number is the ratio of the mean free path of a gas (λ) to the characteristic length of the channel [44],

$$Kn = \frac{\lambda}{D}. \qquad (18)$$

The Knudsen number can also be defined as proportional to the ratio of the Reynolds number and the Mach number (from [40]) by

$$Kn = \sqrt{\frac{\pi\gamma}{2}}\frac{\mathrm{Ma}}{\mathrm{Re}}. \qquad (19)$$

Therefore the Knudsen number can either be regarded as a ratio of the frequency of molecular collisions to wall collisions, or a ratio of the speed of a flow to its force balance. Most normal flows are subsonic and have $100 < \mathrm{Re} < 4000$, yielding Knudsen numbers much less than 0.001. Given the definition of the mean free path of a gas as

$$\lambda = \frac{kT}{\sqrt{2}\pi P d_m^2}, \tag{20}$$

where k is Boltzmann's constant, T is the absolute temperature, P is the pressure and d_m is the molecular diameter, one can estimate λ's for P and T where Kn is no longer very small. Based on these equations and the empirical results of other researchers, Gad-el-Hak divides micro flows into the following flow regimes [40]:

Table 4:Flow regimes for microchannels

Kn	Regime	Description
< 0.001	Continuum Flow	Classical Poiseuille flow
0.001 - 0.01	Slip-Flow Regime	Navier-Stokes flow with slip boundary conditions
0.01-10	Transition Regime	Gas behaves slightly rarified
> 10	Free-molecule flow	Gas behaves like a rarified gas

It is apparent from Table 4 that only slip and continuum flow are achievable at normal operating conditions for a micro fuel cell. The following graphs relate estimates of temperature to Kn for several different gasses with $D = 100$ μm and 50 μm.

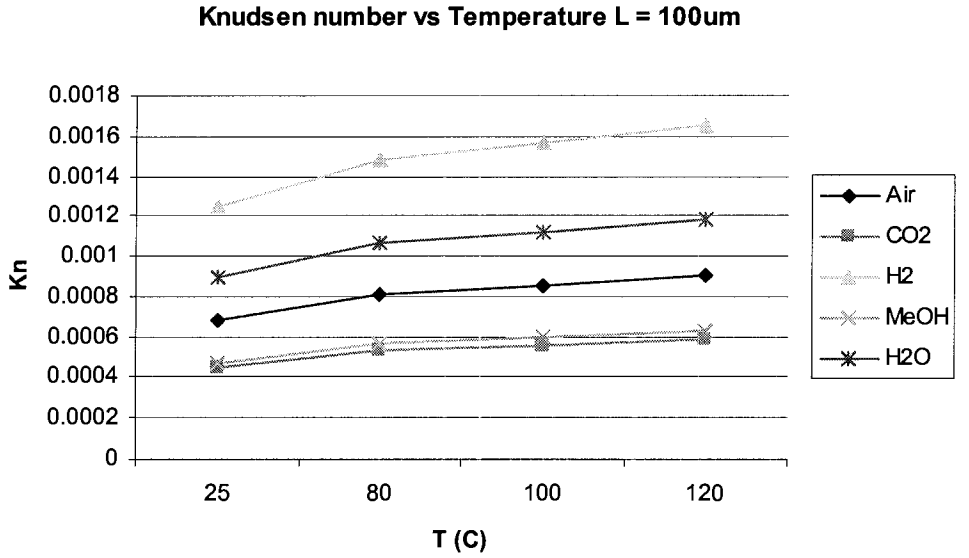

Figure 11: Knudsen number versus temperature for common fuel cell gasses, D = 100um

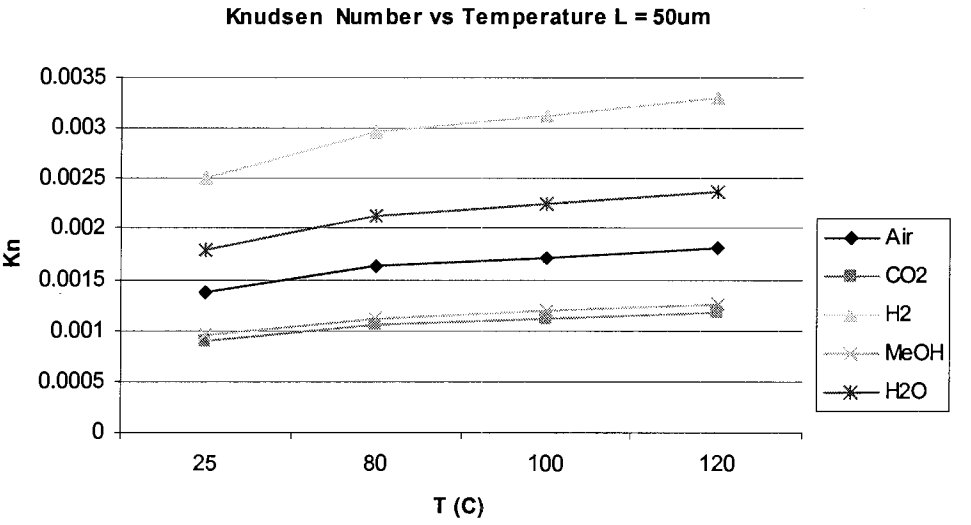

Figure 12: Knudsen number versus temperature for common fuel cell gasses, D = 50 μm

Given that the transition from no-slip to slip flow occurs at Kn = 0.001, micro channels containing water vapor or hydrogen gas are much more likely to encounter slip flow for D = 100 μm, and most gasses will exhibit some slip flow for D = 50 μm. The effect of slip flow is

difficult to determine because the normal boundary condition, fluid speed equal to zero at the channel wall ($y = 0$)

$$u(y=0)=0, \tag{21}$$

is replaced with the slip condition,

$$u\big|_{wall} = \sigma K \frac{\partial u}{\partial y}\bigg|_{wall}, \tag{22}$$

where σ_a is the accommodation constant, which is related to the tangential accommodation constant σ_m, varying from 0 (specular accommodation) or 1 (full accommodation) [38] by

$$\sigma_a = \frac{2-\sigma_m}{\sigma_m}. \tag{23}$$

Using a perturbation method, Arkilic *et al.* [38] achieved an approximate analytical solution for slip flow in a micro channel for systems with long length scales. The results of their analysis are

$$\tilde{p}(\tilde{x}) = -6\sigma_a Kn + \sqrt{(6\sigma_a Kn)^2 + (1+12\sigma_a Kn)\tilde{x} + (\tilde{p}_i + 12\sigma_a Kn\,\tilde{p}_i)(1-\tilde{x})}, \tag{24}$$

$$\dot{m} = \frac{H^3 w P_o^2}{24\mu LRT}\left[\tilde{p}_i^2 - 1 + 12\sigma_a Kn\left(\tilde{p}_i - 1\right)\right], \tag{25}$$

where a tilde represents a normalized quantity, subscript o represents an output, subscript i represents an input, a dot represents a time derivative, P is the outlet pressure, p is the local pressure, m is mass, and H, w, and L are the height, width, and length of the duct, respectively.

Of particular interest is (25), which relates a change in mass velocity to the slip condition, which is in the second term within the brackets. If the Knudsen number is small, then the slip term disappears, and normal Poiseuille flow is exhibited. This approximation can be used to estimate the first order effect that the slip flow will have on the system.

Letting $Kn \rightarrow 0$, in equation (24), the model prediction for no-slip flow is the result. Taking the ratio between the slip and no-slip solutions,

$$\frac{\dot{m}}{\dot{m}_{NS}} = 1 + \frac{12\sigma Kn}{\tilde{p}+1}, \qquad (26)$$

which can be used to evaluate the impact of the slip flow term on the overall system.

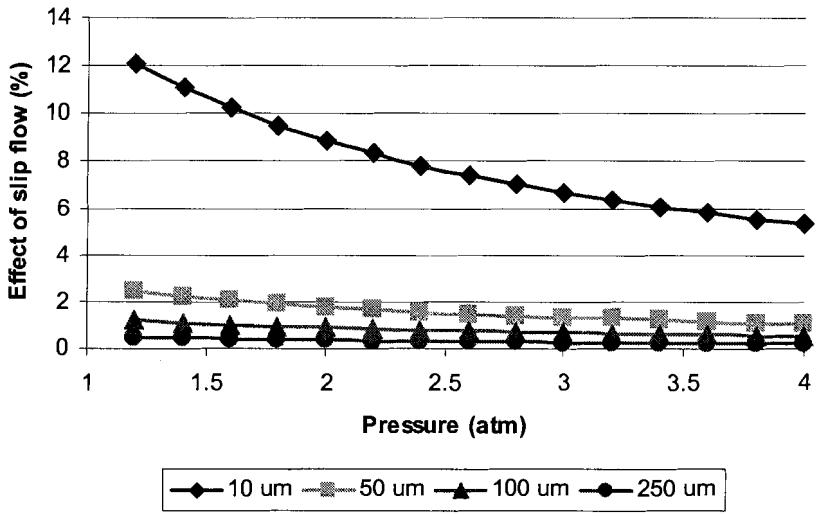

Figure 13:Slip effects for hydrogen

The above graph shows the effect of slip flow on microchannels of decreasing dimension under increasing pressure. Slip flow in this diagram is shown as the percent contribution to the flow rate from the slip component. It is apparent from the graph that all channels greater than 50 μm have less than 1% contribution from slip flow. Below 50 μm, the contribution

from slip flow doubles. While most micro fuel cell systems have characteristic dimensions of at least 100 μm, some micro fluidic components such as micro pumps and valves have constrictions of down to 10 μm. Slip flows at higher characteristic dimensions are relevant only for the impact they may have on calibration of flow control apparatus.

2.2.2.2 Bubble Formation and Two Phase Flow

The anode of fuel cells can produce a significant amount of carbon dioxide. Argyropoulos *et al.* [45] provide an excellent model for determining the two-phase behavior in macro DMFCs. Their model predicts that carbon dioxide saturation will occur within 10 cm of the inlet, even for relatively high flow rates of 0.01 dm^3/min. With similar current densities and much lower flow rates, carbon dioxide saturation of the fluid will occur much earlier. In addition, the 4 mm^2 channels exhibited bubbly flow, while the micro flow systems moved directly to cap or slug flow. The thermal effects that they reported would also likely be repressed at smaller scales and lower operating temperatures. An investigation of the behavior of carbon dioxide bubbles in micro channels would be of significant theoretical interest.

Bubble formation in micro channels is significantly different from bubble formation in macro channels. The size of the channel prohibits bubbly flow, as bubbles large enough to maintain structural integrity are of the same order as the channel itself. According to Xu *et al.* [46], while normal flow progressed from bubbly flow to slug flow to churn flow to annular flow, flow regimes below 3 mm progressed through cap-bubbly flow, slug-droplet flow and annular flow. Cap-bubbly flow was characterized by small slugs of gas. Slug-droplet flow was characterized by slugs of gas with suspended droplets inside. The annular flow regime was no different than normal annular flow. Their total channel length was less than 3 cm, so these effects are likely to be exacerbated over the length scales common to micro fuel cells.

Much of the micro two-phase flow literature pertains to micro heat sinks, and thermal bubble behavior. While the possibility exists for thermal bubbles formation within micro fuel cells, as in Lee *et al.* [47], Jiang *et al.* [48], and Hapke *et al.* [49], the heat flux rates required are higher than would be expected in a micro fuel cell. However, their observations of bubble formation and behavior during boiling can be instructive. In particular, they found that even though bubbles would form, they rapidly expanded to fill the inside of the channel, then either departed quickly or collapsed. Collapse of thermal bubbles is a normal effect of thermal transfer in flowing liquids. In DMFCs, bubbles at the anode form because of carbon dioxide saturation.

Qu and Mudawar provide a model for the formation of thermal bubbles at nucleation sites [50]. The model accounts for the surface tension forces, locking the bubble to the wall, with the dynamic forces due to the fluid flow moving past the bubble into account. They show that for a hemispherical bubble

$$F_d = C_d \rho_f u_c^2 A_p, \tag{27}$$

where F_d is the force due to drag, C_d is the drag coefficient, ρ_f is the density of the fluid u_c is the liquid velocity halfway from the nucleation site of the bubble tip and A_p is the projected area of the bubble. The surface adhesion is given by

$$F_s = \frac{C_s}{4} \sigma P_c (\cos\theta_r - \cos\theta_a), \tag{28}$$

where P_c is the contact length given by

$$P_c = 2\pi r \sin\theta, \tag{29}$$

where F_s is the surface force, C_s is an empirical constant, σ is the surface tension, θ is the average contact angle, θ_r is the receding contact angle and θ_a is the advancing contact angle. The key point is the very small value of F_s. For bubbles even 100 μm across the surface force is in the millinewtons. Substituting (29) into (28)

$$F_s = \frac{C_s}{2}\sigma\pi r \sin\theta(\cos\theta_r - \cos\theta_a). \quad (30)$$

In this maximum case, the potential for the force to grow is small because the contact length is much shorter than the overall length of the cell. The pressure drop required to move the bubble is

$$\Delta P = \frac{C_s}{2r}\sigma \sin\theta(\cos\theta_r - \cos\theta_a). \quad (31)$$

For water in a 100 μm channel the pressure difference is approximately 350 Pa or 0.05 psi. For a simple bubble the resistance is small; however, for multiple bubbles, this loss is accumulated. Moving a single bubble is trivial, moving 10 bubbles is significant, and moving 100 bubbles is prohibitive. This behavior can be anecdotally observed in intravenous drip systems where plugs of gas travel down the tube with only modest pressure head. However, such a bubble could be potentially disruptive for a diffusion driven micro fuel cell as methanol would have to evaporate and condense at either side of the bubble for transport.

Because bubble surface tension only scales as the radius, it will always be dominated by the pressure loss in micro fuel cell systems. In systems where the length and flow rates are small, as is the case in many micro fluidic systems, bubbles can have a significant impact. Researchers such as Kim are correct in assuming that surface forces predominate at micro scales [51]. However, the length scale must be consistent to realize these effects. Bubbles

would only be a concern if the frequency of blocking bubbles were proportional to the length scale. If a the pressure drop due to a single bubble is relevant at a 1 cm scale, then 100 simultaneous blocking bubbles would be relevant for a 1 m long channel.

2.2.2.3 Summary of Flow Field Impact

Because micro fuel cells exhibit both micro and macro scale aspects, micro-scaled hydraulic diameters, and macro-scaled lengths, both effects must be considered when designing fuel cells. Generally, at lower velocity and smaller channels, micro effects become more dominant. At higher velocities, cumulative effects such as pressure drop dominate. For liquid systems continuum effects are more serious because the viscosity is higher, exacerbating the laminar pressure drop and mixing effects. Schematics showing the impact of the flow field diameter and length are shown in Figure 14 and Figure 15 for both gas and liquid transport. These diagrams are only general guidelines, not deterministic relationships for use in designing micro fuel cell systems.

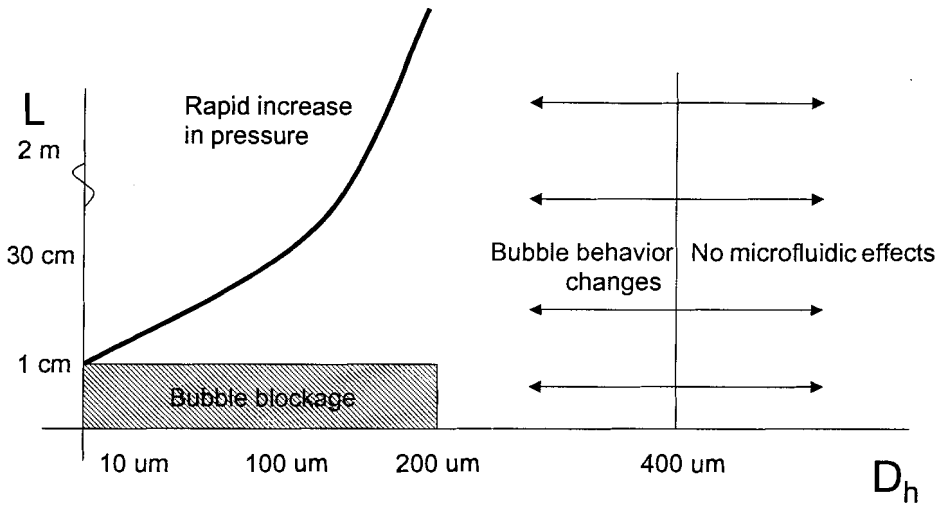

Figure 14:Flow field effects for liquid transport at micro scales

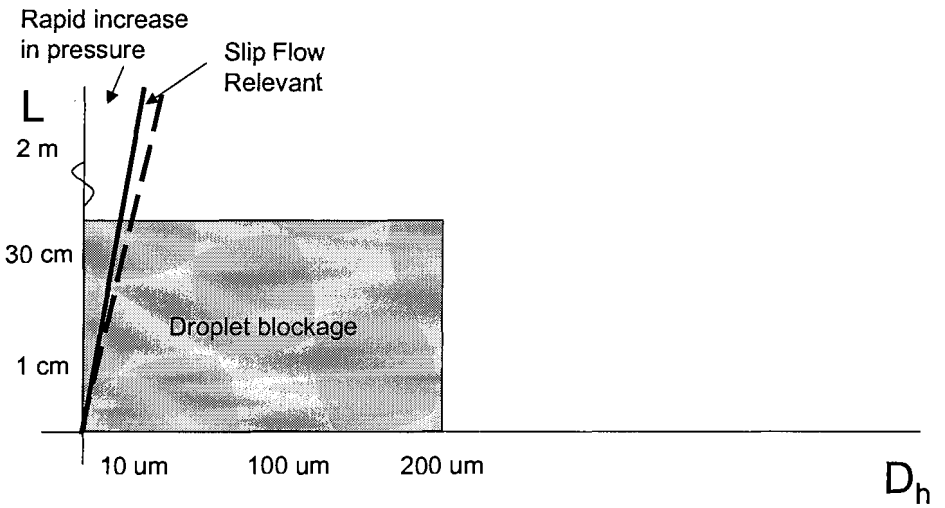

Figure 15: Flow field effects for gas transport

In the above diagram, the horizontal axis represents the hydraulic diameter, and the vertical axis represents the total channel length. Bubble blockage represents the size of channel where trapped bubbles or droplets become relevant to the total flow behavior. Above 400 μm in liquids and above 200 μm in gasses, micro fluidic effects are negligible and only continuum effects must be considered.

The total channel length is determined by the MEA surface area, which is in turn defined by the desired power output. Altering the hydraulic diameter is the primary method of controlling the flow characteristics in the system. For micro fuel cells, volume should be minimized. Micro fuel cells should have the minimum flow field volume possible to maintain the flow required by the power output of the system. For small cells, gas transport cells, or systems which run at lower power densities, a floor of 200 μm for the hydraulic diameter is advisable. For longer fuel cells or fuel cells which require higher mass transport rates, the hydraulic diameter is determined by the back pressure available.

2.2.3 DMFC Governing Equations

Many researchers have modeled the operation of direct methanol fuel cells [55-72], with special attention paid to the operation of the proton exchange membrane and the issue of methanol cross over. Most of the attention is paid to the anode side because the cathode transport is almost identical to the hydrogen PEM transport, which is already well covered in the literature [45].

The DMFC is very similar to the hydrogen PEM in many ways; (structurally it is identical) however because the fuel is a hydrocarbon rather than pure hydrogen, the chemical reactions are more complex. The catalytic oxidation of methanol is a complex multi-stage process. The precise process is not relevant to this analysis.

The protons migrate through the proton exchange membrane and the electrons migrate around the external circuit. The carbon dioxide remains in the anode and must be purged. In aqueous methanol feed solutions, carbon dioxide gas can rapidly reach 40 % of the channel volume [45]. In micro fuel cells this is a significant problem because large bubbles can form valves, which block the flow of reactants and limit the operation of the cell [13].

The second major difference between PEM and DMFC cells is the selectivity of Nafion and other common PEM membranes to methanol. Nafion is impermeable to gasses, but it conducts small ionic species, such as hydrogen ions, metallic ions, and aqueous methanol very well. For even moderate concentrations of methanol, between 1 and 3 M, significant concentrations can diffuse through the membrane and oxidize on the cathode catalyst directly, degrading both fuel utilization, and cell performance [45].

2.2.4 MEA Modeling

Most of the modeling for the direct methanol fuel cell has focused on the membrane electrode assembly, the area where the chemical reactions occur. Although earlier characterization attempts had been made, Scott and his team in the University of Newcastle were the first to publish a series of papers relating the observed behavior of the fuel cell to specific transport phenomenon [45, 55-58]. Scott and his colleagues determined that the choice of aqueous or gaseous methanol was a critical decision that affected most of the other modeling steps. Particularly worrisome was the formation of large carbon dioxide bubbles and then streams as the fuel cell was run at high power densities. They managed to create a flow field to accommodate the release of the gas, but were still uncertain about aqueous methanol as a fuel.

Kulikovsky *et al.* [59,60] extended the Scott's model for a gaseous cell, and analyzed the role that structure played on the mass transport of gasses and conduction of electrons. His analysis showed that in a typical graphite plate cell, most of the electrons were collected along the steps of the risers, as there was no bulk current collector directly over the channel. He then proposed a theoretically interesting, but practically difficult embedded collector that would move electrons more efficiently. In his second paper, he addressed water management at the cathode, and found that a change in the topology of the cell could reduce the impact of water formation and transport degradation.

Meyers and Newman [61] published a series of detailed papers on the operation of the direct methanol fuel cell. Although their work was theoretically interesting, and included the first real treatment of thermodynamic phenomenon, the results were too esoteric to be of practical use. Their findings echoed the earlier work of Scott, adding detail but little new

understanding. Later Meyers and Maynard [62] published a follow up paper where they demonstrated that mixed planar fuel cells (interdigitated anode and cathode flows on the same substrate) suffered massive scale up problems when compared to the more traditional membrane-sandwich approach shown in Figure 1.

Finally, Jeng and Chen [63] have very recently published a relatively simple and useful model of the operation of a DMFC anode. This very complete derivation includes several terms relating to the transport of liquid water through the diffusion and catalyst layers, and its effect on the transfer of methanol. However, these effects are not present in the vapor phase fuel cell we are proposing.

The most complete and useful description for the operation of a gaseous direct methanol fuel cell can be found in [56] and [59]. We have opted for the derivation of Kulikovsky in [59], excerpts of which are presented below. Kulikovsky uses Rothfeld's model [64] to express the combined Stefan-Maxwell and Knudsen diffusion through the diffusion and catalyst layers.

$$\frac{G_k}{D_k^K} + \sum_l \frac{c_l G_k - c_k G_l}{D_{kl}} = -c_T \nabla c_k \,, \qquad (32)$$

where G is the flux, c is the concentration, D^K is the Knudsen diffusion coefficient, D is the binary diffusion coefficient, subscripts l and k denote gas species, and the subscript T denotes the total concentration. While combined Knudsen and Stephan-Maxwell diffusion is the most accurate representation of mass transport within the gas diffusion and catalyst layers of the fuel cell, for the an air breathing DMFC, Fickian diffusion is sufficiently accurate for most calculations. The mass conservation equation is given by

$$D_{eff}\left(\nabla \cdot G_k\right) = R_k\,, \tag{33}$$

where R_k is the rate of consumption/production in the reactions and D_{eff} is the effective diffusion coefficient.

Kulikovsky uses exponential Butler-Volmer style equations to link the rate of reaction with the potentials at the anode, cathode and membrane. This approximation is valid at moderate current draws and potentials.

$$R_a = i_0^{ref}\left(\frac{c_{MeOH}}{c_{MeOH}^{ref}}\right)^{\gamma_a} e^{\frac{\alpha_a F}{RT}(v_a - v_m)}, \tag{34}$$

$$R_c = i_0^{ref}\left(\frac{c_{O_2}}{c_{O_2}^{ref}}\right)^{\gamma_c} e^{\frac{\alpha_c F}{RT}(v_m - v_c)}, \tag{35}$$

where subscripts a and c denote anode and cathode, superscript *ref* corresponds to a normalizing reference value and α is a reaction constant.

Proton flux through the membrane and catalyst layers obeys Fick's Law, but can be treated as Ohmic for simplicity. Assuming a sufficient supply of reactants on either side, and using the diffusion constants, and current draw, it is possible to solve the system of differential equations for the gas transport and electron flow through the system. Cruickshank and Scott [57] provide a simple algebraic and empirical model for the methanol crossover in a gaseous methanol fuel cell. They derive the methanol flux through the membrane as

$$G_{MeOH} = \frac{\frac{D_{MeOH,m}c_l}{h} + \frac{\psi I}{nF}}{1 + \frac{D_{MeOH,m}}{kh} + \frac{K}{kh}\Delta P} \tag{36}$$

where $D_{meOH,m}$ is the diffusion coefficient for methanol in the membrane, n is the number of moles, h is the thickness of the membrane, ψ is the ratio of moles of methanol to proton, k is the rate of permeate removal (methanol transferred to but not oxidized at the cathode), and K a rate constant related to the permeability of water. The parameters k and K are determined experimentally as

$$k = 2.75 \times 10^{24} e^{\frac{-22187.5}{T}}, \tag{37}$$

$$K = 1.17 \times 10^{19} e^{\frac{-19098}{T}}. \tag{38}$$

Adding this empirical model as an additional flux to the above model generates a reasonably complete description of mass transport within the MEA.

Therefore, in this analysis we will only consider isothermal mass transport in the fluid channels, and the diffusion of species into and out of the catalyst layer. A simple two-dimensional diagram of a single channel is shown in Figure 16.

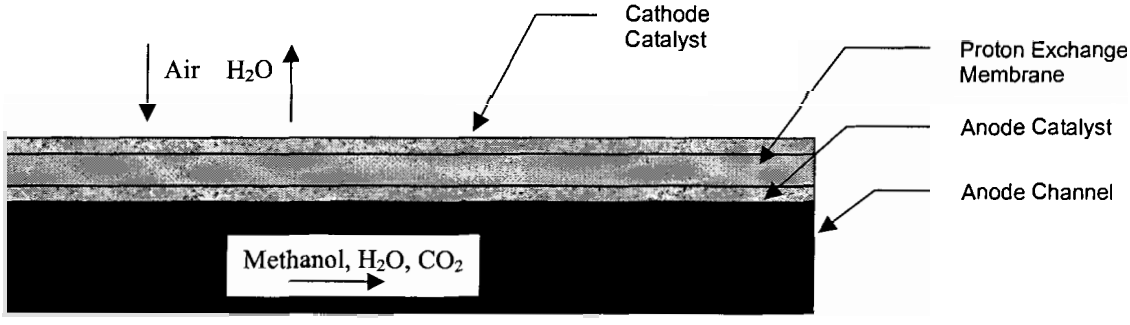

Figure 16: View of Species Flow in a Single Channel

The equations that govern the operation of our cell follow. Equations presented earlier in the theoretical discussion and literature review are restated here for ease of reading.

2.3 Finite Element Analysis

Finite element analysis (FEA) and computational fluid dynamics (CFD) are computational analysis techniques that provide numerical solutions for engineering systems, which are too complex or impossible to solve with analytical techniques. Fuel cell systems are excellent candidates for CFD analysis because of the complex interplay between chemical, physical, electrical, and thermal phenomenon.

Both FEA and CFD generate numerical solutions. What separates FEA and CFD from strict nonlinear solvers is the inclusion of geometry and geometric effects. CFD in particular is extremely useful for solving problems with geometries that cannot be expressed easily as geometric primitives such as cylinders or trapezoids. CFD technology has a long history in fuel cell research. It is beyond the scope of this work to provide a complete literature review and analysis of CFD and FEA work in fuel cells in general. We do not attempt to extend CFD and FEA beyond the current state of the art in fuel cell modeling, rather we use the existing fuel cell models and modeling systems, as described in the literature to motivate the design of micro fuel cells in general, and micro fuel cell electrodes in particular--something which has not been reported in detail in the literature.

2.3.1 FEA Overview

The fundamental building block of a FEA system is an element. A fluid element is a smaller volume than the geometric scale of the most significant effects. By dividing the problem into a series of finite fluid elements, the problem can be solved locally, on simple geometries and as the solution converges on larger, more arbitrary geometries. A diagram of a fluid element is shown in Figure 17.

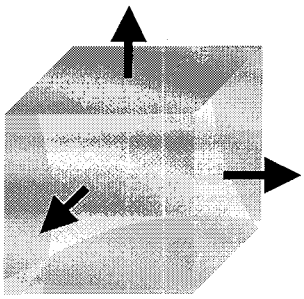

Figure 17: Fluidic element

Any heat, mass, or charge entering one of the faces or created within the body of the element must be matched by an equal amount leaving one of the faces or sunk within the volume. The mechanism dictating the transfer of properties through the faces is the physics being modeled. For example in the catalyst layer of a fuel cell, charge is transferred from cell to cell according to Ohm's law, mass is transferred by diffusion, and chemical species are converted according to the Butler-Volmer relation.

2.4 Impact of Edge Collection

In most micro fuel cell systems, edge collection is used because it is convenient at small scales using thin films. Edge collection has an impact on micro fuel cell system efficiency. In edge collection, current flows laterally from one side of the electrode to another instead of vertically from one cell to the next through a bulk conductor. Edge collection is shown in Figure 18.

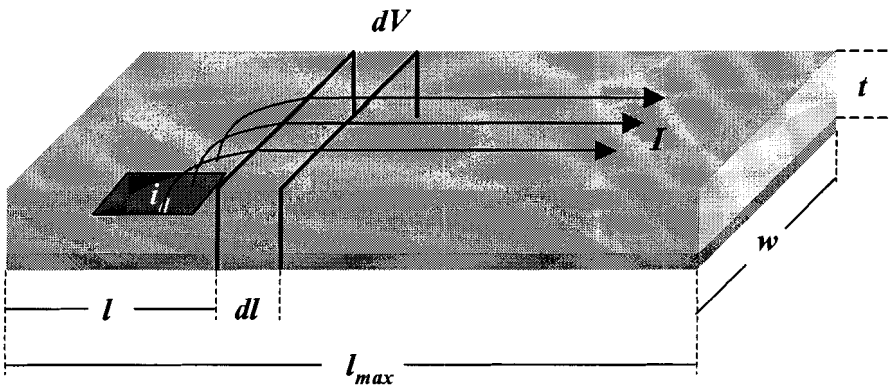

Figure 18: Edge collection through GDL

In Figure 18, the top block represents the bulk current carrier, such as the gas diffusion layer, and the lower block represents the catalyst layer. Current flows from left to right from l = 0 to l_{max} in small steps dl. Width and conductor thickness are denoted by w and t, respectively. Current generation is represented by the current density i_d, which depends on the operating parameters of the fuel cell. The incremental voltage drop for the next small segment of the conductor is represented by dV. Equation (39) provides the course upper boundary of the potential drop (V_t) along the electrode, assuming the maximum current (I_{lmax}) occurs along the entire electrode length, where σ_{GDL} is the conductivity of the GDL.

$$V_t < I_{l_{max}} \frac{l_{max}}{\sigma_{GDL} wt}. \qquad (39)$$

The total potential drop is bounded by the maximum current across the entire length of the electrode. Intuitively, the potential drop is less than (39) because the total current I_{lmax} only flows through the final small segment l_{max}-dl and only a very small current $i_d wdl$ travels the entire length of the electrode.

2.4.1 Edge Collection Model Derivation

For a strongly forward biased reaction, the relationship between potential, current, and operating conditions for a fuel cell electrode is given by the Butler-Volmer relation,. The current generated over a length l is

$$I(l) = wli_d, \tag{40}$$

the resistance seen by the accumulated current over a small increment dl is

$$R(dl) = \frac{dl}{\sigma_{GDL} wt}, \tag{41}$$

therefore the voltage drop given by Ohm's law is

$$dV = \frac{ldl}{\sigma_{GDL} t} i_d. \tag{42}$$

Because dV is proportional to i_d, the resulting equation is transcendental, and therefore no closed form solution exists. Approximations for this relation can be found using FEA and CFD techniques. However, an analytical approximation can be derived by assuming that i_d is constant. This approximation is reasonable for voltage losses due to edge collection for small to moderate impedances. While the actual distribution of potential and current density may not precisely reflect the operation within the fuel cell, a constant current approximation can be used to design electrodes based on input-output requirements.

For the constant current density approximation, (42) can be solved using

$$\int dV = \int \frac{ldl}{\sigma t} i_d, \tag{43}$$

$$V_l = \frac{l^2}{2\sigma_{GDL} t} i_d . \qquad (44)$$

Comparing (38) to (43) we find that

$$\frac{l_{\max}^2}{\sigma_{GDL} t} i_d > \frac{l^2}{2\sigma_{GDL} t} i_d . \qquad (45)$$

It is apparent from (45) that our new estimate reduces the potential drop when compared with the maximum estimate. The validity of the estimation must be established using numerical solutions because the actual equation is transcendental.

Several conclusions can be deduced from (45). First, the potential drop is proportional to the square of the distance the current must travel. Thus, large fuel cells using edge collection will be inherently inefficient. However, for small l, the impact of edge collection can be acceptable compared to the simplicity of the fuel cell manufacturing. Second, the voltage loss is independent of the electrode width. Although the resistance decreases with increasing width, the total current drawn increases with increasing width, leading to an identical potential drop. To reduce the potential losses, the current collector thickness or conductivity needs to be adjusted. Electrode dimensions and current density are primarily determined by the performance and size requirements of the system.

For systems where a high conductivity thin film current collector is used in conjunction with the GDL, then the resistance is given by a simple parallel resistance.

$$R(dl) = \frac{dl}{w\left(\sigma_{GDL} t_{GDL} + \sigma_{TF} t_{TF}\right)}, \qquad (46)$$

where σ and t refer to conductivity and thicknesses and the subscripts *GDL* and *TF* refer to the gas diffusion layer and thin film respectively. Obviously, the net resistance will always decrease with the additional of another parallel conductive layer. However, in order for the conductive layer to have a significant impact, the conductivity of the thin film must be several orders of magnitude greater than the GDL because the thin film thickness is significantly less than the GDL thickness. The complete voltage drop expression including the thin film current collection is

$$V_l = \frac{l^2}{2(\sigma_{GDL} t_{GDL} + \sigma_{TF} t_{TF})} i_d . \qquad (47)$$

Equation (47) takes the total current flowing through an incremental segment of the GDL into consideration. The following assumptions are inherent in (47).

1. Current density does not vary with length.
2. Conductivity is isotropic and invariant with length.
3. Conductor thickness variations are small compared with the total thickness.
4. The fuel cell is operating in a regime where Ohmic losses predominate.

For a given current density, the potential drop can be minimized by changing the geometry of the electrode, by changing the GDL and current collector materials, or by changing the thickness of the conductor. Changes in geometry are often difficult to achieve given the form factor constraints dictated by the application. Changes in material are limited by compatibility and desirability. Few fuel cell compatible materials have a higher electrical conductivity than graphite. GDL thickness can be adjusted to decrease the real resistance, but the thickness of the GDL also affects the mass transport of reactants and products in and out of the electrode.

Using the general constraints and geometries described in the previous chapter, and the manufacturing techniques described in the next, the following current collection geometries are possible.

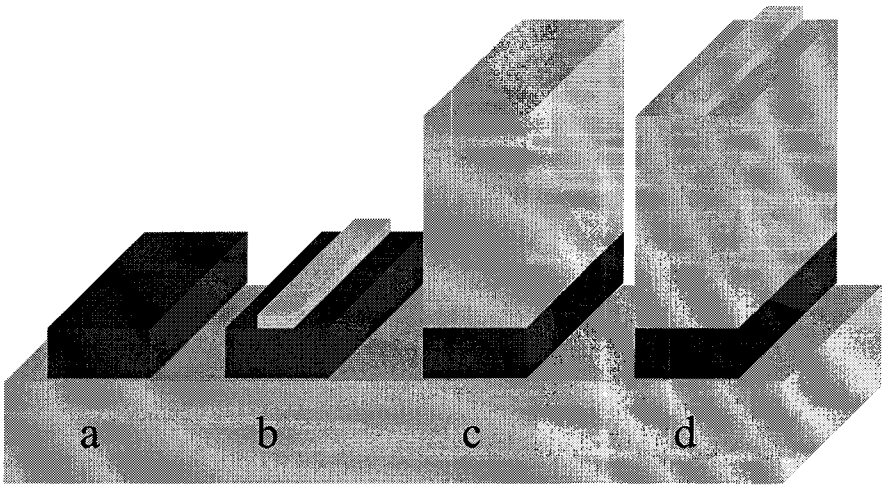

Figure 19: Possible edge collection geometries:
(a) catalyst only (b) catalyst and thin film current collector
(c) catalyst and GDL (d) catalyst GDL and thin film collector

In the catalyst only case, (a), current is created and drawn directly from the catalyst. In the catalyst and thin film case, (b), the situation most common in uncompressed fuel cells, the catalyst layer, either a classic packed bed, or an electroplated or sputtered film, routes current locally, but the thin film current collector routes current globally. Generally these current collectors are deposited directly above or adjacent to the catalyst layer. In (c), the current is directly collected through the GDL. In (d), the current is collected through the GDL and the thin film current collector. Because the conductivity of the GDL is much greater than the conductivity of the catalyst layer, in (c) and (d), we assume current travels vertically through the catalyst layer.

In the case of current collectors deposited directly on the catalyst or gas diffusion layers, the rough surface of the conductors leads to breaks in the thin film, forcing current to hop or

tunnel through portions of the catalyst layer and GDL. In the case of compressed and assembled systems where the thin film is deposited on the flow fields, there are voids where the GDL does not contact the thin film collector. To compensate, the thin film electrodes are approximated as thick film electrodes with a lower conductivity but greater thickness, not to exceed the actual conductivity of the thin film layer. The following table shows the electrical conductivities for each of the layers. These conductivities were determined experimentally and are presented in chapter 3.

Table 5:Material properties for edge collection potential loss calculations

Material	Thickness (μm)	Conductivity Low (S/m)	Conductivity High (S/m)
Catalyst	20	50	250
Catalyst + thin film	5	50k	50k
GDL	100	10k	50k
GDL + thin film	5	500k	1000k

Obviously, minimizing length has the maximum return in reducing loss. However, minimizing length changes the power output of the system, so there is limited play in the variable. However, the length term can provide a practical upper limit for edge-collected design. A hard limit for losses in a fuel cell electrode exists. Neglecting Ohmic and mass transport losses, kinetic losses for direct methanol fuel cells generate a practical maximum potential of 0.7 V. Any system with Ohmic losses greater than 0.7 V is physically unrealizable. Figure 20 illustrates the maximum length for an edge collected electrode for single conductor (GDL only) and mixed conductor (GDL and thin film) systems.

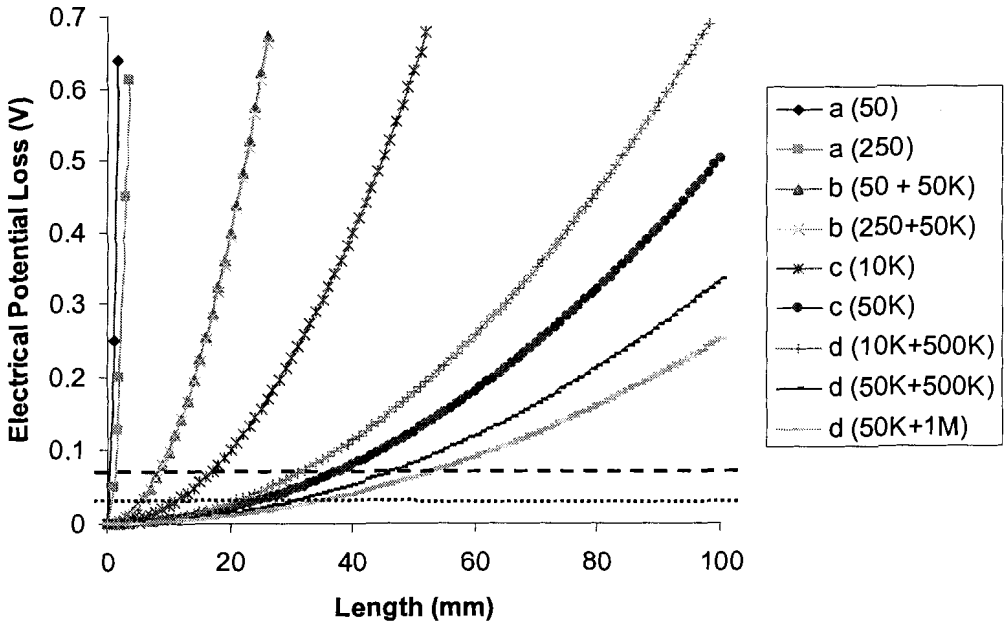

Figure 20:Edge collection losses with respect to conductivity and electrode length

The vertical axis in Figure 20 corresponds to the estimated Ohmic loss in a fuel cell with edge collected electrodes. Losses due to activation, crossover, ionic resistance and mass transport effects are not included. Losses were calculated at a current density of 50 mA/cm^2, a reasonable operating point for a micro DMFC. The horizontal axis corresponds to the length of the electrode in millimeters. Each curve in the graph corresponds to a single geometry and a set of conductivity and thickness. The curve name corresponds to a geometry shown in Figure 18, and the curve value corresponds to a set of material properties listed in Table 5. Curves are truncated at approximately 0.7 V, corresponding to a loss of all available potential due to Ohmic heating of the electrode. While 0.7 V is a physical maximum, much smaller losses are acceptable in practice. The dashed line in Figure 20 corresponds to a 10% (0.07 V) loss through the electrode, the dotted line corresponds to a 5% (0.035 V) loss through the electrode. We have arbitrarily chosen these as low loss figures. Application specific design

criteria must be analyzed to determine acceptable losses for particular systems. Several design parameters are can be deduced from this diagram.

1. Edge collected systems are only practical for micro fuel cells systems. Even with very high conductivities in the GDL-thin film configuration, losses are unacceptably high for electrode lengths beyond 60 mm. Given that typical fuel cell plates are at least 300 mm in diameter, those losses are unacceptably high.
2. Catalyst only systems are constrained to extremely small (<1 mm) or extremely low power devices. Even in low power devices most of the energy created by the fuel cell will be expended heating the electrodes. While these systems may have academic interest, they will never be practical.
3. A high conductivity catalyst layer in conjunction with a thin film electrode is superior to a GDL only system, if the GDL conductivity is low. In all other cases, GDL based systems have superior performance over systems with only catalyst layers.

Further design parameters can be extracted by considering only the region within practical limits, bounded by 0.07V as shown in Figure 21.

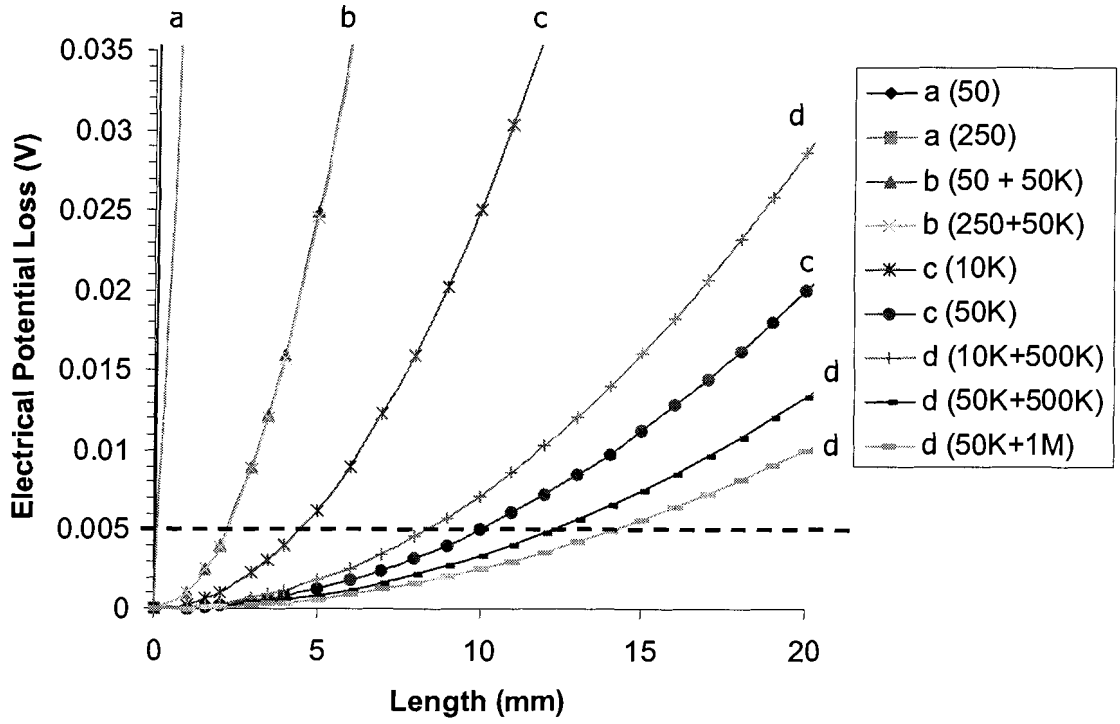

Figure 21:Low potential drop regime for edge collected electrodes

The curves in this diagram are identical to the curves in Figure 20, however, the scale has been increased to examine the design tradeoffs for practical fuel cells instead of in the limit of operation. The dashed lines correspond to a practical loss (5 mV) and length (10 mm). For the operating point of 50 mA, the 50 kS GDL only system, and all the GDL and thin film systems provide adequate performance. For very small losses (1 mV or less) denoted by the dotted line, only highly conductive electrodes less than 5 mm in length are realizable. Thicker GDLs or thin film conductors may improve performance, but cost and mass transport implications exist for both situations. The following design parameters can be extracted from the graph.

1. A declining return exists for increasing the conductivity of the thin film collector. A doubling of the conductivity only generates a savings of 1 mV at 10 mm.

2. It is almost impossible to achieve losses of less than 1 mV at 50 mA. Small current densities or very small electrodes can be created, but significant current generation will inflict losses.

3. Practical edge collected fuel cells are possible to create, but only for small systems, with electrode lengths less than 30 mm.

2.4.2 Approximation Verification with FEA

We have analytically verified that our constant current density approximation is more accurate than the worst-case approximation; however the validity of the approximation cannot be verified analytically. To determine the validity of our approximation, FEA analysis was used to numerically determine the solution to the system of equations for an edge-collection.

A two dimensional lengthwise simulation was performed. Only the cathode was simulated. Mass transport by diffusion was modeled by Fick's Law, and assumed to be entirely in the vapor phase. Potential losses in the liquid and solid phase obeyed Ohm's Law. Electrochemical effects were modeled using the Butler-Volmer relation, assuming a strong forward bias. A parametric solution was generated, solving for solid phase potentials between 1.2 V and 0.75 V with a course resolution (0.01 V) and between 7.5 V and 6.0 V with fine resolution (0.001 V). The physical parameters used in the model are recorded in Table 6.

Table 6:Parameters used in verification simulation

Parameter	*Value*	*Parameter*	*Value*	*Parameter*	*Value*
σ_l	1 S/m	D_{eff}^{cat}	$8.3\text{x}10^{-7}\text{m}^2/\text{s}$	O_2^{ref}	3.66mol/m^3
σ_{GDL}	10kS/m-50kS/m	D_{eff}^{GDL}	$2.5\text{x}10^{-6}\text{m}^2/\text{s}$	i_0	0.001A/m^3
σ_{TF}	500kS/m-1MS/m	O_2^b	8.7mol/m^3	S_c	$1\text{x}10^9\text{m}^2/\text{m}^3$
V_s	1.2V-0.7V	H_2O^b	0.45mol/m^3	α	0.5
V_l	-0.4V	T	298K	F	96485

The potential with an output current density of 50 mA/cm^2 was taken as the result. Electrode lengths of 5 mm, 7.5 mm, 10 mm, and 15 mm were modeled. The potential drop includes both kinetic, Ohmic, and coupling effects, in both the solid and ionic phases. The solid phase potential drop was recorded and compared to the predictions made by the approximation. Ionic drop was not included because the geometry of ionic transport is bipolar in all the geometries investigated here.

Figure 22 shows the results for a simulation run for a 5 mm electrode with 50kS/m GDL and 700kS/m thin film. The solution shown has a 0.7 V solid phase boundary. The trace lines represent the current path. The grayscale of the trace represents the potential at that point, the bar on the right shows the maximum and minimum potential.

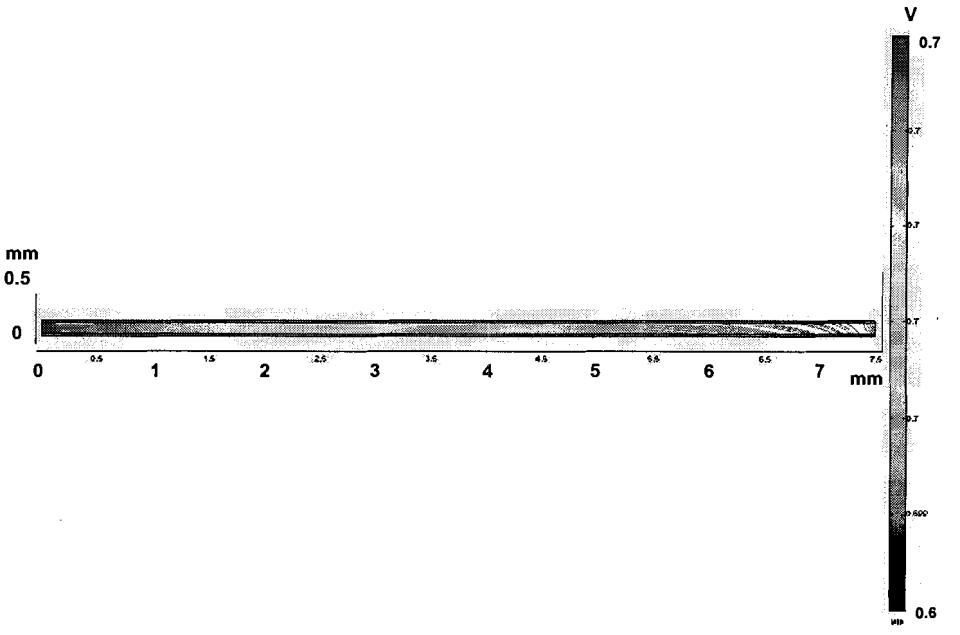

Figure 22: Edge collection simulation

The minimum potential is 0.699 V and the boundary potential is 0.7 V, leading to an Ohmic drop of 1 mV. The drop occurs end-to-end, not top-to-bottom as expected. This numerical solution better reflects the actual performance of the electrode because it includes

the electrochemical Butler-Volmer equation. Results for 5 different combinations of solid phase conductivity are shown in Figure 23.

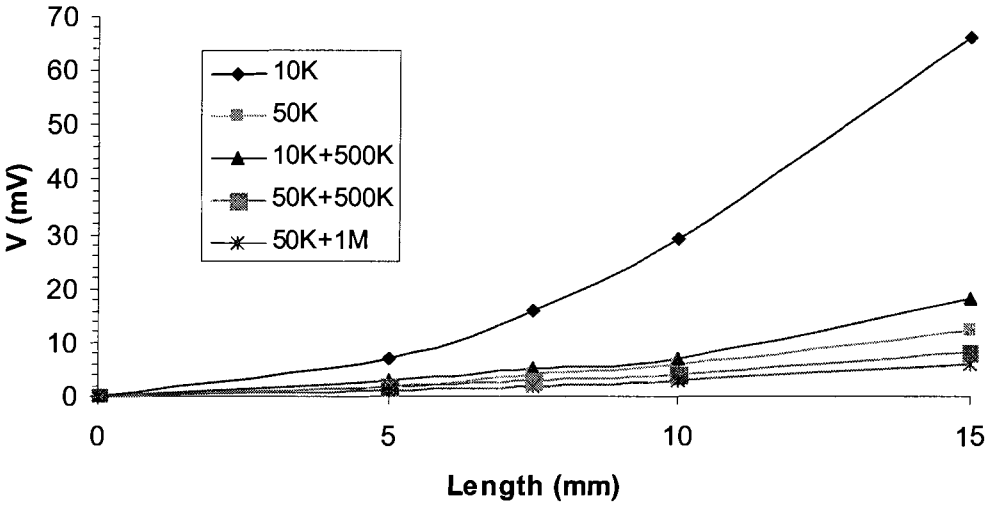

Figure 23: Simulated edge collected electrode results

The results are shown for the range of potential of 0 – 70 mV, or the range of acceptable losses for practical micro fuel cells. Only GDL based systems are shown in Figure 23 because catalyst and thin film systems have insufficient performance for practical fuel cells. The characteristic second order behavior is present in the numerical solutions as well. A comparison of simulated and approximated solutions is shown in Figure 24.

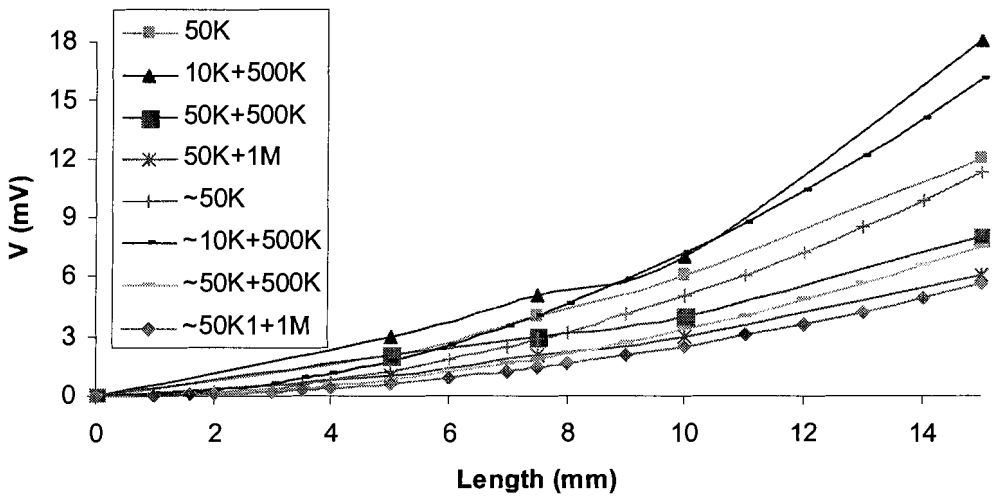

Figure 24:Comparison of approximation and numerical solutions

Curves denoted by a tilde correspond to approximate solutions, whereas curves without tildes are numerical solutions. The approximate solutions approximate the numerical solutions. In all cases, the approximate solutions slightly underestimate the value returned by the numerical solution. However, both agree by less than 1.5 mV, which is an acceptable discrepancy for fuel cell systems. Given the complexity of fuel cells, it is unlikely that any model is with 1.5 mV of the operation of the fuel cell for all operating conditions. The magnitude of the error for smaller conductivities and larger losses begins to increase. The following chart shows only the approximate and numerical solution for the10 kS/m GDL only case.

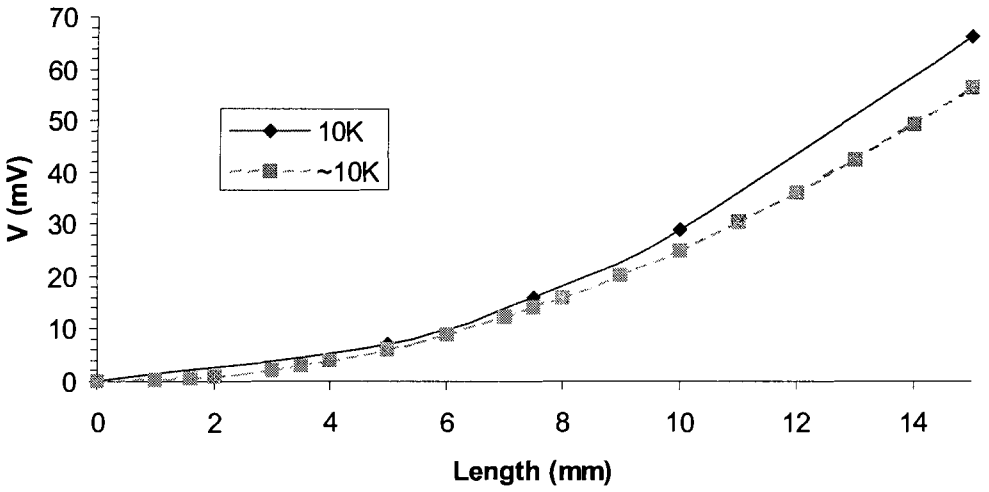

Figure 25:Discrepancies between approximate and numerical solutions

The maximum error of 10 mV occurs at the maximum length of 15 mm. It is also clear from the graph that the solutions diverge with increasing length. We can conclude that the greater the predicted loss, the less accurate the approximation. This divergence is not surprising considering the key assumption underlying the approximation. By assuming that the current is constant everywhere, the local effects amplified by the Butler-Volmer relation is removed. As the interaction becomes more pronounced, the validity of the underlying assumption becomes more tenuous. The systematically lower potential drop predicted by the approximation can also be explained by the impact of the assumption.

2.4.3 Summary of Edge Collection Effects

For the purpose of fuel cell design, loss of accuracy at high potential drops is not critical. If fuel cell design exhibits a significant potential drop according to the approximate solution, the design can be discarded. The actual error can be neglected as the design is not practical. For architectures with acceptable levels of performance, below 3.5 mV of Ohmic loss at 50 mA, the approximation is sufficiently accurate and can be used to predict performance. The

approximate solution can be used to quickly evaluate the feasibility of an edge-collected designs, and determine the operating losses for sufficiently conductive electrodes.

2.5 FEA Analysis

Based on our calculations, edge collected systems are only appropriate for fuel cells operating at moderate to low current densities over short lengths. Because edge collection effects are independent of the width, we assumed that only the geometry in the z direction significantly affects the performance. The electrode we consider is shown in Figure 26.

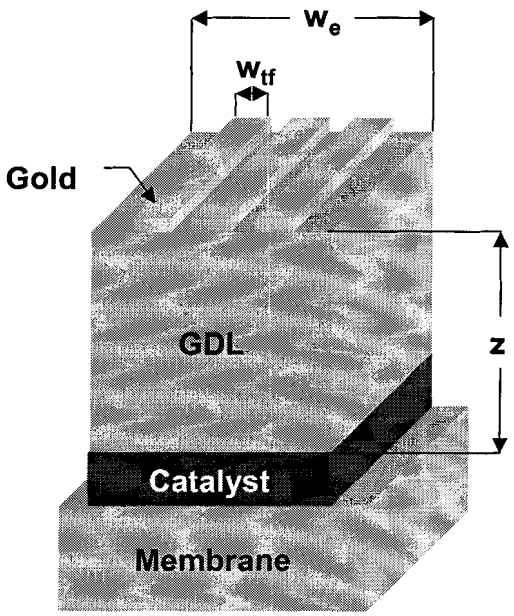

Figure 26:Schematic of the edge collected electrode considered in FEA analysis

However, this approximation only holds true if geometry effects due to edge collection are much less than the geometry effects due to the profile of the electrode. Electron flow is not necessarily uniform over a cross-section of the fuel cell. To analyze the impact of electron flow over the cross section of the architectures of the electrodes, and determine the impact of electrode kinetics on reaction kinetics and mass transport, we have examined the architectures in Figure 19 using FEA models.

The FEA analysis of potential micro fuel cell electrodes focuses on the behavior at the cathode. We examined the cathode because anode effects in DMFCs are well understood [54-63] and the behavior of completely passive cathodes, such as those found in micro fuel cells is less understood. Electrical effects such as Ohmic losses depend primarily on the architecture of the electrode and not the specific reaction occurring at the electrode. Therefore, generalizations about electrical behavior can be made on either the anode or the cathode. While the anode side must be controlled for fuel concentration and temperature, the cathode is directly exposed to the ambient environment. The effects of ambient temperature and humidity on passive air breathing cathodes are a gap in the micro fuel cell literature.

2.5.1 Model Parameters

A PEM (proton exchange membrane) fuel cell electrode is usually composed of three layers. The active catalyst layer or gas diffusion electrode (GDE) layer is composed of dispersed catalyst and ionic conductors. The gas diffusion layer is a porous electrolyte conductor responsible for distributing reactants and products and routing electrons to the active layer. Above the GDL layer is a bulk current collector. In larger cells, this collector is formed by the rib of the flow field (see Figure 1). In the micro fuel cell designs considered here, the current collector is a thin film conductor, either on the rib of a flow field or deposited directly on the GDL.

The governing equations for diffusion and electrical current conduction were defined in all domains except the membrane. Proton transport was defined on the catalyst and membrane layers because ionic conductors are not present in the gas diffusion layer.

Both ionic and electric current transport, are modeled using Ohm's law normally stated as

$$V = IR\,, \tag{48}$$

or differentially as

$$-\nabla(\sigma\nabla V) = Q_j\,. \tag{49}$$

The gradient of the current leaving the volume is equal to the source term Q_j. The conductivity, σ, is defined for each layer according to experimental results. The source term is zero everywhere but the catalyst layer where it is determined by the chemical reaction as described by the Butler-Volmer relation,

$$i_d = S_c i_0^{ref}\left(\frac{c_{O_2}}{c_{O_2}^{ref}}\right)^{\gamma_c} e^{\frac{\alpha_c F}{RT}(v_s - v_l - v_{ref})}, \tag{50}$$

where *Sc* is the surface area of the catalyst in m^2/m^3, and v_{ref} is a reference potential for the cathode, usually 1.2 V the theoretical maximum voltage. Within the catalyst layer $Q_j = i_d$. Boundary conditions for the electrical (V) and protonic (V_p) potential at each of the boundaries in the model are shown in Figure 27.

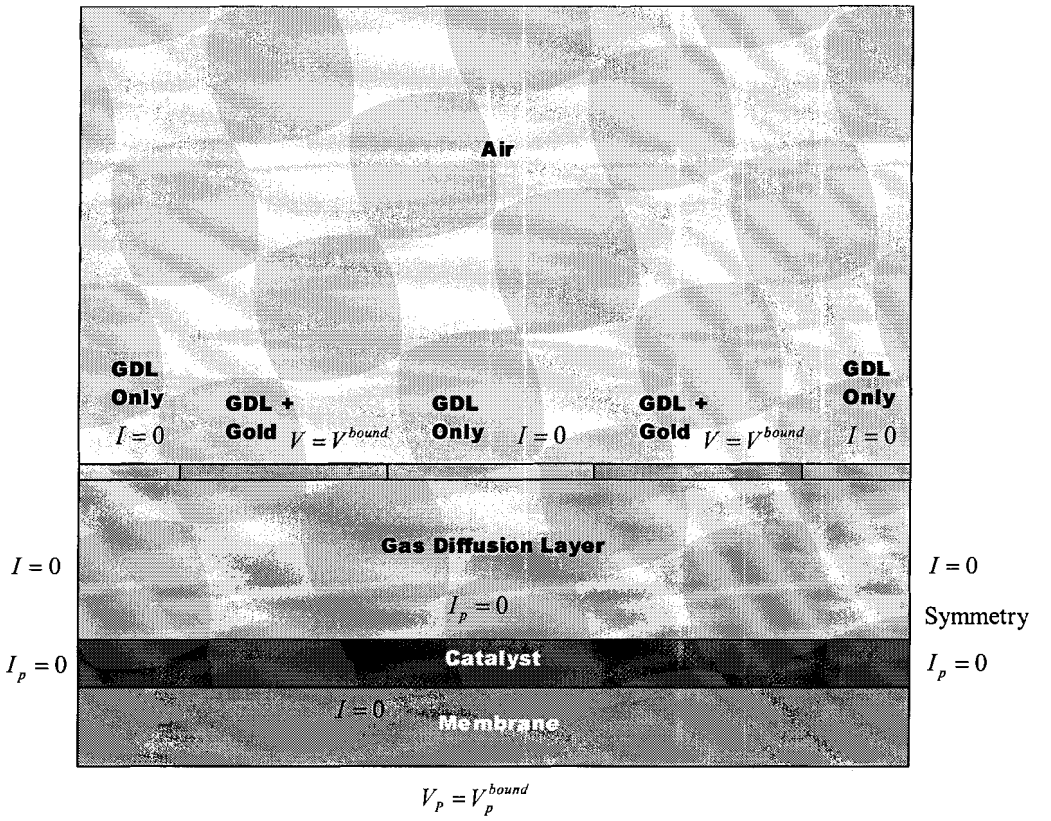

Figure 27:Boundary conditions for ionic and electronic transport

The GDL-thin film and catalyst-membrane boundary; are held at a constant potential, simulating a fixed load. Variations in load are modeled by variations in the solid boundary value.

Diffusion is modeled using Fick's Law

$$\nabla \bullet \left(- D_{eff} \nabla C_i \right) = R_i . \qquad (51)$$

The motion of reactants through the boundaries of the element is equal to the source term. The source term is given by using the current density (50) and Faraday's constant

$$R_i = \frac{i_d}{nF}, \qquad (52)$$

where n is the stoichiometric constant for a reactant i. Although Maxwell-Stephan diffusion is more accurate for diffusion of mixtures, Fickian diffusion is sufficiently accurate for air because nitrogen acts as a solvent and comprises approximately 70% of the volume at room temperature. Fickian diffusion also simplifies the scope of the problem, reducing the number of degrees of freedom, making the numerical solutions more stable and easier to achieve.

Heat transfer is assumed to be entirely conductive. Some heat and mass transfer occurs through buoyancy driven mass transport, this factor is neglected to simplify the model. Heat transfer is governed by

$$-\nabla \bullet (k\nabla T) = Q. \tag{53}$$

The thermal energy produced by the reaction is given by the following equation from [72]:

$$\dot{Q} = \left|\frac{i}{nF}\right|(T\Delta S) - |i\Delta V|. \tag{54}$$

Because the cathode is assumed to be a passive air-breathing cathode, there is no convective transport. Furthermore, the boundary conditions are determined by the ambient environment. Boundary conditions corresponding to the mass transport of species are shown in Figure 28.

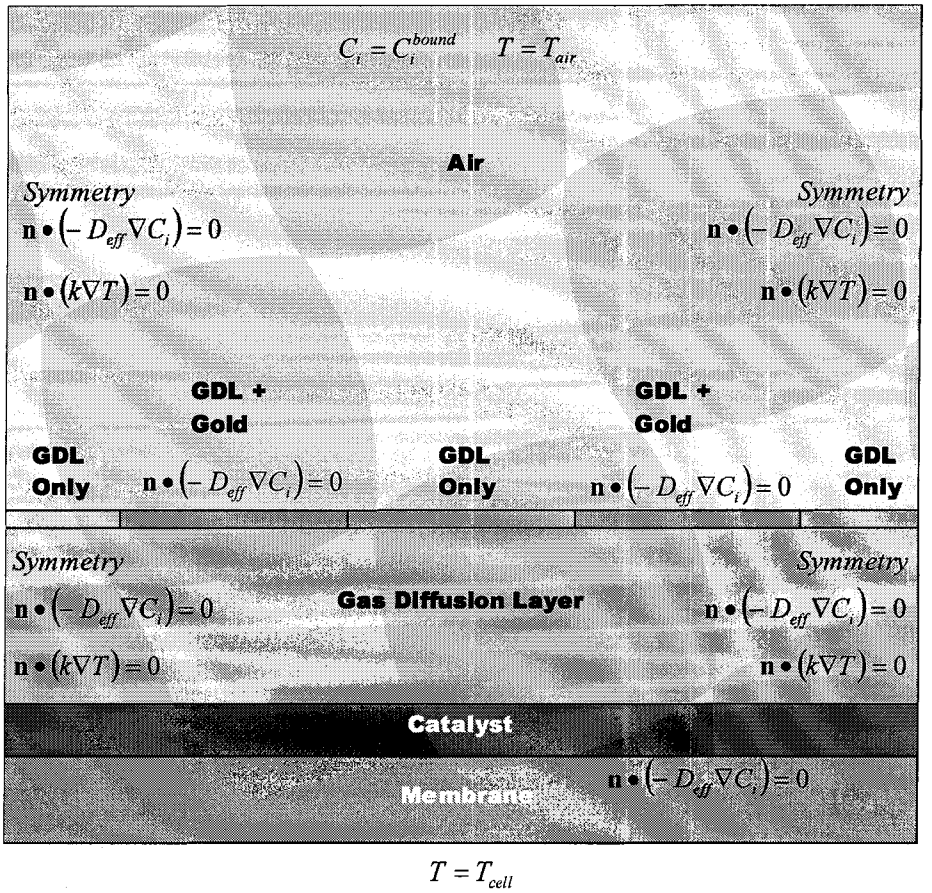

Figure 28:Boundary conditions for diffusion of reactants and products

Most of the boundaries within the electrode are zero flux (insulation or symmetry) conditions. Although our experimental data shows that some porosity remains after depositing thin films on the gas diffusion layer or the catalyst layer, we assumed that the porosity of the thin film covered area is zero; therefore, the boundary condition is insulation.

The phenomenon of electrode flooding is a common problem in all fuel cells and in passive fuel cells in particular. Our model handles flooding by using a pseudo-step function, similar in form to a Butterworth filter, modeling the change in porosity when the saturation limit is reached and liquid water forms in the pores. It is possible for fluids to exist in supersaturated states, however, droplet formation is catalyzed by suitable cavities on a solid surface. When the shape of the cavity matches the tangents of the spherical bubble formed within the cavity,

the energy required to form the free surface goes to zero and droplets or bubbles can be assumed to form instantaneously. In the high surface area catalyst layer, almost all possible pores sizes and angles are present. We assume that droplets will form at the onset of saturation.

Once a droplet of water has formed, the gas phase can no longer reach the catalytic sites. A partial blockage can occur if a finite element cell is only partially full of liquid water. To model this effect, we allowed the effective diffusion coefficient to approach zero once saturation has been reached. To simulate this, the effective diffusion coefficient tends towards zero prior to the average water concentration in the cell to reach the saturation point. We used the following equations to represent the change in effective diffusivity during flooding.

$$k = \begin{cases} 1 & C_{H_2O} <= C_T \\ \dfrac{1+\cos\left(\dfrac{\pi\left(C_{H_2O}-C_T\right)}{C_{SAT}-C_T}\right)}{2} & C_{H_2O} > C_T \\ 0 & C_{H_2O} > C_{SAT} \end{cases}, \qquad (55)$$

$$D_{eff}^{'} = kD_{eff}, \qquad (56)$$

where C_T is the empirically defined threshold and C_{SAT} is the saturation concentration of water at the current temperature. This function is shown in Figure 29.

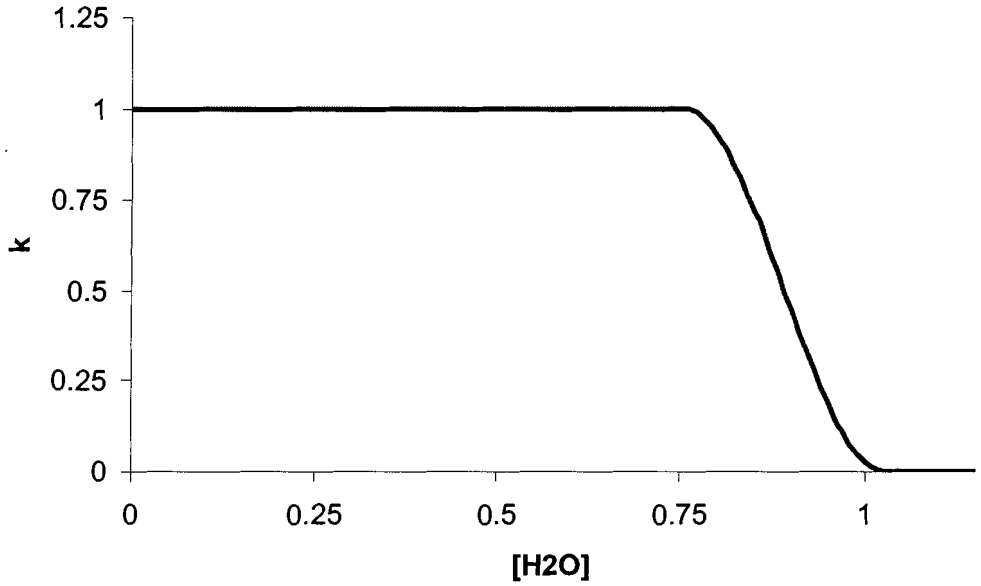

Figure 29:Representation of the scaling function for saturation effects

This function has several advantages over a standard step function despite its complexity. First, the effect of gradual losses in effective diffusion can be modeled. Second, the function is smooth and continuous aiding numerical computation and convergence. Third, the sloped portion of the curve is trigonometric and infinitely differentiable, which reduces the computational complexity. The threshold concentration is arbitrary and should be determined empirically. A threshold of $0.8\ C_{SAT}$, appeared to mimic the behavior of a fuel cell electrode but this ratio is not based on any underlying physical model.

This model assumes several fluidic behaviors within the catalyst layer. First, we assume that saturation occurs on a cell-by-cell basis. The transient effects of condensation are not modeled. The further accumulation of water on an existing surface is not considered, although it is a relevant transient effect. In the steady state, the precise boundary of the water gas interface is not modeled as precisely under this assumption. Modeling the precise location of

the water gas interface is not the intent of this analysis. Once substantial flooding occurs, the fuel cell is considered inoperable and the precise nature of the inoperability is not relevant.

Our second assumption is that liquid water motion is irrelevant in passive air breathing cathodes. On the surface this assumption seems spurious: liquid water will move from hydrophobic to hydrophilic regions and from micro to macro pores. However, in a passive air-breathing cell, liquid water is essential trapped. Liquid water can migrate within the electrode but cannot be drawn out of the electrode by forced air. If liquid water is forming in a steady state, it will saturate the electrode, and a passive fuel cell will flood.

Third, we assume that some saturation effects will occur before the cell is totally saturated. We assume that the volume of liquid water in the nano-pores will increase as the concentration of water reaches the saturation point, reducing the effective diffusion coefficient. This assumption has some theoretical and experimental viability, but is certainly not an accurate model of the actual processes. The process of droplet formation and flooding within the catalyst and gas diffusion layers is complex and nonlinear. Fields of mathematics such as percolation theory have attempted to explain the interaction between the formation of water, change in pore size, and the degradation of effective diffusivity; however, these approaches have yet to yield a satisfactory analytical solution.

The assumptions made in the model to reduce scope and allow the solvers to converge on a solution compromise the validity of the simulation and any conclusions that may be drawn from it. However, the simulations are not intended for precise physical representations of the electrode microstructure; rather, the FEA analysis is intended to provide approximate solutions which can be used to understand the design tradeoffs inherent in passive cathode designs that leading to new materials and electrode geometries. The precision of the

simulation is not as important as its repeatability in this type of analysis. If the models are good approximations and are consistent over the range of parameters investigated, simulations can be used to determine the relative impact of different designs and material properties.

Our FEA analysis considers three key design considerations for the micro-electrode: the impact of cross-sectional current collection; the effect of catalyst and GDL porosity on gas transport and flooding; and the effect of ambient operating conditions on gas transport and flooding. During the FEA analysis several parameters are altered while others are held constant, as in an empirical analysis. In the following simulation runs the parameters shown in Table 7 are used unless otherwise noted.

Table 7:Parameters used in simulations and their numerical values

Parameter Description	Symbol	Value
Electrolyte proton conductivity	σ_l	1 S/m
Catalyst electrical conductivity	σ_c	10 S/m
GDL electrical conductivity	σ_{GDL}	50kS/m
Catalyst and thin film electrical conductivity	σ_{TFCat}	20kS/m
GDL and thin film electrical conductivity	σ_{TFGold}	500kS/m
Electrical potential at the boundary	V_s	1.2V-0.5V
Protonic potential at the boundary	V_l	-0.4V
Effective diffusion coefficient of the catalyst	D_{eff}^{cat}	$8.3x10^{-7}m^2/s$
Effective diffusion coefficient of the GDL	D_{eff}^{GDL}	$2.5x10^{-6}m^2/s$
Concentration of oxygen at the boundary	O_2^b	$8.7mol/m^3$
Concentration of water at the boundary	H_2O^b	$0.45mol/m^3$
Ambient temperature	T	298K
Stoichiometric ratios for O_2 and H_2O	N_{H2O}, N_{O2}	2,4
Reference O_2 concentration for Butler-Volmer	O_2^{ref}	$3.66mol/m^3$
Exchange current density	i_0	$0.001A/m^3$
Effective catalyst surface area	S_c	$1x10^9m^2/m^3$
Reaction order	α	0.5
Faraday's Constant	F	96485
Thermal conductivity of the air	k_{air}	0.025 W/mK
Thermal conductivity of the catalyst	k_{cat}	100 W/mK
Thermal conductivity of Nafion	k_{Naf}	0.21 W/mK
Thermal Conductivity of the GDL	k_{GDL}	100 W/mK

Physical parameters related were determined experimentally as outlined in chapter 3. Electrochemical and thermal parameters were obtained from [72,73].

2.5.2 Simulation Implementation

We used FEMLab 3.0 from COMSOL to perform the FEA analysis. FEMLab is an extension of MATLab, a general linear systems analysis and programming environment. Because FEMLab uses MATLab as its mathematical underpinning, it is relatively straightforward to customize the governing equations for the model. However, memory management is less robust than dedicated commercial grade systems; therefore, large models cannot be effectively simulated. An example mesh is shown in Figure 30.

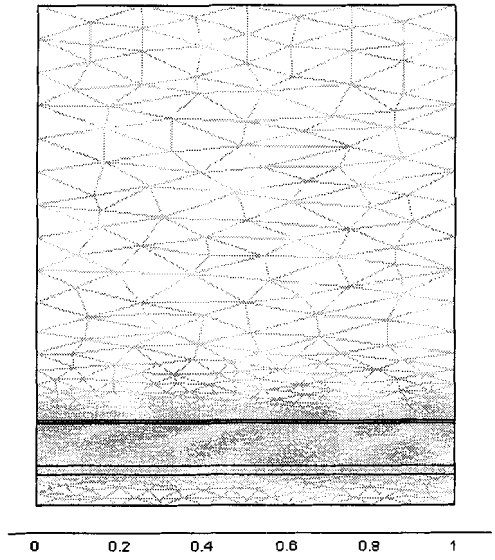

Figure 30: Example mesh of fuel cell electrode

Meshes were generated using FEMLab's unstructured mesh tool. The mesh size in the GDL, electrode and catalyst layers were halved, doubling the number of cells and increasing the resolution to remove numerical effects in the solution. Further increases in cell count had no effect on the solution.

Solutions were generated parametrically, starting at 1.2V decreasing in 0.05 V steps down to 0.7 V. Below 0.7 V steps of 0.005V were taken between solutions. To generate current output for a given input voltage, the total current in the catalyst layer was integrated, and divided by the total area. The UMFPACK nonlinear solver was used with a $1x10^{-6}$ convergence criterion. Automatic step size adjustment for the parametric solver was employed, refining the step size until a minimum step threshold was reached or the convergence criteria was satisfied.

2.5.3 Current Collection Effects

The earlier analysis on the effects of edge collection examined the impact of the lateral geometry on the performance of the fuel cell. That analysis assumed that the cross-sectional geometry was constant and had no effect on the Ohmic losses in the fuel cell system. However, the cross-section geometry must be considered, as it impacts the trade-off between mass transport and current collection. In particular the impact of the width of the thin film layer and its impact on current collection versus mass transport is a critical variable.

Several possible variants on the basic edge collection system are possible. Configurations of adjacent or bipolar bulk current collectors are feasible. Gas diffusion layers can be introduced to provide intermediate current collection and gas distribution. In thin film edge collected current collection, the width of the thin film current collector increases the lateral conductivity of the electrode, but inhibit the diffusion of reactants and products into and out of the electrode. By crossing these design parameters, we can design a simulation based experiment to analyze the impact of the design parameters. Figure 31 shows the possible configurations for current collection in thin film fuel cells.

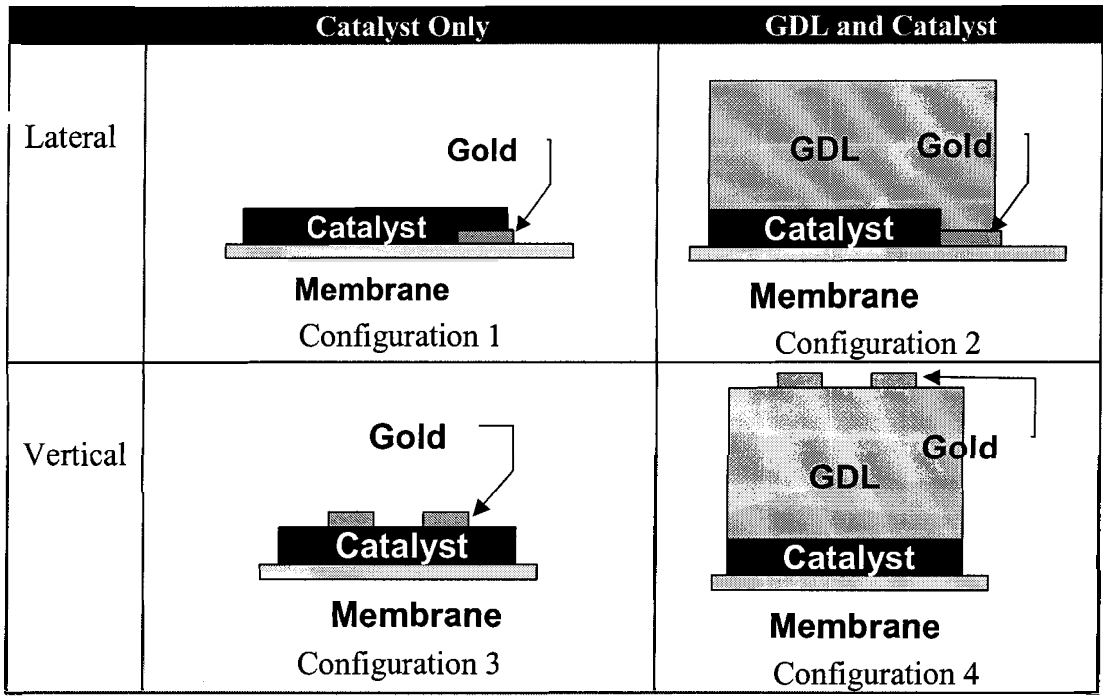

Figure 31: Thin-film electrode configurations considered

Lateral current collection offers no impedance to the diffusion of reactants in and out of the electrode; however it requires more surface area. Vertical current collection reduces the distance that electrons must travel prior to reaching the high conductivity electrode, but it interferes with gas flow. Given the requirements for energy density, the vertical current collection method is preferred, if the thin film current collectors do not substantially interfere with the passive mass transport at the cathode.

We assumed that the gold was impermeable, and therefore, no gasses could diffuse through the gold in the vertical current collection cases. In the lateral current collection cases, the width of the overlap between the gold and catalyst or GDL were varied to determine the

impact of current constriction at the interface. In both the vertical and lateral cases we refer to the gold-width parameter. The gold-width parameters used in the simulations described in sections 2.5.3.1 to 2.5.3.4 are shown in Table 8.

Table 8: Gold-width parameter used in simulations

Width	Vertical (trace width) (μm)	Lateral (overlap) (μm)
Small	100	0
Medium	200	50
Large	300	250

Sections 2.5.3.1 to 2.5.3.4 examine the performance of each of these configurations using the FEA model described in the preceding section. The operating parameters are held constant throughout the model. The membrane boundary temperature is set to 35 C. The air temperature boundary is set to 25 C and the relative humidity to 45%, typical for an air-conditioned building. Potentials are set at the membrane and thin film boundaries for the liquid and solid phase potentials, respectively.

2.5.3.1 Lateral Collection without GDL

The simplest configuration for a micro fuel cell electrode is a laterally connected catalyst-only topology. This configuration is the simplest to manufacture, because no GDL component is required. The quality of the thin film current collector can be higher because the membrane has a lower surface roughness than the GDL or catalyst surface. Even though the quality of the current collection can be improved, the surface area required to achieve the same current density is lower because the adjacent current collectors consume surface area.

The gold width parameter, described in Figure 31, refers to the degree of overlap with the current collector: wide corresponds to the catalyst layer completely covering the current collector, medium refers to a 100 μm overlap, and small refers to no overlap. Figure 31 shows

the three conditions for lateral current collection at an electrochemical bias of 0.97 V. The current path is shown as streamlines. The electrical scale is provided as a reference. The grayscale bar contains the magnitude of the electrical losses, in Volts. The contour lines represent the proton phase potential loss, in Volts, the concentration grayscale is in mol/m^3.

In all three cases, the electrical current flows left to right. The rate of voltage drop increases the closer to the electrode, in a reduced version of the edge-collected case described above. Even though the length an order of magnitude shorter than discussed in section 2.4 the electrical conductivity of the bare catalyst is 1000 times smaller than the GDL conductivity. Predictably, the performance of side-collected, catalyst-only configuration was poor given the current geometry. Substantial Ohmic losses (greater than 0.4 V) were incurred traveling through the catalyst layer to the bulk current collector on the edge. Any savings from the improved film quality would be lost in the lateral routing of current through the catalyst layer. The configuration used a 500 μm electrode width. Because Ohmic losses were linear, the performance could be increased by using very thin strips of catalyst, less than 100 μm across. However, the ratio of catalyst to bulk current collector width must be made as large as possible to maximize power density. Demonstration of fuel cells based on this architecture is possible, but due to the Ohmic losses in catalyst layer, any architecture with a superior local conductivity would have superior performance. It would be possible to demonstrate a fuel cell based on this architecture, but it would have limited commercial appeal because of its Ohmic limitations.

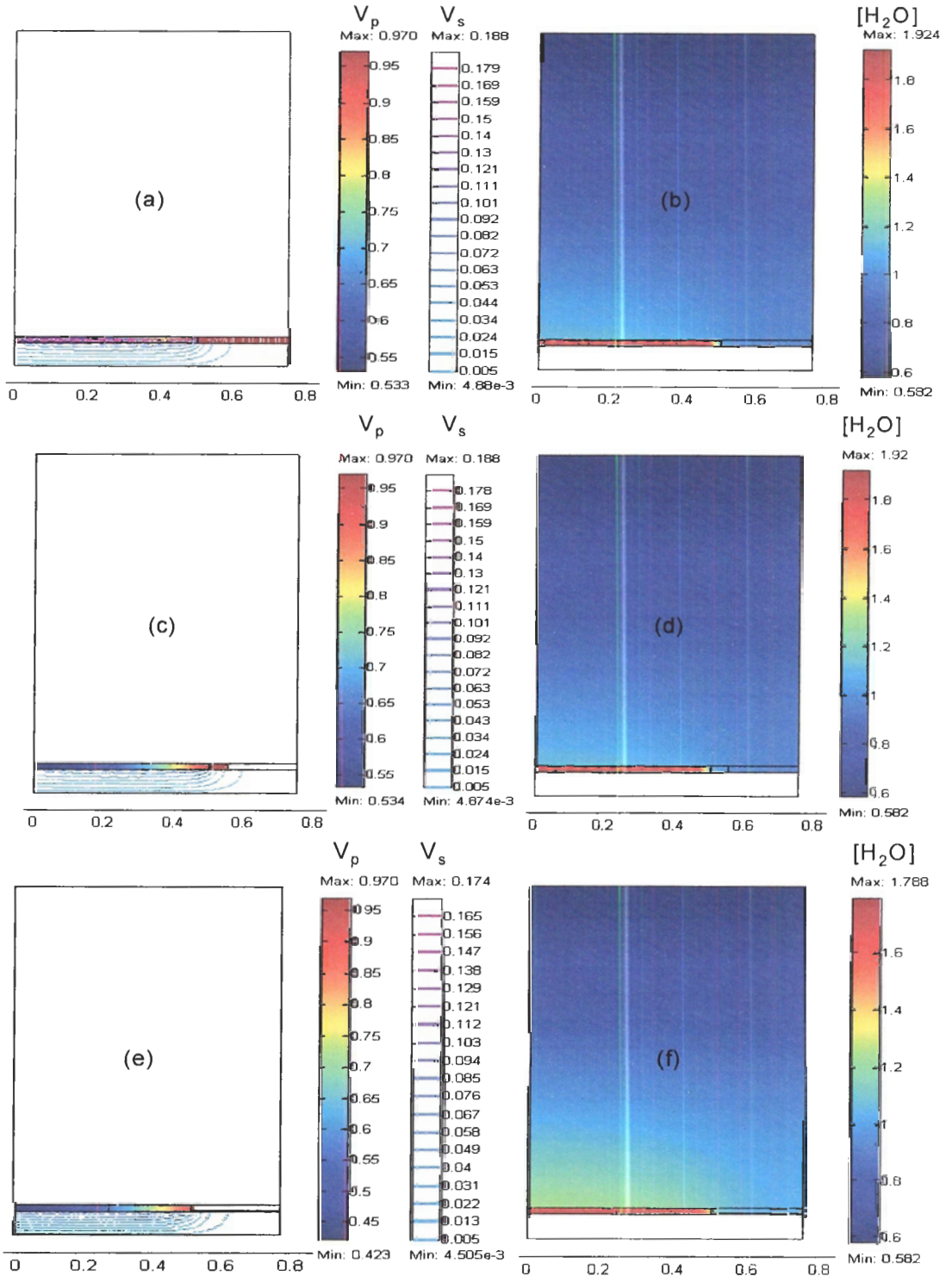

Figure 32:Simulation results for configuration 1; (a) potential drop narrow, (b) water vapor concentration narrow (c) potential drop medium, (d) water vapor concentration medium (e) potential drop wide, (f) water vapor concentration wide

2.5.3.2 Vertical Collection without GDL

The simplest edge collected fuel cell architecture is a catalyst layer and a current collector. As shown in Figure 20, this architecture is on the boundary of practical utility due to Ohmic losses along the length of the electrode. The impact of geometry on the width of the cell is more difficult to model and is best understood using FEA analysis. We used the conductivities according to Figure 21. The physical and electrical parameters were as shown in Table 7. The performance of a thin film electrode directly deposited on a catalyst layer is shown in Figure 32. In this case, the gold width parameter refers to the width of the current collector on the surface of the catalyst. Figure 33 shows the three conditions for lateral current collection at an electrochemical bias of 0.97 V. The current path is shown as streamlines.

Moving the current collectors to the vertical current collector configuration has nearly eliminated the electrical potential drop through the catalyst layer. However, examining the grayscale of the water concentration, it is clear that saturation regions form under gold regions, evidenced by the high concentration of water near the current collectors. The diffusion coefficient of the catalyst layer is almost an order of magnitude smaller than the GDL diffusion coefficient and almost two smaller than the diffusion in air.

Although the vertical collection significantly reduces the Ohmic losses in the solid phase, the low porosity of the catalyst layer causes significant flooding in areas beneath the thin films. Additionally, the high surface roughness of the catalyst layer reduces the conductivity of the electrode, increasing the Ohmic losses along the electrode. While this geometry performs better locally than the lateral edge collection, neither are a practical solution for an edge collected fuel cell. Locally, the medium and wide electrodes promote significant flooding. The narrow system behaves no worse than the lateral current collection system.

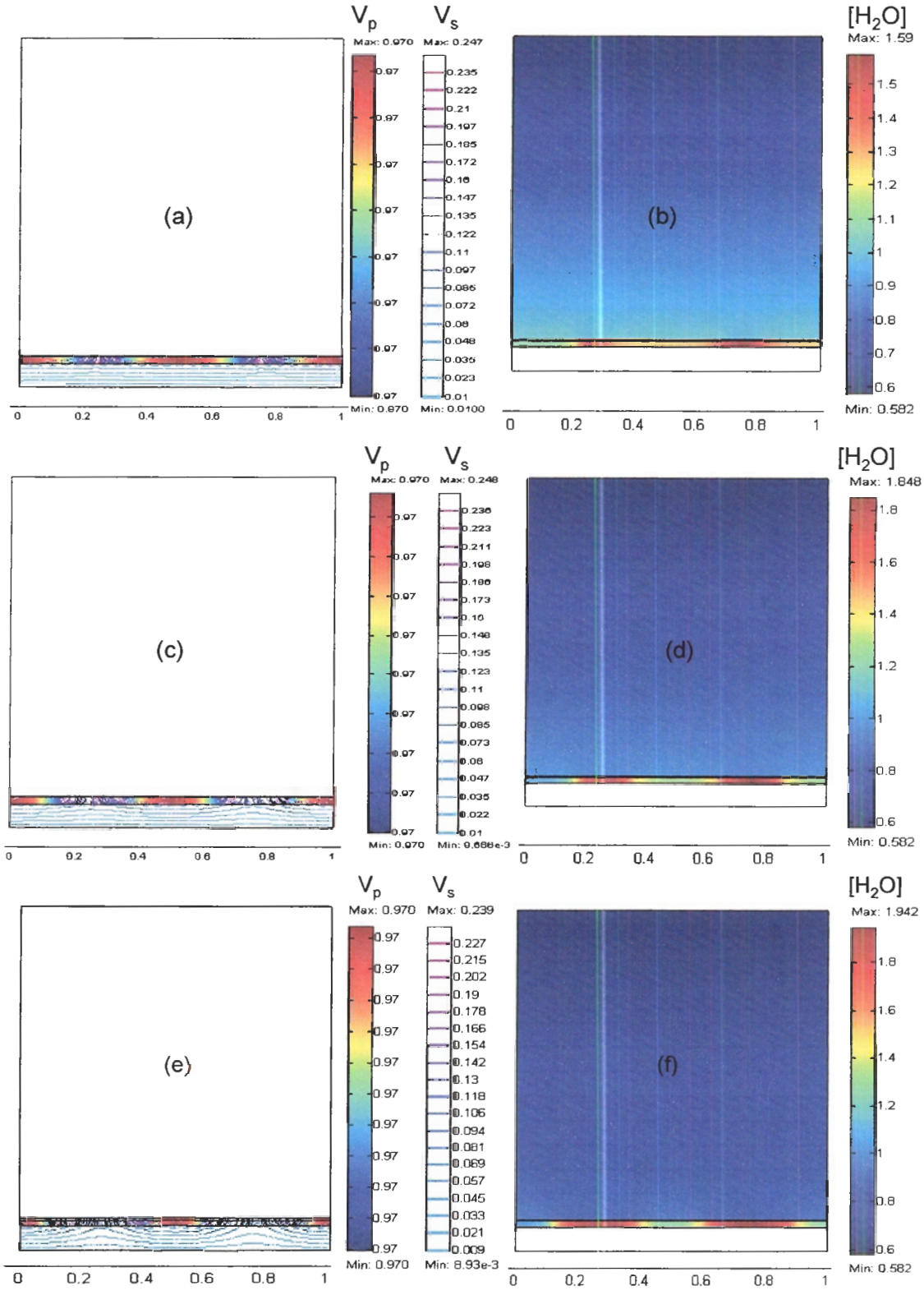

Figure 33:Simulation results for configuration 3; (a) potential drop narrow, (b) water vapor concentration narrow (c) potential drop medium, (d) water vapor concentration medium (e) potential drop wide, (f) water vapor concentration wide

2.5.3.3 Lateral Collection with GDL

A gas diffusion layer imposes additional impedance on the mass transport of the reactants and products. For systems based on vertical or bipolar collection, the GDL provides a higher diffusivity path around the obstacle provided by the rib or thin film. In the case of lateral current collection, there are no obstacles to diffusion. For a GDL to have an impact, it must be substantially more electrically conductive than the catalyst layer, without substantially impeding the flow of reactants. Figure 33 shows the three conditions for lateral current collection at an electrochemical bias of 0.97 V. The current path is shown as grayscale streamlines.

The GDL-based lateral collection configuration has potential drops of less than 60 mV in all configurations, clearly superior to the lateral catalyst only given the difference in thickness and conductivity between the GDL and catalyst layer. The GDL lateral collection system did no show any evidence of additional flooding when compared to the catalyst case despite the additional diffusion resistance.

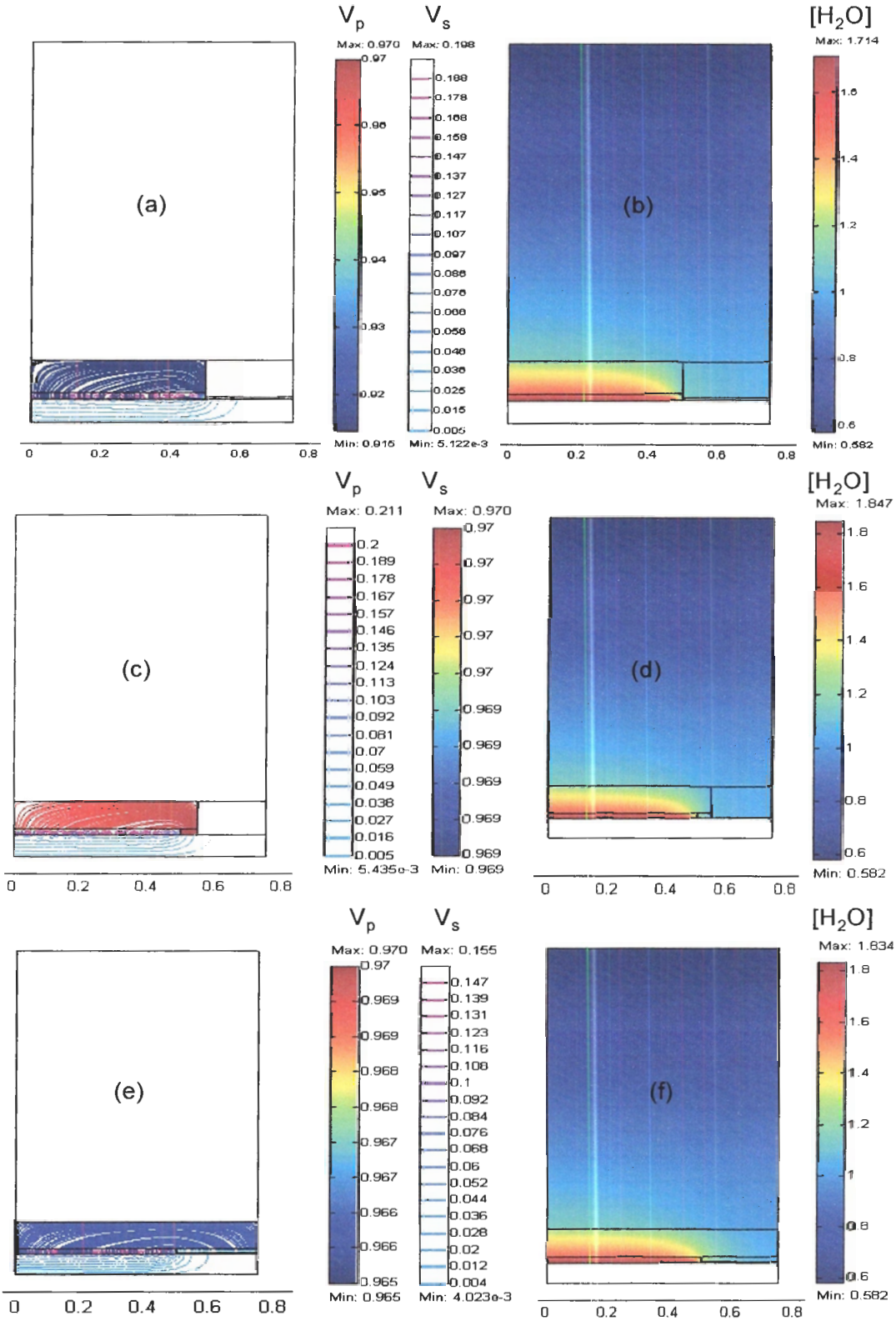

Figure 34:Simulation results for configuration 2; (a) potential drop narrow, (b) water vapor concentration narrow (c) potential drop medium, (d) water vapor concentration medium (e) potential drop wide, (f) water vapor concentration wide

The GDL-based lateral collection system performs significantly better than the catalyst only lateral collection system. Ohmic losses are significantly less because the GDL has a much higher conductivity than the catalyst layer. While the GDL poses an additional overhead for diffusion, the overall cell is still limited by the porosity of the catalyst layer. The additional conductivity of the GDL makes this architecture superior to the catalyst only architecture. However, the adjacent thin film still consumes surface area. The vertical current collection system would be superior if the thin films do not interfere with the mass transport to the same degree as in the catalyst only vertical current collection case. Little difference exists between the small and large overlap architectures. Because the components of the GDL are less expensive than platinum, little benefit can be derived in pursuing the smaller overlapped architecture. A variant of this architecture has thin films on both the top and bottom of the GDL, which enhanced conductivity along the electrode, but has little impact in cross-section.

2.5.3.4 Vertical Collection with GDL

Introducing a highly conductive gas diffusion layer had a significant impact on the Ohmic losses along the length of the fuel cell. A similar impact can be observed in the cross-section. This effect is not unexpected because adding a more conductive path for the electrons would obviously alter the potential drop. However, the magnitude of the impact and the relation between the position and size of the gold traces must be considered. The following figure compares the impact of potential drop for two different widths of thin film as well as mass transport for the three electrode widths.

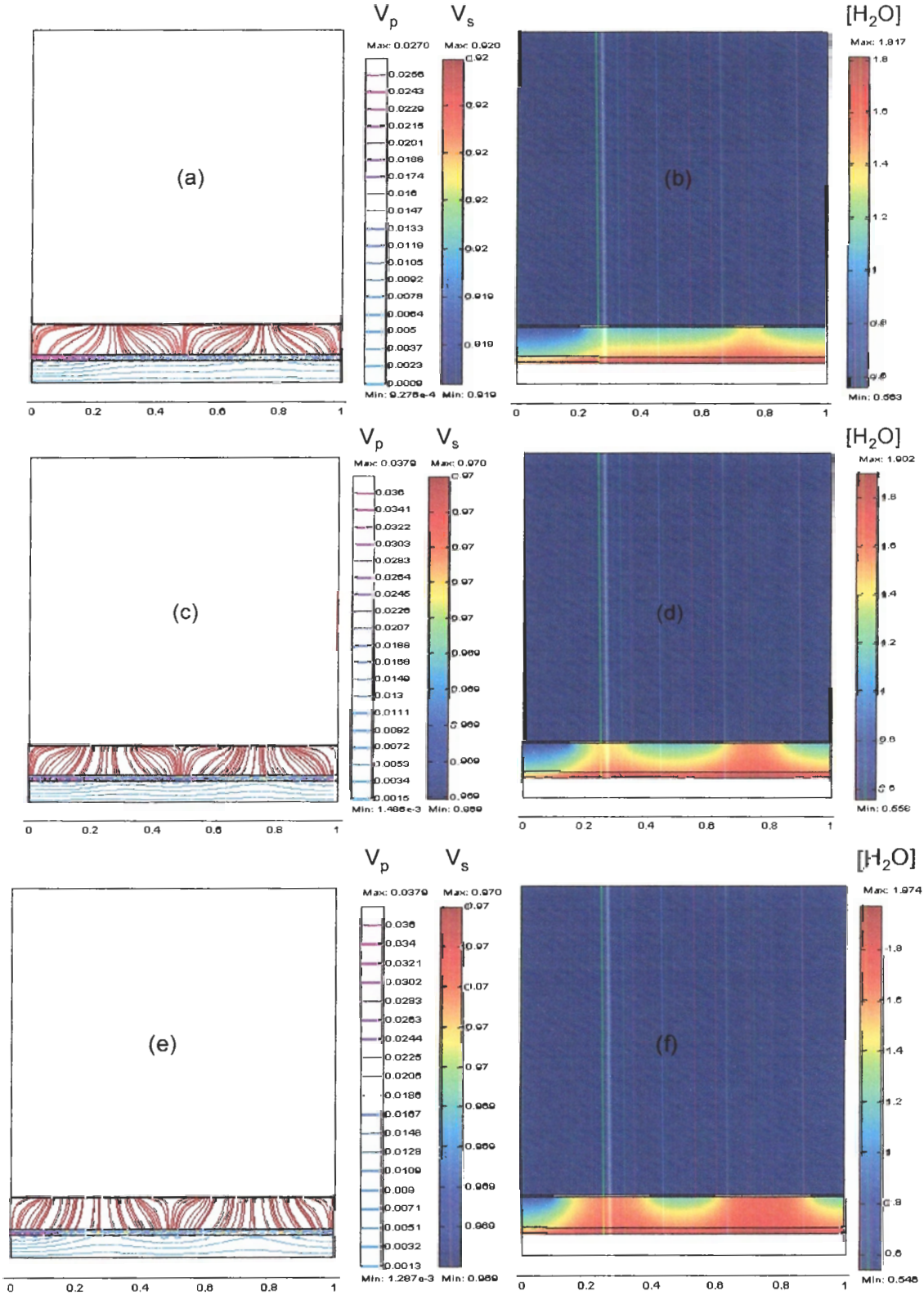

Figure 35:Simulation results for configuration 1; (a) potential drop narrow, (b) water vapor concentration narrow (c) potential drop medium, (d) water vapor concentration medium (e) potential drop wide, (f) water vapor concentration wide

Electrical potential loss is only 1 mV in all three cases examined. The potential loss is more than acceptable. Diffusion limitations are evident under the current collectors in the wide configuration. This configuration seems to provide a balance between current collection and mass transport if the gold electrode width is properly designed.

In all cases, most of the potential drop occurs in the catalyst layer. In the case of the wide conductor, the potential drop is regular. In the case of the narrow conductor, the potential drop is less regular. Although some of this irregularity is an artifact of the numerical solution, it indicates concentration of current at the thin film. This effect is analogous in many ways to the concentration of current at the ribs of a larger PEM cell. While the resistances in a larger PEM cell are substantially lower, the current densities are generally an order of magnitude higher, leading to similar effects. The more perpendicular the electronic connector is to the catalyst layer, the more regular the potential drop and the smaller the losses.

The electrochemical reaction is effected by the potential drops of the electronic and ionic phases, and the concentration of reactants, which is determined by mass transport. This analysis has shown that the Ohmic losses in thin film electrodes are at the bounds of acceptability, even with a highly conductive gas diffusion layer. To create the most efficient fuel cell, the width of the thin film collectors should be maximized while minimizing the impact on the mass transport in the electrodes. This conclusion applies to both uncompressed cells where thin films are directly deposited on the gas diffusion layer, and compressed fuel cells where a thin film is deposited on an insulating substrate and pressed into contact with a gas diffusion or catalyst layer.

2.5.4 Effective Diffusion Coefficient

Depending on the fabrication technique used to create the fuel cell, a GDL can have a practical effective diffusion coefficient between $2.5x10^{-5}m^2/s$, (the diffusion rate of water in air) to $8.3x10^{-7}m^2/s$, the diffusion rate of the catalyst layer. Obviously larger diffusion constants are more desirable to maximize water transport; however, for particle based gas diffusion layers, smaller porosity generally results in a higher conducting phase content and lower Ohmic resistance.

The impact of the diffusion coefficient will be primarily observed in the mass transport limited portion of the polarization curve. Predictably, the lower the diffusion coefficient, the earlier the mass transport limitation will be reached. For micro fuel cell design, lower current densities are expected for the following reasons: the sluggish kinetics of direct methanol operation; the reduced current densities required for edge collection; and the high-voltage, low current requirements of small electronic devices. Mass transport limitations are acceptable if they occur sufficiently far from the expected operating point. Figure 36 shows the impact of effective diffusion coefficient on a vertical GDL fuel cell configuration with no thermal gradient between the cell and ambient air.

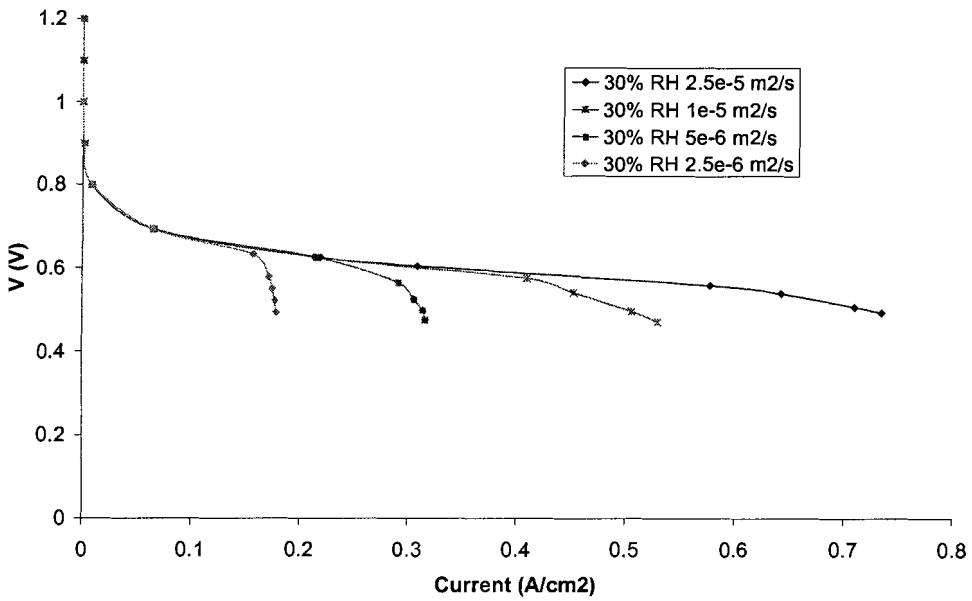

Figure 36: Impact of effective diffusion coefficient

In Figure 36, the impact of diffusion on fuel cell performance is shown. Each point on the polarization curve represents one simulation run in the parametric solver. All curves assume a boundary 30% relative humidity and room temperature, which is generally the minimum for normal environmental conditions (see Table 10) and a wide cross-section. Simulations continued until saturation was reached. Flooding, unlike oxygen starvation due to mass transport limits, causes fuel cell failure rather than predictable performance degradation. Once significantly flooded, the fuel cell ceases to function because only isolated pockets can produce current, causing a truncated polarization curve.

As expected, a decreased diffusion coefficient leads to early flooding and mass transport limitations. For all diffusion coefficients at 30% humidity, the limiting current is well beyond the required 50 mA/cm^2 outlined in the target application in chapter 1. At 100 mA/cm^2 all curves are still within the Ohmic region. For larger cells, 100 mA/cm^2 operation is insufficient. For micro DMFC cells, 100 mA/cm^2 is a standard operating point. However,

only deserts are routinely 30% humidity, so the curves in Figure 36 represent a best case for expected environmental operating conditions. Room temperature is low for the operating temperature of a micro fuel cell. Other parameters such as increased relative humidity and cell operating temperature must be considered. Figure 36 shows the impact of diffusion on fuel cell performance with a cell operating temperature of 55 C.

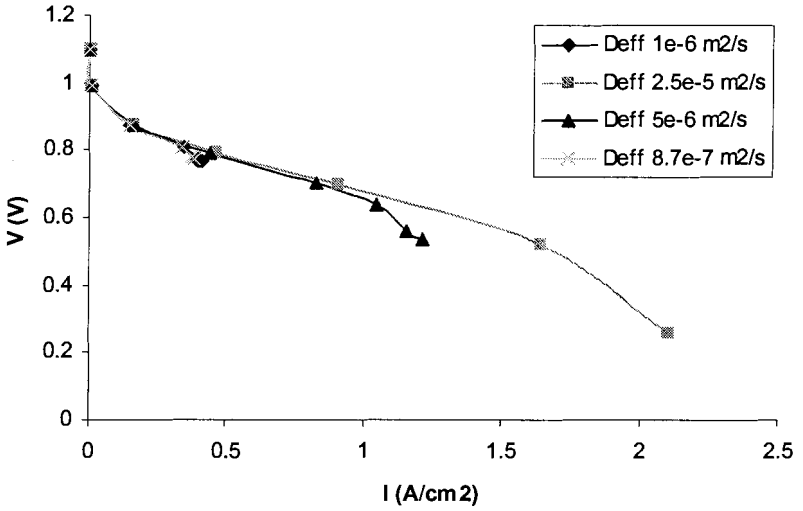

Figure 37:Impact of effective diffusion coefficient with heated anode

In Figure 37, the impact of diffusion on fuel cell performance is shown. Simulations continued until saturation was reached. Each point on the polarization curve represents one simulation run in the parametric solver. All curves assume a boundary 45% relative humidity and room temperature, and a cell operating point of 55 C. The higher operating temperature within the cell increases the ability of air at the cathode to hold water. Even though the air is cooler, the higher diffusion coefficient in air allows the water vapor to dissipate before flooding. Once significantly flooded, the fuel cell ceases to function because only isolated pockets can produce current, causing a truncated polarization curve. The diffusion coefficient clearly has a significant impact on the performance of the fuel cell. Diffusion coefficients of

greater than $5x10^{-6}$ m^2/s consistently exceed the current density requirements for micro fuel cell operation.

2.5.5 Temperature Effects

A thermal gradient can ease the flooding problem by locally increasing the water capacity of the surrounding air. Table 9 shows the current density at which flooding occurs for the given geometry with a GDL effective diffusion coefficient of $5x10^{-6}$ m^2/s and a relative humidity of 45%.

Table 9: Effect of temperature

Cell Temperature (C)	Ambient Temperature (C)	Current at flooding (A/cm^2)
55	25	1.25
35	25	0.417
25	25	0.199
55	15	1.37
35	15	0.511
25	15	0.275
55	5	1.4
35	5	0.57
25	5	0.335

Even with no thermal gradient, the performance of the fuel cell is sufficient at moderate relative humidity. The lowest current density at saturation is still sufficient to support most micro fuel cell operation. We did assume that the fuel cell would operate internally at a minimum of 25 C. Because of the kinetics, most fuel cell reactions are sluggish at lower temperatures we believe this is a reasonable assumption.

The results seem somewhat counterintuitive at first: the fuel cell seems to perform better at low ambient temperatures. This performance boost is due to the reduced water content at lower temperatures for the same relative humidity. Because the cell has a much higher

thermal conductivity than the air, the fuel cell maintains its internal temperature, and the lower ambient temperature reduces the water content at the boundary. However, the heat required to maintain the operating temperature also increases with temperature difference, decreasing the net energy efficiency of the system.

Table 9 indicates that as long as a temperature gradient is maintained, the passive cathode will continue to operate. Because the air has a much higher effective diffusion coefficient than either the catalyst or GDL layers. If the cell is warm enough to increase the saturation point within the GDL, the water can escape and disperse in the surrounding air. While this is true in the operating region examined, it is not generalizable. At very high temperatures, water will begin wicking from the membrane, reducing the membrane conductivity, and rendering the fuel cell inoperable. At very low temperatures, water escaping from the fuel cell will condense or even freeze before it has time to disperse, coating the exterior of the cathode in water or ice. Neither of these effects have been modeled or investigated in the current system.

Our simulations indicate that a minimum of a 10 C temperature differential can ensure that the fuel cell operates well with a passive cathode. However, this analysis neglects the thermal engineering required to meet this target. Our analysis also indicates that micro fuel cells will have a tendency to flood when they are at equilibrium with the surroundings. This situation is particularly common at startup.

2.5.6 Environmental Impacts

Portable electronics are portable. They must be able to operate under a variety of operating conditions. Although temperature has some effect on reaction kinetics, relative humidity has a significant impact on fuel cell operation by changing the driving concentration for the diffusion of water out of the fuel cell. Increasing the boundary concentration not only

increases the set point for water removal from the cell, but it also reduces the rate at which water vapor is removed by reducing the concentration difference in Fick's Law. Table 10 shows the monthly average humidity for major centers around North America [74-75].

Table 10:Average humidity values for major centers in North America

City	J	F	M	A	M	J	J	A	S	O	N	D
New York	54.0	65.5	64.0	63.0	64.0	67.0	67.5	68.5	70.0	68.5	65.5	65.0
El Paso	51.5	45.5	37.0	30.0	29.5	31.0	39.5	47.5	50.0	48.5	45.5	48.5
Key West	66.0	75.0	73.0	71.5	70.0	71.5	72.5	72.0	74.0	75.5	76.0	76.0
Vancouver	83.8	66.2	78.1	75.1	73.9	73.3	74.3	76.3	78.9	81.9	83.5	83.6

It is apparent from the table that even at extremes of humidity, relative humidity (RH) rarely drops below 30% or rises above 90%. Passive fuel cells must operate reliably over the entire range. The temperature plays a significant role in the impact of relative humidity in fuel cells. The following table shows the impact of humidity and effective diffusion coefficient on the performance of a passive cathode.

Table 11: Effect of 90% RH

Cell Temperature (C)	Ambient Temperature (C)	Current at flooding (A/cm^2)
55	25	1.15
35	25	0.25
25	25	0.015
55	15	1.25
35	15	0.4
25	15	0.146
55	5	1.38
35	5	0.57
25	5	0.28

Increasing the relative humidity does impact the performance of the cell, particularly when the fuel cell is operating near the ambient temperature. With a sufficiently high diffusion coefficient and proper thermal management passive air breathing fuel cells are feasible. Passive fuel cells will be prone to flood at startup because they are at equilibrium with the

ambient environment. Some form of pre-heating at startup will be required to ensure that the fuel cell operates properly when starting.

2.6 Summary

Our theoretical analysis of the distinctive behaviors of micro fuel cells has lead us to conclude that while micro fuel cells are feasible, neither micro systems theory or the empirical design guidelines normally used to fabricate larger fuel cells is sufficient to guide the design of the fuel cell alone. Our combined analysis has led us to a set of guidelines that determines the design boundaries for micro fuel cells.

2.6.1 Flow Guidelines

Flow channel dimensions should be minimized to maximize energy density. Several tradeoffs exist between the size of the fuel cell and the size of channels. However, general guidelines can be derived for small fuel cells. For fuel cells whose length dimensions is below the critical threshold, the following hydraulic diameters can be used as a rule-of-thumb minimums: 200 μm for gas systems and 400 μm for liquid systems. These values could be reduced further if the fuel cell system were engineered to ensure that only single-phase flow was present. For flow in single-phase systems, the dimensions are dictated by the cumulative effects in the liquid case. Gas systems have a floor of approximately 20 μm.

2.6.2 Electrode Guidelines

We derived a simple algebraic approximation for the Ohmic losses due to edge collection. Based on these calculations we can conclude that edge-collected electrodes larger than 3 cm are feasible but not practical. Edge-collection is only practical in the smallest architectures. Further analysis of the relationship between conductivity and edge collection showed that

catalyst and current collector systems as described in many attempts in the literature (see chapter 1), are not ultimately realizable in practical systems. A gas diffusion layer reduces the losses to acceptable levels, if the conductivity of the GDL is sufficiently high. Electrodes of between 1 and 3 cm in length are possible for fuel cells with a combined GDL-thin film architecture if the GDL has a conductivity of greater than 10 kS/m.

2.6.3 Diffusion Guidelines

FEA analysis was used to examine the behavior of passive air-breathing cathodes, an area of fuel cell analysis not commonly undertaken. The results of the simulation showed that the behavior of air-breathing fuel cells is strongly dependent on the effective diffusion coefficient and the ambient humidity. High relative humidity causes the onset of flooding to occur at current densities commonly associated with the kinetic or Ohmic region of fuel cell behavior. The trade-off between porosity and conductivity in the gas diffusion layer is a complex, but for passive fuel cells, the fuel cell should be designed for maximum porosity at the minimum appropriate GDL conductivity.

2.6.4 Thermal Guidelines

To prevent flooding, a minimum 10 C temperature differential must be maintained with the ambient environment. A sufficiently high thermal gradient will allow the vapor produced by the fuel cell to dissipate in the surrounding air before reaching a critical vapor pressure. In addition, below freezing, the thermal debt increases, as the temperature gradient must be sharp enough to at least maintain the fuel cell above freezing. Finally these guidelines only apply to very small fuel cells. Larger cells running at higher power densities will have very different thermal behaviors. Fuel cell design for thermal management is not part of this dissertation; however, it is worth noting that the overall geometry and thermal properties of all the fuel cell

components are important for proper thermal management. All we could realistically conclude from this work on thermal management was it is possible to reduce the impact of flooding through thermal management of the cell during operation, and that passive cells are prone to flooding at startup if no preheating is provided.

2.7 Conclusions

As we stated earlier, specific conclusions should not be drawn from general simulation work. Too many degrees of freedom in fuel cell design and operation imply that computational solutions may not be generally valid. Only very specific problems or very general trends can be analyzed using these techniques. In this thesis we have been concerned with general design guidelines to shrink the possible design space for inside-out micro fuel cells. The optimization of these designs is left for future work. From these general guidelines we can draw the following general conclusions:

1. Flow channels should be at least 50 μm, but less than 400 μm, based on the impact of macro and micro fluidic phenomenon within this range.

2. A GDL is required for reasonable current collection. It should have an effective diffusion coefficient of at least 2.5×10^{-6} m^2/s, but preferably higher, based on our simulation results.

3. Edge collection can have a significant impact on Ohmic losses, as such, electrode length should be minimized, based on the approximation for constant current density edge collected potential drop we derived.

4. Lateral collection with GDL is the best geometry for minimizing losses, but at the expense of wasted surface area. A sufficiently conductive and porous GDL

permits the use of the higher energy density vertical current collection topology, based on our simulation of electrode structure and material properties.

5. Passive fuel cells tend to flood at startup unless preheated, based on our simulations including thermal effects.

6. A thermal gradient is required to work in high humidity areas, or current will be unacceptably low, based on our simulations including thermal effects.

Using these general guidelines and the architecture guidelines outlined in chapter 1, we have created a new fuel cell architecture and fabrication technique. The fuel cell is based on the GDL, vertical current collection topology, employs an inside-out architecture, and is fully fabricated as part of the manufacturing process. The cell design and fabrication process are described in chapter 3.

Chapter 3 Design and Fabrication

3.1 Introduction

In chapter 1 we described the current state of the art in fuel cell design and discussed some of the drawbacks in micro fuel cell architecture and fabrication. Current micro fuel cells suffer from insufficient power density; are too difficult or expensive to manufacture at small scales, or have insufficient lifetimes. In chapter 2 we motivated a minimum practical size and power density for a fuel cell based on physical principles and application requirements, and analyzed the electrode structure of micro fuel cells. Our conclusions in chapter 2 lead us to a specification of architectural, material, and operating conditions for a practical micro fuel cell.

In this chapter we present our micro fuel cell architecture solution. Based on the understanding and architectural specifications in chapter 2 and the design and fabrication shortcomings discussed in chapter 1, we have designed a fuel cell that could deliver a practical performance with easily automatable fabrication techniques and assembly. Because the cost drivers for micro fuel cells are fabrication, packing and system components instead of materials, the fabrication process must be automation friendly.

Although a general system architecture was derived in chapter 2, we had to develop appropriate techniques to fabricate the architecture and new materials to realize the fabrication process. In this chapter, we present the overall architecture and fabrication technique, followed by detailing each step of the process, and any novel materials are characterized. Characterization of new materials is presented to outline the effect they have on the fuel cell performance. While material work is not the primary focus of this thesis, the creation of novel materials was required to achieve the architecture and fabrication process. New materials were developed in conjunction with the Membrane Electrode Assembly Group at NRC-IFCI.

3.2 Fabrication

The fabrication of micro fuel cells has been a topic of investigation for more than 5 years. The creation of fuel cells with small volumes is crucial to achieving the total volume and power density required for the portable market. Most researchers have relied on MEMS processes to minimize the volume of the fuel cell. On the surface, MEMS techniques seem appropriate choice, because many chemical and medical microfluidic devices are fabricated this way. Using the electrode size and flow field diameter limits derived in the previous chapter, it is possible to design a minimally thin micro fuel cell, then create a MEMS based fabrication process to achieve the design.

MEMS techniques have two significant advantages: first, the ability to pattern devices on scales approaching one micron; and second, the ability to fabricate more devices into the same area, increasing device density. Our derivations show that the minimum realistic channel dimension is 50 μm. The surface area of the micro fuel cell is dictated by the required current output. The minimum realizable pattern dimension, as determined by the micro fabrication technique, has little bearing on the active surface area of the fuel cell. Because the surface area is limited by electrochemistry, not manufacturing techniques, micro fuel cells cannot benefit the ability to decrease device size. With fluidic dimensions on the order of 100 microns and surface area independent of pattern resolution, micro fuel cells are clearly not MEMS devices.

Micro fuel cell design and fabrication have related, but different, requirements to those commonly found in MEMS systems. An analysis of the unique characteristics of the demands of micro fuel cell design and fabrication, combined with the numerical and theoretical solutions from the previous chapter, can lead to architecture based on the requirements of the

system, not the particulars of a specific manufacturing process. Four key drivers of micro fuel cell design and fabrication exist: cell thickness, electrode structure and performance, fabrication cost and repeatability, and mechanical stability.

Micro fuel cells are dominated by volumetric power density. Because the surface area of a fuel cell is dictated by electrochemical efficiency and power requirements, the most efficient method to increase the volumetric power density is to decrease the fuel cell thickness. As stated in chapter 1, the thickness can be minimized by eliminating compression, and gaskets, as well as reducing the flow field volume to the minimum volume allowed by micro fluidics. Minimum dimensions for most fuel cell components were illustrated in chapter 2. Any further reductions in volume can occur by minimizing the GDL or membrane thickness. The minimum practical GDL thickness is a function of its porosity and conductivity as outlined in chapter 2. A thicker GDL has a higher conductance for better edge collection, but requires higher porosity to ensure that the diffusion of water out of the cathode occurs quickly enough. A smaller thickness increases the volumetric power density. Given the conductivity and porosity of a given GDL material, an optimal configuration can be derived for a desired operating range.

The electrode structure constraint includes both the macro and microstructure. The macro structure as described in the taxonomy in chapter 1, and the edge collection limits, as described in chapter 2, considered the bulk routing of electrons and protons. From the literature and our calculations, we have concluded that for micro fuel cells of less than 1 W, an edge collected through-plane design is the most appropriate. The microstructure of the electrode describes the interfaces between the catalyst layer, bulk membrane, and GDL, as well as the interfaces between the three main conducting phases (polymer, graphite, and pore)

within the catalyst layer itself. The structure and loading of the catalyst is also included in the electrode structure constraint. Additionally, the electrode structure determines the performance range and efficiency of the fuel cell.

The cost and reliability of the fabrication process is a practical concern, not often addressed in the literature, and is critically important to the eventual commercial success of micro fuel cells. While materials costs do not factor as strongly in small fuel cells as they do in larger stacks, the cost of fabrication tends to increase as a percentage of the total cost as cell scale diminishes. Although chemical vapor deposition and etch techniques are excellent processes for creating and patterning thin and thick films, they are expensive in terms of power consumption, operating time, and materials required for the size of devices we require. Micro fuel cells can be fabricated using traditional MEMS processes, but these processes are expensive. The discipline of micro fuel cells is not at a point in the commercial cycle where fully optimized manufacturing techniques are required; however, any practical micro fuel cell must have the potential for low cost manufacturing.

Finally, the mechanical reliability of the fuel cell must be sufficient to withstand the stresses of the intended application. Structures built out of porous ceramics on single crystal substrates, such as those proposed by D'Arrigo [14], are brittle, and must be carefully handled to avoid failure due to mechanical shock. Mechanical stability is especially important in mobile power markets such as telecommunications devices and military applications. Additional shock absorbent padding required to support a large single crystal substrate and porous ceramic gas diffusion layer negates much of the volume savings gained from MEMS techniques to fabricate the fuel cell. Mechanical properties are often neglected in fuel cell design at all scales because mechanical failures are rarely encountered in a laboratory

environment. However, these effects must be accounted for because they are too difficult to compensate for after the design and fabrication process has been set.

3.2.1 Existing Designs and Fabrication Techniques

Fabrication techniques in the literature are generally discussed in the taxonomy in chapter 1. The specifics of a few key techniques are outlined here. As stated in chapter 1, the fabrication techniques can be broadly classified by the degree of micro fabrication, and the order of operations.

Yu *et al.* presented an excellent example of micro fabricated flow fields combined with standard membrane electrode assemblies [17]. From a fabrication perspective, this approach is very appealing because it separates the electrochemical processes from the flow and current collection. This system allows the use of commercial MEAs to perform the electrochemical work. Although most researchers investigating this technique have used silicon as the base material for the flow fields, it is feasible to replace the silicon with an injection-molded plastic, and maintain the thin film electrode structure for current collection. The disadvantage of this approach is the requirement for compression, which negates much of the volumetric power density advantage.

The second most common approach is the outside-in micro fabrication process. Typical examples of this approach include [5,12] and [14]. The basic premise of the outside-in approach is the creation of a flow field-GDL-catalyst system by subsequent depositions or etches using bulk and surface micro machining. The primary advantage of this approach is the implicit compression, which reduces the volume. There are two serious drawbacks to this approach: first, the new approaches to MEA design require that the empirical guidelines for MEA fabrication be rederived; second, the processes required to make these very complex

supported porous micro structures are difficult to repeat. While not commonly documented, the dimensional instability of Nafion also has an impact on these designs. By removing the compression, the Nafion becomes a mechanical component of the system, but Nafion is not mechanically stable. This effect would be the most serious drawback in Kelly's cell [5], where Nafion acts as an adhesive, but even cells with additional adhesive sealing would experience some degradation due to the stresses because of the dimensional change of Nafion.

An uncommon approach is the inside-out approach where the fuel cell is built by successive depositions on the membrane. This approach is rare because bulk Nafion's dimensional instability make it an unsuitable substrate. The one documented inside-out design by Shah *et al.* [18] does not provide any lifetime information. Shah also uses a thin film catalyst layer with uncertain loading and activity. Although this architecture is potentially manufacturable, it has poor performance and little mechanical reliability.

No architecture is entirely problem-free. For larger cells, the traditional plate and frame approach (see Figure 1) is appropriate because the working volume is larger, and the total cell active area to compression plate volume ratio is sufficiently large. For smaller cells, the working volume prohibits the use of compression; therefore, so the outside-in or inside-out architectures are required. Table 12 summarizes the advantages and disadvantages of the two potential fabrication processes from a fabrication perspective.

Table 12:Comparison of micro fuel cell architectures

Parameter	Inside-Out	Outside-In
Thickness	Good	Good
Electrode Structure	Poor	Poor
Manufacturability	Good	Moderate
Mechanical Robustness	Poor	Moderate

Based on Table 12, neither option is particularly compelling. Although both satisfy the thickness requirement for very small fuel cells, neither offers a clear overall performance benefit. By addressing the shortcomings of either design through research, either option could be determined to be a viable solution. In both cases, the requirement to re-engineer the electrode structure from the traditional MEA leads to poor performance because the empirical guidelines for electrode design must be rederived. In both cases, a spray deposited carbon-supported catalyst can be used in place of a thin film catalyst, reducing the required research on electrode structure. The manufacturability of the outside-in design is difficult to address because manufacturing porous media supported over channels is challenging. The mechanical robustness of outside-in architectures can be addressed by substituting a less brittle substrate and GDL. The mechanical robustness of the inside-out architecture can be addressed by replacing Nafion with a dimensionally stable substrate.

The inside-out design can be addressed by the appropriate electrode design and stabilizing the mechanical characteristics of the membrane. Architectures that require new materials are generally not realizable, because the risks involved in new material development are significantly higher than designing an architecture with existing materials. However, research [78-90] indicates that dimensionally stable membranes are feasible. One shortcoming of the inside-out design is the dependence on thin film catalysts layer and current collectors. Using a stencil-based approach, a packed-bed catalyst layer can be deposited on a dimensionally stable substrate. According to the simulations in chapter 2, a high conductivity GDL is required for an edge-collected, inside-out membrane.

3.2.2 Fabrication Process Motivation

Based on the literature analysis in chapter 1, the theoretical analysis in chapter 2, and the preceding analysis of the advantages and shortcomings of feasible fabrication techniques, as we prepared a detailed design of the fuel cell architecture. From this architecture, we designed a fabrication process, architecture and new materials requirements.

While most researchers treat materials, fabrication, architecture and performance as separate entities, they are inexorably linked. The manufacturing or fabrication process is a series operation on specific materials. The final properties of the materials after fabrication have a significant impact on the performance. Most researchers assume that all but one or two factors are fixed, that architecture, materials, or fabrication is taken from the existing literature as optimized, and the other factors are investigated. In general, this approach is an efficient and appropriate method of conducting research. In an emerging field such as fuel cell research, however, no parameter can be properly regarded as optimized, or even approaching optimization. To realize substantial advances in fuel cell technology, architecture, fabrication and material domains must be addressed simultaneously. Although considering advances in all areas of research opens the door to new designs, this approach also significantly increases the research risk.

Based on the analysis of the problem, we have generated a new fuel cell based on the integration of new materials, fabrication processes, and architecture. We can synthesize the results of our analysis into a design, fabrication process, and specifications for new materials.

3.2.2.1 Electrode Fabrication Requirements

From our theoretical analysis in chapter 2, we require an edge-collected electrode of less than 20 cm in length composed of sequential catalyst, gas diffusion, and thin film current

collectors layers. The demands for scale and low cost manufacturing imply that we must be able to create these electrodes without mechanical assembly. Surface MEMS techniques of sequential deposition, patterning and etching are a viable first option. However, the etch chemistries for the individual layers of noble metals are not selective, making patterning individual layers difficult.

The challenge in patterning thick films, and the lack of a selective wet etch chemistries, implies that the patterning must occur during the deposition process. For micro devices on a scale of less than 50 μm, patterning the electrodes directly would be difficult. Some micro printing and self-assembly methods exist, but they have low repeatability and are expensive. However, we know from our theoretical work that the features within a micro fuel cell are usually greater than 100 μm. Several methods exist for patterning features on a scale greater than 100 μm. Direct printing methods, such as syringe or inkjet printing can achieve these scales with the correct ink and substrate. Stencils built from substrates such as silicon, polymers, or metals are possible. Stencil techniques are analogous to the MEMS lift-off techniques, although instead of the stencil being etched away after deposition, it is removed mechanically.

Stencils have several advantages over printing for prototype systems. For example stencils can be used in conjunction with existing catalyst inks. However, for effective inkjeting of catalyst inks, significant research into the ink is required. Another advantage is that stencils can be applied to all process steps including thick and thin film deposition; once a stenciling process has been created it can be applied to all layers by creating different stencils from the same material. Finally, stencils can be created using standard MEMS techniques, allowing the use of existing equipment.

In a standard macro fuel cell, the gas diffusion layer is a carbon felt or cloth, which is hot-pressed into the Nafion substrate. Because carbon cloth is neither depositable nor patternable, either a new GDL material is required or the GDL must be removed from the fuel cell. Our simulations and calculations have shown that edge collected cells without gas diffusion layers are impractical. Therefore, a new electrochemically compatible GDL material with a conductivity of at least 50,000 S/m and a porosity of at least 50% is required.

The electrodes can be fabricated from standard catalyst inks, a new membrane depositable GDL, and thin film noble metal current collectors. The layers can be patterned using micromachined stencils. The method of stencil creation and application, and the GDL material are the key individual research topics.

3.2.2.2 Substrate Fabrication Requirements

In inside-out fabrication, the membrane serves as a substrate. Although Nafion is an excellent solid ionomer, its mechanical properties are not consistent with requirements of a substrate. In particular, the dimensional change of Nafion when its water content is altered, leads to very short-lived fuel cells. The impact of the dimensional change is dominant in inside-out fuel cell architectures, but has an impact on outside-in architectures as well. Outside-in architectures must have a secondary adhesive seal strong enough to compensate for the dimensional change of the Nafion, in order to hold the cell together during deformations.

A new dimensionally stable solid electrolyte is required for a practical inside-out architecture. A new polymer or ceramic electrolyte might be created by material scientists to meet this requirement, but that work is well beyond the scope of this thesis. However, we can draw on earlier work in supported membranes to create the desired substrate. A supported membrane is a composite where the polymer is combined with an inert material to provide

mechanical strength, like fiberglass, or rebar and concrete. Gore has created a pre-commercial polytetrafluroethylene (PTFE)-Nafion composite membrane with better dimensional stability [78]. However, for the dimensional stability that we require, a more rigid supporting matrix is required. Glass is a suitably inert and rigid supporting matrix.

To successfully create an inside-out fuel cell, research was required to create a dimensionally stable membrane to act as a proton conductor and substrate. The conductivity should be consistent with bulk Nafion, and the mechanical strength should permit operational wear and tear, and should survive the fabrication process.

3.2.2.3 Flow Field Fabrication Requirements

Because the current collection in an inside-out edge collected fuel cell occurs along the GDL, the flow field requirements are considerably relaxed. The flow field must route the fuel along the anode, nothing more. Because the flow field requirements are relaxed, a wide variety of materials are suitable. From a cost, machining, and electrochemical compatibility perspective, injection molded polymers are the best long-term solution. The chosen polymer must be inert in a fuel cell environment, mechanically robust, and easy to form.

However, injection molding is not a process amenable to prototyping. Therefore, in the short-term, a process which mimics the results of injection molding, but more applicable to small batches would be appropriate. Soft-lithography of curable polymers on micromachined molds is an appropriate compromise between small production size and final applicability.

The calculations performed in the previous chapter indicate that the flow fields for the anode side should be between 200 and 400 μm in depth for liquid feed fuel cells. Molds created using the UV curable epoxy SU-8 2100 from Microchem meet these requirements. PDMS is typically used as a gasket material in larger fuel cells. It is also commonly used in

soft lithography. A PDMS flow field created using soft lithography meets the basic requirements of compatibility, mechanical durability, and ease of forming.

3.2.3 Fabrication Process

Our fuel cell fabrication technique is based on a sequence of thin and thick film depositions on a stable membrane substrate. Employing a dimensionally stable membrane as the substrate allows us to build the fuel cell in layers from the membrane out, without losing film integrity. Two fabrication paths are shown in Figure 38, the theoretically preferred GDL based system on the left, and the simpler but poorer performing catalyst-only design on the right.

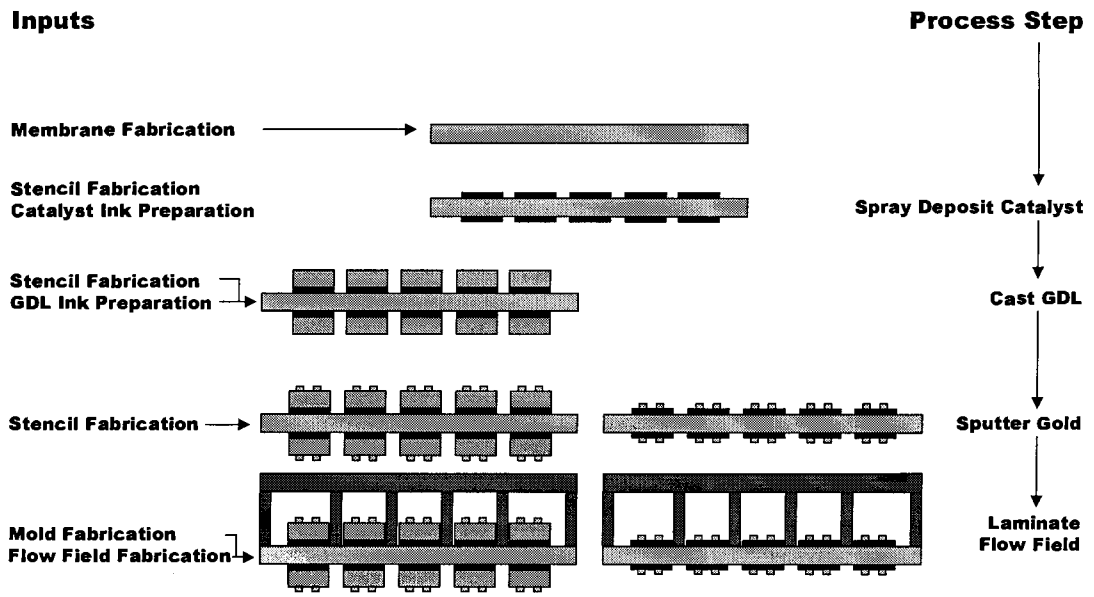

Figure 38: Fabrication process for the micro fuel cell

In Figure 38, the cross section of the fuel cell is shown in the center, the name of the deposition step is shown on the far right, and the required material, tool and die, and component processes, which feed into each step, are shown on the right. For example, the deposition of the catalyst layer requires the preparation of a micromachined stencil, and the catalyst ink.

The process begins with the fabrication of a dimensionally stable membrane. A porous glass substrate loaded with Nafion provides a supporting matrix for the solid electrolyte. Next, the catalyst layer is sprayed through a stencil to create a sequence of segmented electrode regions. The regions are then edge-connected to a sputtered gold current collector. The membrane-catalyst-gold assembly forms an MEA where bulk current collection occurs on the membrane, removing the compression requirement to reduce current collector-MEA contact resistance. In parallel, a set of silicone channels is formed by casting silicone over an SU-8/silicon mold. These channels are then attached to the MEA using a silicone-based RTV adhesive.

3.3 Membrane Preparation

Perfluorosulphonylated ionomer (PFSI) membranes are typically used as the electrolyte in PEM cells. Currently, Nafion from Dupont is the de facto standard for commercial grade proton exchange membranes. Nafion's combination of mechanical strength, high proton conductivity, and chemical compatibility are difficult to match with new materials. However, Nafion does have the disadvantages of cost, dimensional instability, and water management.

Supported membranes based on polytetrafluoroethylene (PTFE)/PFSI hybrids have been reported [78-87] with higher strength, greater dimensional stability lower cost and lower conductivity than Nafion membranes. Their higher mechanical strength permits thinner membranes, and therefore lower resistance through the membrane.

Liu and Martin described the behavior of Nafion-impregnated Gore-Tex membranes in [78, 80, 81]. This is some of the earliest reported work in supported membranes for fuel cells. Although they were primarily concerned with Nafion's utility as a cation exchange membrane, their work was the foundation for much of the research that followed.

Using radio-tracing methods, Verbrugge *et al.* examined the effects of PFSI loading in PTFE membranes on water transport, and found that with increasing PFSI, content shifted from hydrophobic to hydrophilic through a transition region where both behaviors were exhibited [82].

Both Celgard and Teflon supported membranes were examined by Nouel and Fedkiw [83]. They found that while their membranes were less permeable to oxygen and nitrogen than the porous membranes, still significant permeation was still evident. The poor performance was likely due to their use of a single coat of Nafion solution, which after solvent drive off, would not have sufficient Nafion loading to completely fill the pores.

Melt-processed Nafion-PTFE membranes were investigated by Kwak *et al.* [84], where they hot pressed a Nafion sheet into a PTFE membrane. They presented scanning electron microscope (SEM) photographs of different stages of the process and polarization curves of their membrane compared to Nafion 115. At the modest power densities examined their membranes performed well compared to Nafion.

Jiang *et al.* described a Teflon supported Nafion membrane [85]. Whereas this approach is amenable for gas separation membranes, it is not suitable for fuel cells. In a supported structure, only one face of the membrane has substantial Nafion content, while the other is primarily Teflon.

By using thin membranes, Shim *et al.* were able to increase the percentage of Nafion loading and reduce the oxygen and nitrogen permeation [86]. While the permeability to nitrogen was three orders of magnitude higher than Nafion in the composite membrane, the rate of crossover was small enough to not significantly impact the fuel cell polarization curve significantly.

While most composite proton exchange membrane researchers have examined Teflon-Nafion systems, Pan *et al.* created a sulphinated styrene-butadiene-styrene (SBS)/glass membrane [87]. The glass fiber composite more than doubled the strength, reduced swelling to a third, and halved water uptake without compromising conductivity, when compared to the raw SBS membrane.

Asahi Glass fabricates the Flemion proton exchange membrane [88]. Asahi has evaluated the behavior of Flemion/PTFE membranes presented their results at the New Materials conference in 1999. They documented an order of magnitude increase in dimensional stability; increased mechanical strength and a small increase in resistively.

In a detailed study of the mechanical properties of PTFE/Nafion membranes, Liu *et al.* demonstrated significant increases in mechanical strength and dimensional stability for the hybrid membrane over Nafion 115 in both wet and dry conditions [89]. While the resistance of the membrane was higher, the membrane was physically stable to 25 μm thickness, allowing much thinner membranes to be used.

PTFE supported membranes are somewhat difficult to manufacture because the support is hydrophobic. Solvent substitution of the PFSI ionomer is required to remove water and replace it with alcohols or other organic solvents. However, to the best of our knowledge we are the only group to report the behavior of a glass fiber supported Nafion membrane in the academic literature. A team from Johnson-Matthey Corp. has reported a glass supported composite membrane [79] in the patent literature, and demonstrated the feasibility of glass as a support for a composite membrane.

Glass fibers are an attractive support because they are inexpensive, hydrophilic, easy to manufacture, and chemically inert. Because glass has ceramic mechanical material

characteristics, the mechanical properties of our membrane are substantially different than PTFE-Nafion and other polymer composite membranes. Glass fibers can also act as a less expensive, easily manufactured, composite membrane.

3.3.1 Alternate Membrane Approaches

Alternate supported membranes as outlined in the literature review, or bulk Nafion can be used as a membrane for academic research on micro fuel cell topologies, as noted in the literature review and taxonomy in chapter 1. We have investigated the feasibility of both these approaches and found them wanting.

While fabricating an inside-out micro fuel cell based on a bulk Nafion substrate is tempting, the dimensional change of Nafion due to water content cycling creates serious stresses in any films deposited on the membrane. Outside-in fuel cells without external compression, such as [17] and [27], are likely to delaminate with Nafion dimensional cycling. Results for inside-out fuel cells obtained with bulk Nafion in the literature [18,30] are likely valid, but difficult to repeat, because the deposited films would quickly degrade. Figure 39 shows the result of the dimensional change of a 250 nm thick aluminum trace on Nafion 117.

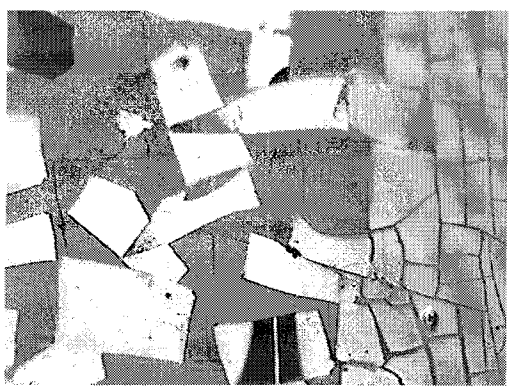

Figure 39: Aluminum film on Nafion

The aluminum was sputtered on a Nafion substrate, which was allowed to reach equilibrium with the ambient air overnight. The Nafion was immersed in DI water for 1 minute prior to the image being capture. The image was taken at 100x magnification under an optical microscope. The picture clearly shows that the thin film has suffered considerable duress. The fragmentation of the film significantly decreases, and potentially destroys, the film's conductivity. To verify the effect of Nafion we created cells with the same processes and topology and subjected them to testing. The cells were generally stable for a single polarization curve test, but delaminated after the cells returned to water vapor equilibrium with the surrounding air. The polarization curves for the Nafion membranes can be found in Figure 57 and Figure 58.

W.L. Gore and Associates Inc. have a pre-commercial membrane based on a Teflon support. We initially attempted to replicate the Gore technology as a supported membrane for our use. However, the Teflon supported membranes were much more difficult to fabricate because Teflon is hydrophobic. Loading thick solutions into hydrophobic pores is a complicated process, even with low water concentrations in the solvent. The solution tended to pool at the top or the bottom of the membrane, forming thin fully dense layers on the top and bottom of the membrane, which isolated the anode from the cathode, and prevented current flow, as shown in Figure 40.

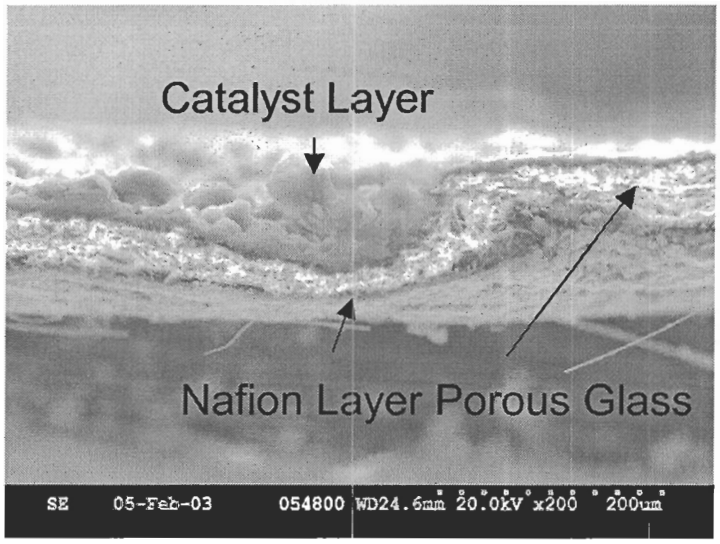

Figure 40: Teflon membrane and catalyst

In Figure 40 the bright inner area is Teflon fiber, the thin conducting layer on the top is the electrode and bottom is the Nafion. AC impedance measurements of the surface showed the membrane was conductive, however, the fuel cell did not operate because, because there is an open ionic circuit between the top and bottom. While Gore's success demonstrates the feasibility of Teflon supported Nafion membranes, we were unable to reliably fabricate in the laboratory.

3.3.2 Fabrication

The membrane is fabricated by sequential immersion and drying in a bath of ionomer solution. The strength of the solution has a significant impact on the final behavior of the membrane. Weak solutions, such as the standard 5% Nafion solution (Alfa Aeser), require 6-8 coats of Nafion for sufficient impregnation. The repeated immersion of the glass fiber in solution can cause catastrophic failure of the support because of stresses placed on the mesh due to uneven wetting and over-handling when wet. In extreme cases, the fiber matte can flow, doubling the diameter of the membrane, and introducing significant pinholes. An

example of a reflowed membrane is shown in Figure 41. The upper-left membrane is largely intact, while the bottom right membrane has failed.

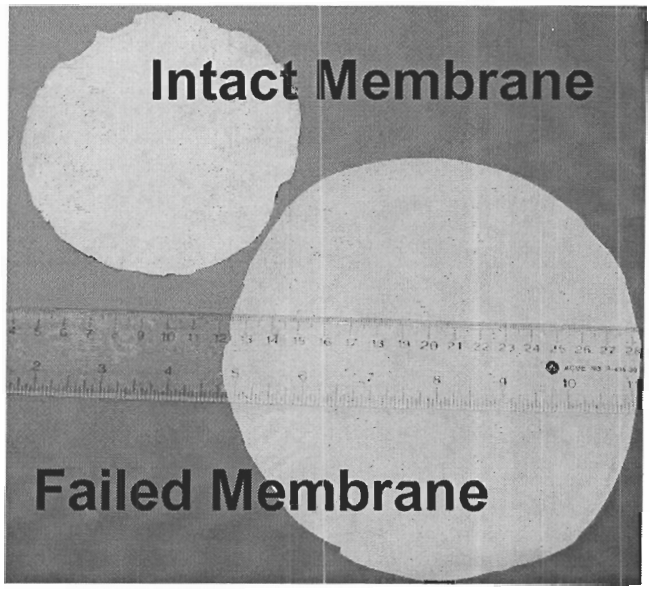

Figure 41: Effect of membrane failure due to slumping

The drying process is critical to the final properties of the membrane: if the solvent is driven off too quickly the ionomer is left in thin sheets, like a pastry; if the solvent is not sufficiently removed, it becomes sealed in pockets, creating bubbles and internal dislocations, because the surface ionomer dries before in the internal ionomer, thus trapping the solvent inside. Figure 42 shows three cross-sections of different membranes to illustrate the impact of solvent drive off rate.

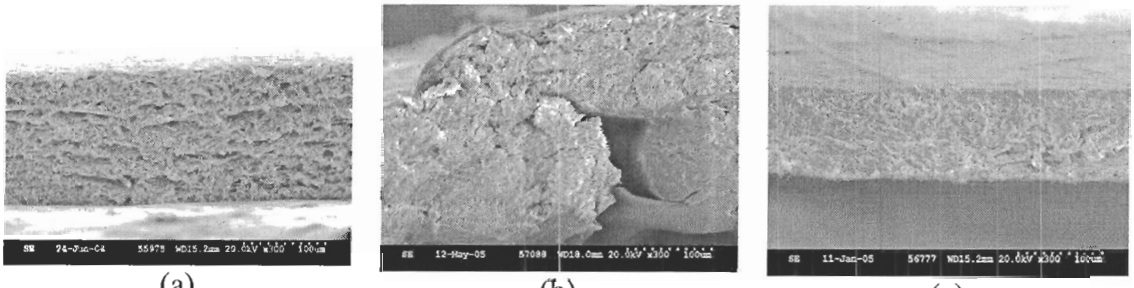

(a) (b) (c)

Figure 42:Comparison of membrane quality with respect to solvent viscosity

Figure 42 shows the SEM images of membrane cross sections using different solvents and concentrations. Image (a) in Figure 41 shows a membrane made using 5% Nafion in 40% alcohol and 60% water solution from Alfa Aeser. The membrane is characterized by a layered texture, similar to a pastry. This layering reduced the tensile strength and through-plane conductivity of the membrane. The second image shows a membrane fabricated with a 25% DMF (N,N-Dimethylformamide) Nafion and rapid drying. The defect shown is the result of a blister formed during the vacuum drying process. While the membrane can be superficially repaired by hot pressing the membrane, it is apparent from the image that the blister does not completely reattach to the membrane. The final image shows a membrane fabricated with 25% DMF.

Membrane fabrication is performed by sequential emersion of 90 mm diameter untreated glass fiber filters (Osmonics G40WP09000) in the DMF-PFSI solution under vacuum. A clean, dry glass membrane is placed in the solution then heated to 40 C in a vacuum oven. The elevated temperature reduces viscosity and reduces the time required to fully wet the membrane. The vacuum oven is pumped down to 20 inches/Hg vacuum, and held for 60 s. The oven is then purged and the process repeated. After immersion, the membrane is extracted from the solution and placed on a clean PTFE sheet for drying. The membrane is dried under 20 inches/Hg vacuum at 80 C for 4 hours, then fewer than 25 inches/Hg at 80 C for a minimum of 8 hours. This process is then repeated, adding a second coat.

The membranes are hydrated by immersion in deionized water for 1 hour at 80 C, and protonated in 10% sulfuric acid for 1 hour at 80 C. After a final rinse, the membranes are allowed to air dry at room temperature. Often a small amount of warping occurs, which can

be removed by hot pressing the membranes between PTFE sheets for 3 minutes at 155 C under 1 US Ton.

Although the same conditions for membrane preparation are maintained throughout the process, repeatability was difficult to achieve in our laboratory environment. While the data presented in the results section is typical for the membranes we have fabricated, some variance in the quality of membranes produced. This variance may be minimized in an industrial environment with automated control systems.

3.3.3 Mechanical Strength

Two 1 cm by 8 cm samples of the membrane and Nafion 117 were prepared using a scalpel for mechanical strength characterization. Each membrane was placed in the pull-tester (Test Resources 2000R) with 4 cm between the clamps and subjected to a linear load increase until the membrane yielded. Membranes were tested in at ambient temperature and humidity, 22 C and 85% respectively. The applied load and displacement were measured by the system. Stress was calculated according to

$$\sigma_s = \frac{F}{A_0} \tag{57}$$

where F is the applied force and A_0 is the cross sectional area, and strain according to

$$\varepsilon = \frac{\Delta l}{l_0} \tag{58}$$

where Δl is the change in length, and l_0 is the starting length. Example stress-strain curves are shown in Figure 43.

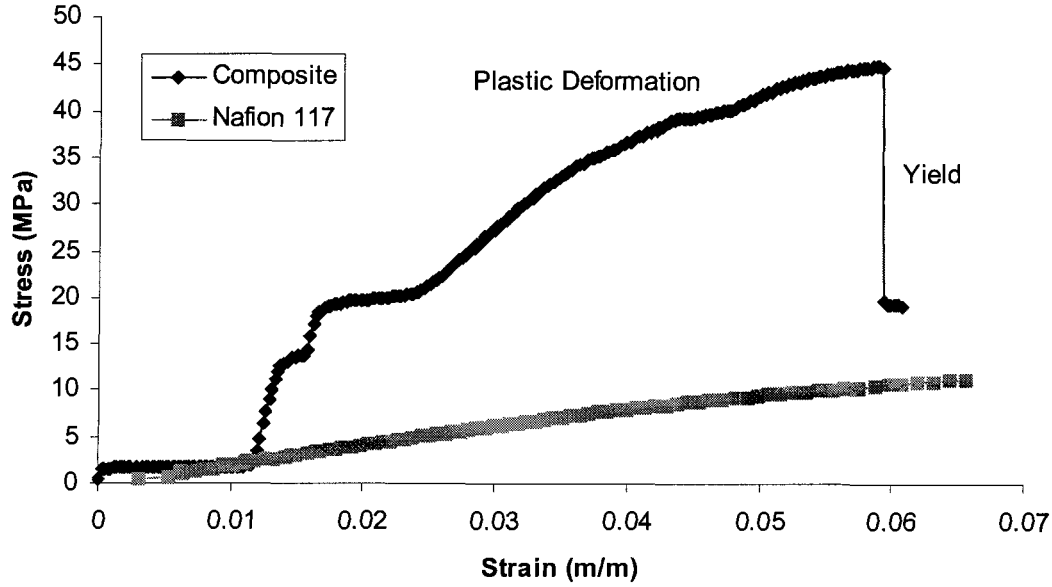

Figure 43:Stress-Strain curves for composite membrane and bulk PFSI

The stress-strain plots show very different mechanical behavior for the glass supported composite membrane and pure Nafion. Some slip occurred between the clamps and sample during the composite membrane trial. Clamp slip may have contributed to the steps visible in the composite curve. The supported membranes have a stress-strain behavior reminiscent of a metal, with a linear elastic region, a deformation region, followed be failure. Nafion, on the other hand, behaves like a plastic, continuously deforming under stress. Although the Nafion 117 has a greater tensile strength than the composite membrane, yielding at approximately 26 MPa [89], it undergoes a continuous deformation, which may be detrimental under reel-to-reel manufacturing conditions.

Given that the membrane is a polymer-glass composite, the mechanism leading to the stress-strain curves are very different from a metal. The initial low-deformation region is approximately linear, and glass-like. We believe that in this region the glass fibers form the primary load support. In the subsequent region, a polymer-like behavior is observed. In this

region, we believe that the glass fibers have yielded, and the composite is held together by threads of polymer, assuming spring-like characteristics. When these thin springs yield, the composite breaks. Like Verbrugge *et al.* [82], we found that Nafion composites behave as composites both physically, and chemically.

Table 13 compares the mechanical characteristics of our composite membranes against others published in the literature. Results from Yoshitake *et al.* [88] and Liu *et al.* [89] are PTFE-Nafion composites, and exhibit large elongation at yield. Our results and those of Pan *et al.* [87] are for glass-polymer composites, exhibiting a much lower elongation at yield.

Table 13: Strength and elongation of selected membranes

Paper	Tensile Strength (MPa)	Elongation (%)
PTFE-Nafion Yoshitake et al. [88]	24.5	160
PTFE-Nafion Liu et al. [89]	41.4	Unreported
Glass-SBS Pan et al. [87]	41	Unreported
Nafion 117 [94]	43	225
Nafion-212 [95]	32	343
Glass-Nafion Stanley	45	6.1

Our supported membrane exhibits the superior mechanical characteristics to those reported in the literature, with the highest tensile strength and the lowest elongation. For most of the reported results, the tensile strength is similar to that of Nafion, which is a reasonable conclusion given our analysis of the stress-strain curves. The substantially smaller elongation results from the glass fiber support as opposed to the PTFE support. These mechanical characteristics not only improve the dimensional stability as required for the micro fuel cell fabrication, but also allow the membrane to be used in higher stress manufacturing environments such as a reel-to-reel printing line.

3.3.4 AC Impedance

Four samples of each membrane, 1.5 cm long and 1 cm wide, were soaked in 1 M sulfuric acid overnight, and then rinsed in DI water. The samples were placed in a PTFE ring with planar platinum electrodes, spaced 1 cm apart. The configuration and associated equivalent circuit are shown in Figure 44.

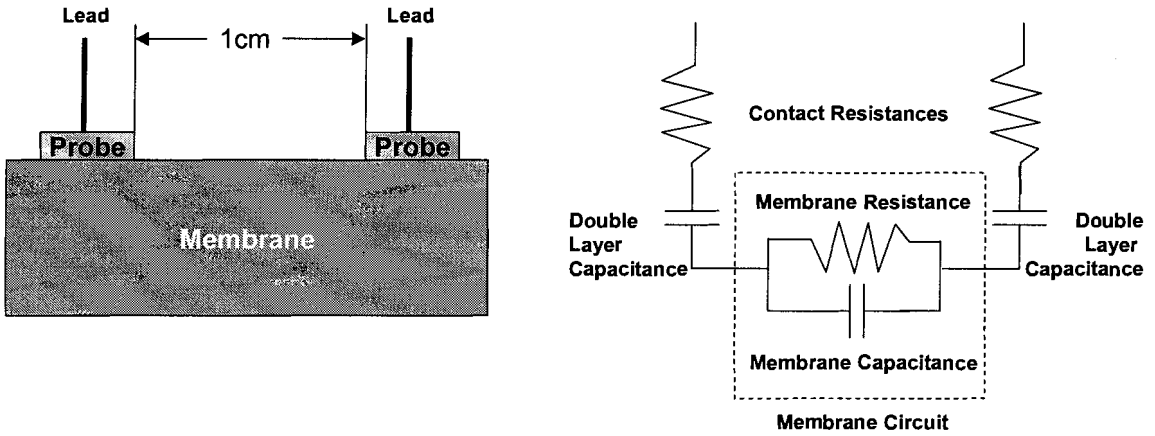

Figure 44: Schematic layout and equivalent circuit for membrane AC Impedance evaluation

Through plane resistances were measured to increase the impedance between the leads and therefore signal to noise ratio. The equivalent circuit in Figure 44 shows the overall equivalent circuit for the membrane and measurement apparatus. The contact resistances account for all the parasitic resistances in the test apparatus, including lead resistances and contact resistances between the leads and platinum probes. The double layer capacitance accounts for the capacitive interface between the electrically conducting probe and the ionically conducting membrane. The membrane itself has both resistive and capacitive behaviors. We are primarily interested in isolating the resistance because fuel cells produce direct current, and the capacitive elements of the membrane can be neglected during fuel cell operation.

The entire assembly was placed in a beaker containing DI water. The AC impedance of the membrane was measured using a Solatron SI1260 impedance analyzer and ZPlot and ZView software from Scribner Associates. After every measurement the DI water in the beaker was changed, to avoid altering the measurement through an accumulation of proton in the water bath from the samples. The real part of the conductivity was taken as the point on the first semicircle closest to the real axis. The length and width of the membrane were measured using calipers and the thickness of the membrane was measured using a micrometer. The conductivity of the membrane calculated as

$$\sigma_p = \frac{L_e}{w_m t_m R} \tag{59}$$

where σ_p is the proton conductivity, L_e is the distance between the electrodes, w_m is the width of the membrane, t_m is the thickness of the membrane, and R is the measured resistance. The average conductivity of the four samples from each loading condition is taken to be the conductivity of the membrane.

The conductivity of the membranes was evaluated using the AC impedance technique [96]. The resistance of the membrane was taken as the closest non-origin point to the real axis on the Cole-Cole plot according to standard practice. AC impedance measurements for samples of three different membranes prepared in the same batch are shown in Figure 45.

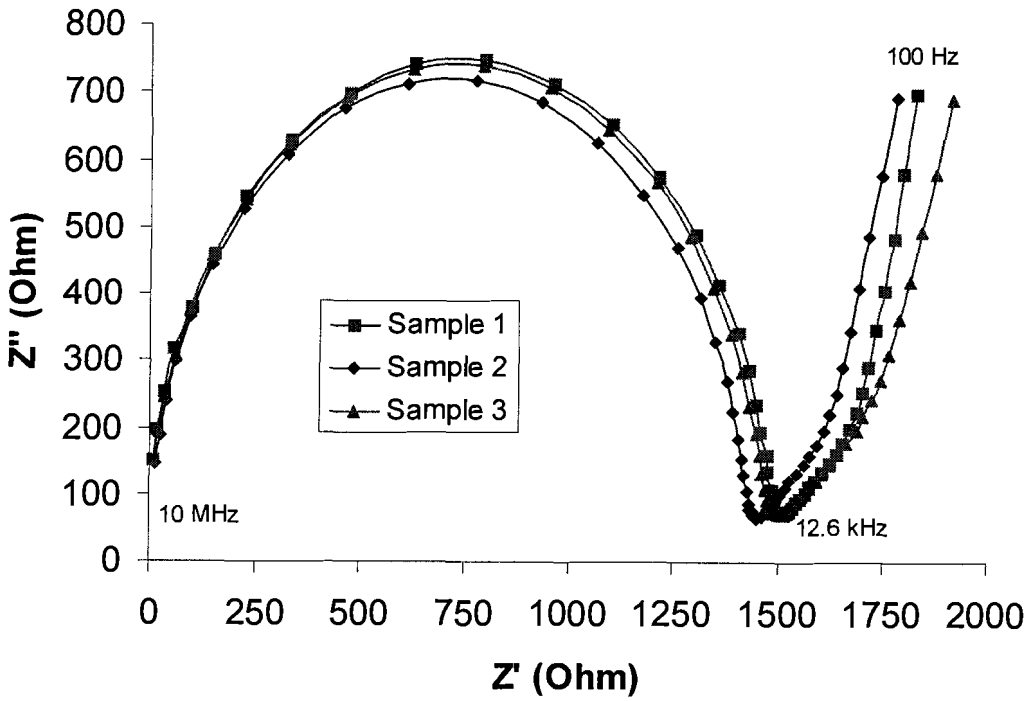

Figure 45: Cole-Cole plots for membranes

In the above diagram, low frequency is dominated by the double layer capacitance between the probes on the membrane. As frequency decreases, the impedance of these capacitors increases, causing the low frequency response to trend to infinity. At very high frequency, the Nafion itself acts like a capacitor, and the impedance trends towards the origin, with a small offset for the contact resistance and test lead resistance. The contact resistance is typically less than 10 Ω, lower than the membrane resistance, and can be ignored. At intermediate frequencies, the double layer impedance is low, but the internal impedance is high. The overall effect is the semicircular plot, with a low frequency tail trending to infinity as shown in Figure 45. The closest point to the real axis was taken as the membrane resistance along the 1 cm electrode, because the contribution from the capacitive components was minimized. For context Bode plots of the same data are shown in Figure 46 and Figure 47.

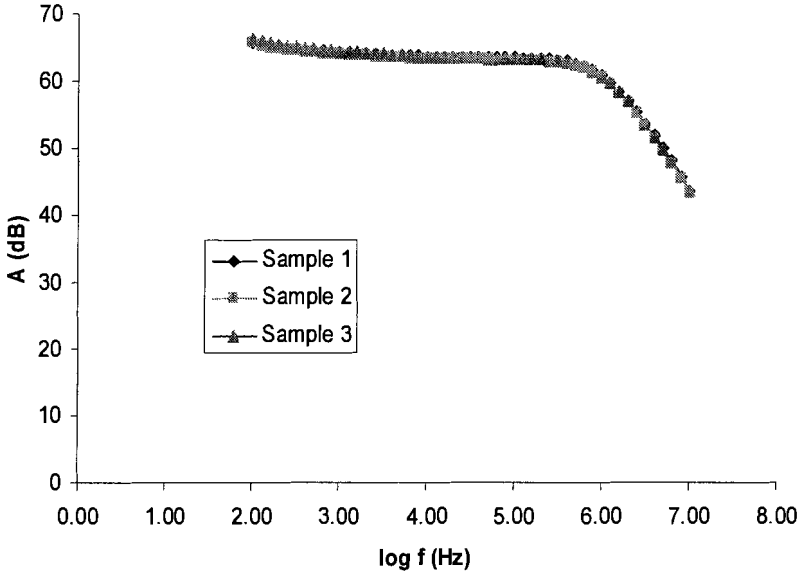

Figure 46: Amplitude vs. log frequency for membrane

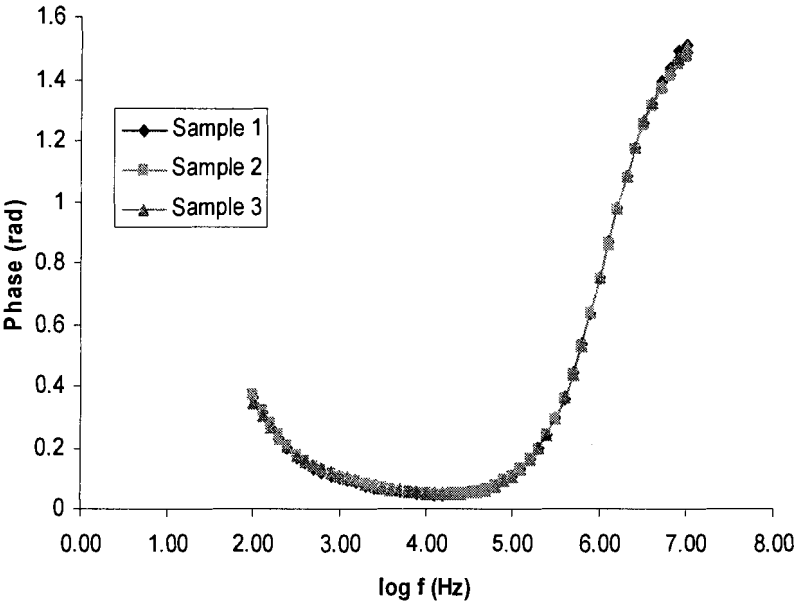

Figure 47: Phase vs. log frequency for membrane

The Bode plots clearly show the same behavior as the Cole-Cole plots. The pole in the Bode plot is at approximately 1 MHz, which corresponds to the peak of the Cole-Cole plot. The phase is at a minimum at approximately 10 kHz, corresponding to the minimum in the Cole-Cole plot.

The conductivities of our membranes, compared to Nafion and the results from [83] are shown in Table 14.

Table 14:Conductivity of selected membranes

Membrane	Conductivity (mS/cm)
Composite Membrane	43
Nafion 117 [94]	83
Nouel and Fedkiw [83] Celgard	27
Nouel and Fedkiw [83] PTFE	101
Nouel and Fedkiw [83] Gore-Select	63
Nouel and Fedkiw [83] Nafion 112	140

The conductivity of our membrane is approximately 50% of Nafion of similar thickness, as expected given our membrane is approximately 50% Nafion by volume; therefore, its material conductivity should be the same, but the effective cross section should be halved. The graph shows that the membrane will either have to be half the thickness of Nafion or the fuel cell will have to operate at a lower current density for our membranes to be effective. Thin glass membranes are easy to obtain. Because we designed this membrane with portable applications in mind, lower current densities associated with portable electronics are expected, reducing the magnitude of Ohmic losses through the membrane. The conductivity data shows that while the conductivity is proportional to Nafion loading, increasing the resistance through the membrane, it is still feasible to make practical fuel cells with this membrane.

3.3.5 Water Content

Water retention was determined by the change in mass before and after dehydration in a vacuum oven. The water content is expressed as the percentage weight change during drying with respect to the Nafion content of the membrane. The membranes were soaked overnight in deionized water, then patted dry with a Kimwipe and weighed. The membranes were dried under a vacuum of 30 mm Hg and 80 C for more than 6 hours. The change in mass was assumed to be entirely due to change in water content. For the DMF membranes, water content was estimated to be 15% (g/g) whereas Nafion has a water content of 21% (g/g) [89]. The reduction in water content may be due to the restriction on physical deformation, which limits the water content once it reaches the concentration where Nafion must expand to accommodate more water.

3.3.6 Permeability

In order for a solid electrolyte to be effective, it must be gas impermeable. Pinholes in the membrane permit reactive elements to mix on the cathode, creating a mixed potential, and degrading the performance of the fuel cell. To evaluate the permeability of our membranes we employed a helium leak detection setup as shown in Figure 48.

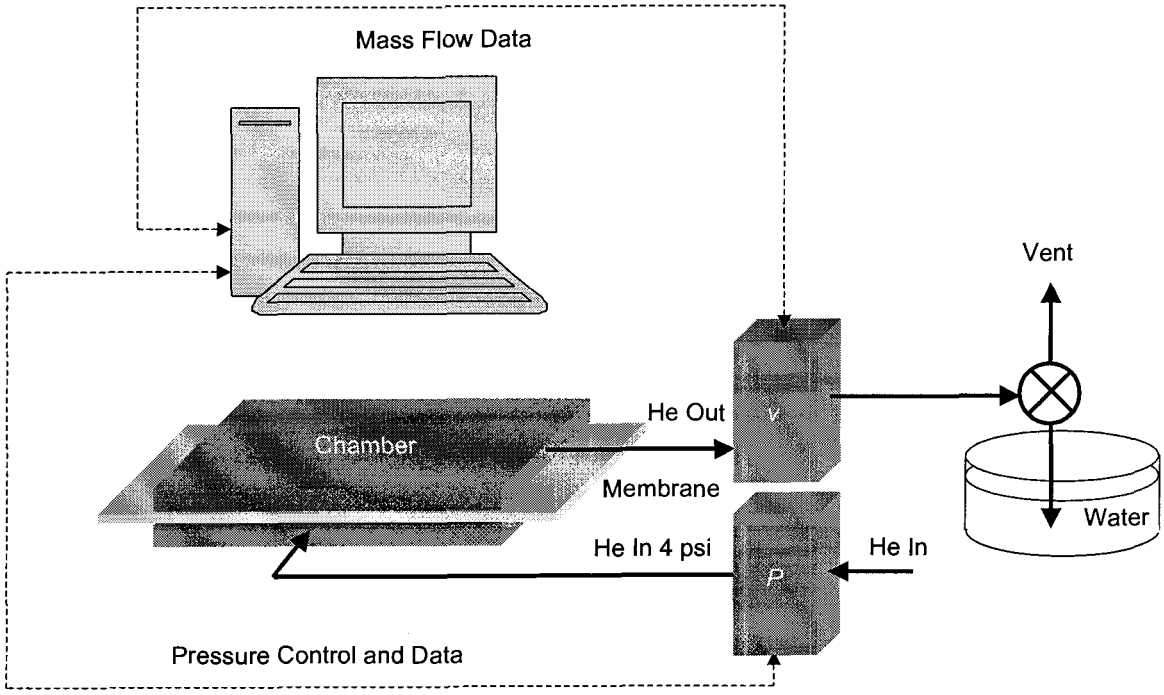

Figure 48:Leak detection apparatus

The membrane is placed between two chambers with silicone o-rings. A computer controlled pressure regulator (Alicat) is used to set the input pressure to 4 psi. Helium is allowed to percolate through the membrane and passes through a highly accurate mass flow meter (Alicat), which is connected to a computer for data logging. The output of the flow meter can be routed through a valve to a vent for direct measurement of the flow rate, or into a pipe in a water bath for a bubble-count measurement of the leak rate.

Measurements were taken in three stages. For membranes with a base leak rate higher than 25 sccm, the membrane was immediately rejected and no further measurements were made. Membranes that passed the initial test were then tested by both bubble counting and direct measurement. For membranes with a leak rate below 10 sccm, the bubble count was required to confirm the results of the direct measurements because the resolution of the flow meter was 3 sccm, and the noise floor was approximately 5 sccm. Bubble counts were performed by

analyzing the flow meter data logs. After a sufficient pressure builds up behind the free surface within the submerged outlet, the bubble begins to form, and the resistance against the flow decreases dramatically. The decrease in resistance corresponds to an increased flow rate through the mass flow meter until the bubble begins to detach, then the resistance increases and the flow rate decreases. Taken over a period of minutes, this behavior leaves a recognizable pulse train in the flow meter data as shown in Figure 50.

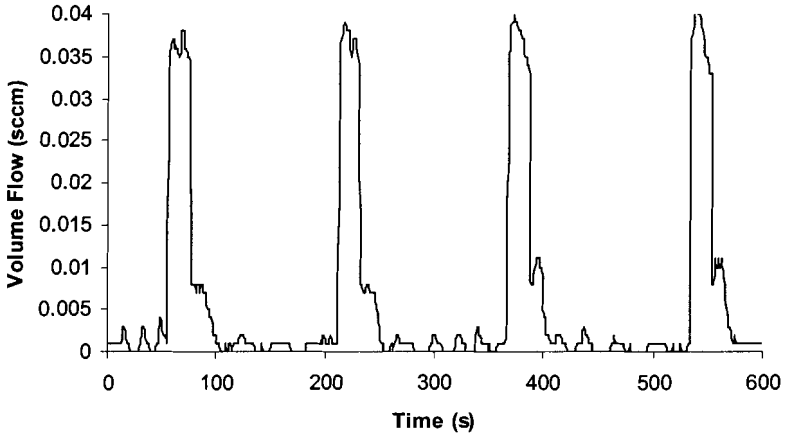

Figure 49: Bubble detection using flow rate for Nafion 117

Figure 50 shows instantaneous flow through the membrane under a backpressure of 4 psi helium. The thickness of Nafion was approximately 175 μm. Bubble volume was calibrated by counting the number of bubbles required to displace 5 ml of water in a graduated cylinder. By assuming that all bubbles are approximately equal in volume, the volume per bubble is simply the volume displaced divided by number of bubbles. Our calibration estimates bubble volume as 15.5 μl. In the above graph, the bubble based flow rate calculation is 6.2 μl/min. Integrating the entire curve, and dividing by the total duration, gives a result of 6.3 μl/min, indicating that our calibration is reasonably accurate.

Supported membranes measured using the same apparatus generate similar pulse trains to the Nafion membrane shown Figure 49. Figure 50 shows a composite membrane measured under the same conditions and apparatus. The membrane in this graph is slightly thinner than the Nafion 117, which partially explains the slightly higher leak rate. The thickness of the composite membrane was approximately 135 μm, 30% thinner than the Nafion 117.

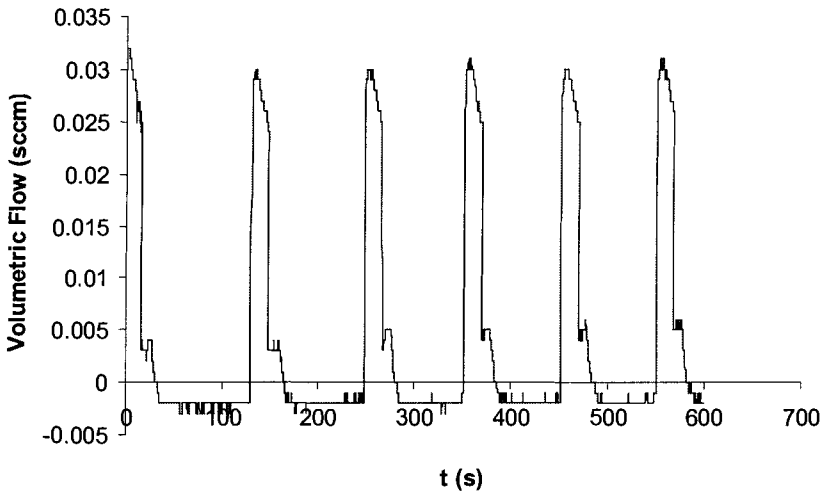

Figure 50:Bubble detection using flow rate for a composite membrane

The small negative value in the graph is due to a systematic error in the measurement apparatus. Based on the calibrated bubble method of estimating the flow, the leak rate for the membrane was 9.3 μl/min. The slightly higher leak rate is proportional to the difference in thickness. The leak detection apparatus was used to screen membranes and eliminate membranes with a leak rate of greater than 25 μl/min from further fuel cell processing.

3.3.7 Dimensional Stability

Dimensional stability of the membrane is crucial to our design [90]. We evaluated dimensional stability by recording the dimensions before and after dehydration in a vacuum oven.

Table 15:Surface area stability of membranes

Membrane	Surface Deformation (%)	Volume Deformation (%)
Stanley et al.	0.37	3.8
Nafion 117 [94]	21	31
C-325 Liu et al [89]	11	25
Nafion 112 Liu et al. [89]	24	55
Pan et al. [87]	3.7	20.6

The surface deformation of our membrane is substantially less than reported as shown in Table 15, even compared to other supported membranes. While the other glass fiber membrane had a much higher deformation, Pan *et al.* were using a different polymer electrolyte, with a deformation coefficient greater than Nafion. The surface deformation of our membrane is substantially better than PTFE based composites. Although PTFE supports the Nafion and reduces swelling, PTFE is much more malleable than glass. As internal forces stress the membrane, deformation will occur at a slower rate than in bulk Nafion. Because of the glass-like properties at low to moderate stresses in our membrane, lateral deformation is very low. Because the substrate membranes are a mixed mat-weave, they are not as strong along the vertical axis, allowing the membrane to thicken when hydrated, changing the volume. However, with respect to our requirements, changes in thickness are not a serious issue.

The rigidity of the glass fiber support lends itself to a much more stable membrane. However, the surface area deformation was very low, varying between 0.5 and 1% for our

supported membranes. Given that the surface area deformation is less than 1%, we can treat the membrane as a stable substrate for low-cost deposition based fuel cell manufacturing.

3.3.8 Summary

We have demonstrated a new composite membrane based on glass fiber supported Nafion. Ionic conductivity was reduced with the volume fraction of the Nafion; however, all the mechanical characteristics were improved. In particular, the membrane resisted deformation from both external applied loads and from water content cycling. The stability of the membrane at low strains makes it particularly suited for reel-to-reel manufacturing techniques because it will not deform under stress or handling. The stability of the surface area under water cycling makes this membrane a candidate for a sequentially printed, compressionless fuel cell.

3.4 GDL Ink Preparation

The GDL must have the following characteristics: electrochemically compatible with a fuel cell operating environment; have a conductivity of at least 50 kS/m; and a porosity of 50%. In carbon paper and porous silicon systems, the GDL is a solid and is difficult to deposit through a stencil. A more appropriate GDL formulation is a particle-based conductor held together with a polymer binder, similar to a fuel cell catalyst layer or silver epoxy paints.

Porous conducting particulate media can be composed of many different materials possessing a wide variety of particle morphologies. Members of the research team at NRC devoted a significant effort into the empirical investigation of the role of particle type, morphology and relative concentration on the conductivity and porosity of the composite. This thesis is not concerned with the research process used to achieve this material because the

author was not the primary researcher in that effort. The final composition is presented here, and its application described in later sections. The final composition is relevant to the overall performance of this system.

For the anode, a modified version of the standard silver based particle conductors can be used as the GDL. The addition of carbon particles and rods for additional porosity, and substitution of a flexible chemically inert binder for the standard epoxy based binder, can alter a silver based conductor to make a suitable GDL. Unfortunately, only costly noble metals and carbon have sufficient conductivity and resistance to electrochemical corrosion.

The final GDL formulation is composite of carbon fibers, carbon particles, silver particles, and a binder. The carbon fibers are 250 μm long graphite rods, 12 μm diameter. The carbon particles are XC-72A from Cabot Materials. The silver particles are 5 μm diameter pure silver from Alfa Aesar. The binder is SEBS (Polystyrene-block-(polyethylene-ran-butylene)-block-polystyrene). Table 16 shows the relative mass ratios of the components.

Table 16:Component ratios for castable anode GDL

Component	Mass Ratio (%)
Silver Particles	49
Silver Flakes	13
Carbon Rods	12
XC-72A	2
SEBS	24

The above formulation is appropriate for the anode of the fuel cell. However, silver will corrode under fuel cell operating conditions on the cathode, and interfere with the oxygen reduction reaction at the cathode, significantly reducing the current available for electrical work. Most non-noble metals corrode under fuel cell cathode conditions. To prototype our

fuel cell, we substituted conducting grade graphite particles for silver particles and flakes. Table 17 shows the cathode formulation for the cathode.

Table 17:Component ratios for a castable cathode GDL

Component	Mass Ratio (%)
Carbon Rods	55
XC-72A	7.5
SEBS	37.5

The formulation for the cathode GDL was determined by substituting the silver on a volume basis by multiplying the mass required for the anode silver loading by the ratios of the density of silver and graphite. The conductivity of the graphite based GDL should be less than the silver based system by the ratio of the conductivities. The fabrication method for both the carbon and silver based GDLs were identical.

The particle components are mixed in their dry form and the SEBS is dissolved and diluted in toluene. Casting, the current method of deposition, requires that the solids be a significant proportion of the total mass loading. The suspension should be the consistency of wet sand; this implies a toluene mass ratio of approximately 1:1.

3.4.1 Characterization of Castable GDL

According to the requirements for the material, three key physical parameters for the GDL were required: electrical conductivity, porosity, and electrochemical compatibility. The conductivity was characterized using a four-point probe method. Porosity was confirmed by measuring the volume and mass. Electrochemical compatibility was tested using cyclic voltametry.

3.4.1.1 Conductivity

Electrical conductivity is usually measured with a four-point probe, where the sensing electrodes are separated from the current probing electrodes, reducing the error. A four-point substrate was prepared by etching traces in a printed circuit board. The GDL was deposited across the electrodes through a stencil 2 cm wide and 3 cm long. The substrate had traces at 5 mm spacing that were, 2.5 mm wide. The working length for the measurement, is therefore, 0.5 mm. Thickness of the film was estimated from measurements in ten locations using a micrometer calibrated on a Zeiss microscope at 500x magnification. The conductivity values for the carbon and silver based GDLs are shown in Table 18.

Table 18: GDL conductivities

GDL Primary Composition	Typical Conductivity (S/cm)
Carbon (cathode)	18 S/cm
Silver (anode)	1065 S/cm

Using this technique, a conductivity of 1065 S/cm was measured which is double the conductivity required by the calculations and simulations in chapter 2. However, the cathode GDL conductivity is significantly less than the requirements as outlined in chapter 2. The lower than expected conductivity was primarily due to the substitution of carbon for silver. Although carbon is chemically compatible with cathode electrochemistry, it is not sufficiently conductive for power generation. The low conductivity of the cathode GDL could dominate the performance of the micro fuel cell.

3.4.1.2 Porosity

Porosity is usually measured using a mercury porosimeter, which forces mercury through a sample and records the change in pressure. However, measurements on our GDL have proven

unreliable because the GDL material itself is flexible. During the measurement, the pore structure deforms, making the results difficult to interpret.

Instead of using the more precise direct measurement technique, the porosity can be estimated from the density of the solid content of the GDL and its total volume. This calculation is based on the assumption that the solid phase components and binder are distributed homogeneously throughout the GDL. Based on these calculations, the porosity was expected to be approximately 0.61 for both formulations. The basic assumption underlying this calculation should hold for a large surface area. To verify the approximation, we have examined SEM images of the GDL to determine if the distribution is approximately constant. An example of the structure is shown in Figure 51.

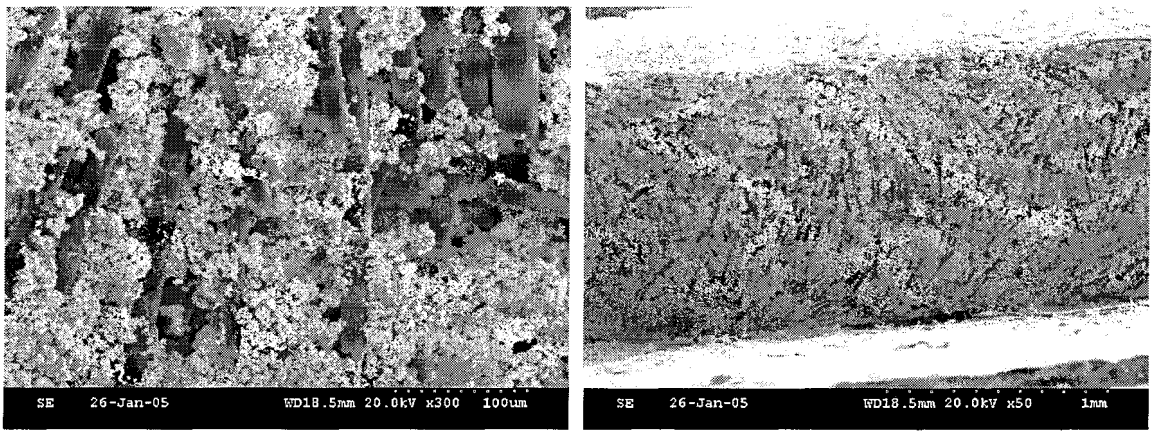

Figure 51: SEM images of castable GDL

The SEM image on the left in Figure 51 is a top view of the anode GDL. The SEM image on left in Figure 51 is a cross-section of the anode GDL. Both large and small pores are visible in both images. In particular the top view shows pockets that are between 20 and 50 μm in diameter and smaller pores between the individual silver particles.

3.4.2 Summary

Working with other researchers, we have created a castable GDL with a conductivity of 1068 S/cm for the anode, and 18 S/cm for the cathode. For the anode side, these parameters more than meet the requirements calculated in the theoretical analysis in chapter 2. However, the cathode side underperforms, leading excessive Ohmic losses. As an additional benefit, the GDL is flexible. While the flexibility makes direct measurement of the porosity difficult, it adds an additional degree of mechanical robustness to the fuel cell design.

3.5 Catalyst Ink Preparation

The catalyst ink was prepared using standard methods. A 20 wt% platinum on XC-72A carbon from E-Tek was used as the solid phase of the ink. Butyl-Acetate was added to the carbon to form a slurry. In a separate beaker, a colloidal Nafion solution was formed. A 5% Nafion solution in water and alcohols, from Alfa-Aeser, was mixed with isopropyl alcohol at a 1:1.5 ratio, then drop-wise butyl acetate at a total ratio of approximately 1:1. Once the Nafion-isopropyl alcohol-butyl acetate solution changed from clear to light blue, the colloidal form had been achieved. The carbon-platinum-butyl acetate suspension and the Nafion colloidal solution were then combined in a high-speed mixer for 15 minutes. The resulting suspension was applied to the substrate through a stencil.

3.6 Electrode Fabrication

The electrode is the combination of the all the solid phase electrical conductors including: the catalyst, GDL and thin-film current collector layers. The inks were prepared as stated in the previous section and deposited through stencil prepared using photolithography techniques, explained in the following sections.

3.6.1 Electrode Patterning Technique

There are several possible methods to pattern the catalyst, GDL, and gold layers of the electrode structures. Gold thin films can be etched in iodine or aqua regia based systems. While theoretically possible to use photolithography to pattern thin films on a dimensionally stable ionomer substrate, the chemical etchants, and organic solvents used in photolithography can be absorbed by the ionomer, degrading its performance. Iodine-based etchants are selective for gold over the other constituents of the fuel cell. Aqua regia will etch platinum slower than gold, and could theoretically be employed to selectively pattern the gold current collector in the presence of platinum catalyst. However, given that nanoparticulate platinum is used in fuel cells, any platinum etchant could destroy the catalytic activity. While our membranes are significantly more stable than bulk Nafion under water content cycling, they are not stable when exposed to other organic solvents such as acetone. Most common photoresist materials require an acetone rinse to completely remove the photoresist after processing. Directly patterning gold electrodes in an inside-out fuel cell is almost possible, but a new photoresist material with an alcohol based stripping solvent would be required. Using existing patterning technology, a dry, stencil-based approach is superior to a deposit and etch system, despite the loss of resolution in stencil-based systems.

3.6.2 Stencil Fabrication

We fabricated stencils from 50 μm thick carbon steel shims (Lyon Industries). Carbon steel allows the use of a magnetic chuck to keep the stencil attached to the substrate during depositions. Stainless steel and other metals were insufficiently ferromagnetic to maintain a sufficient level of adhesion between the mask and substrate. Masks corresponding to the catalyst, GDL and current collector layers were designed in AutoCAD and exported as

PostScript files for direct acetate film printing. Duplicate films were created with symmetry about the y-axis. Designs used for the experiments in chapter 4 are shown Figure 52 (not to scale).

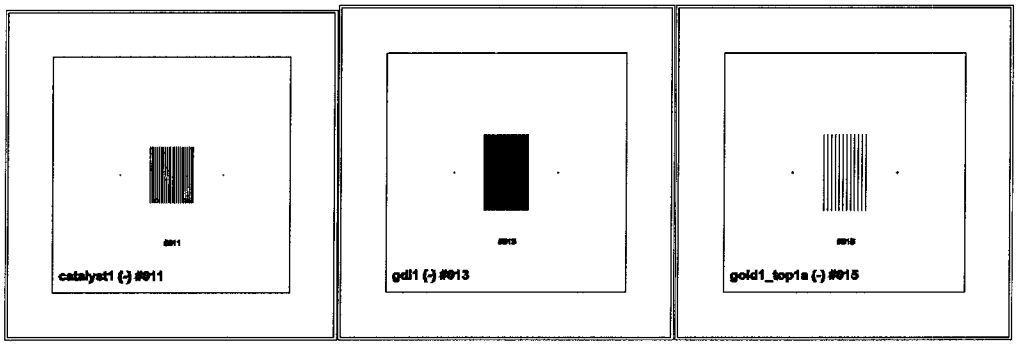

Figure 52:Stencil masks for catalyst (left), GDL (centre) and thin film (right)

A series of electrodes 2mm wide and 2 cm in length were used for the electrodes. A set of strip cells could be wired in series or parallel depending on the requirements of the system. Based on our analysis in chapter 1, a system providing 4 V and 25 mA would be sufficient for most applications. For a DMFC operating at 0.35 V, twelve electrodes are required. With an electrode area of 0.4 cm^2, each electrode would need to produce 62.5 mA/cm^2, a reasonable operating point for a DMFC from the literature.

The films were aligned under a microscope and attached with tape on one edge, to form a hinge. The metal foil was coated with photoresist (Shipley) on both sides and soft baked for 20 minutes. Both sides of the film were exposed under UV light for 30 s, developed then baked for an additional 20 minutes. After developing, the steel films were etched in $FeCl_3$ (aq) until the pattern was clear.

Because steel etchants are isotropic, significant overetching occurred. Theoretically, the over etch should be twice the substrate thickness for a single sided etch, or equal to the

thickness of the substrate for simultaneous etch from both sides. However, significant additional etching was required to completely clear the masks, resulting in additional lateral etching. The lateral etch is exacerbated by the additional etching time required. In practice, we found that an overetch of 2.5 times the thickness resulted from the additional etching time required.

For the catalyst and GDL layers, which are 2mm wide, the overetch adds an additional 12% of width, easily compensated by reducing the size of the features in the masks. However, the gold traces should be narrow to maximize mass transport. Based on a minimum feature size of 25 μm from the acetate printing process, the minimum feature size for a stencil is 150 μm. Based on our analysis, 200 μm traces with 300 μm spacing is sufficient for diffusive mass transport at 50 mA/cm^2.

3.6.3 Catalyst Deposition

Deposition of the catalyst on the dimensionally stable membrane was accomplished through spray deposition. The membrane was placed on a magnetic chuck separated from the membrane with a layer of Parafilm (Alfa Aeser). The ferromagnetic mask performs the dual role of holding the substrate in place and providing a stencil for deposition. A diagram showing the assembly is shown in Figure 53.

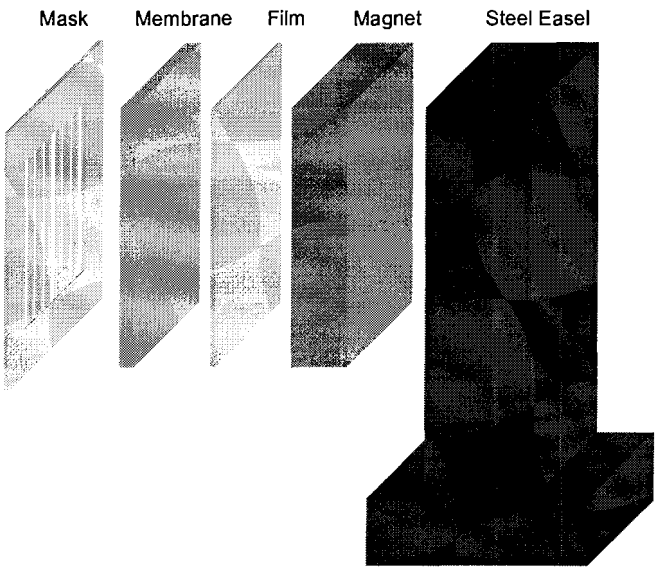

Figure 53: Magnetic chuck assembly for catalyst deposition

Once the mask and membrane were secured to the magnetic chuck, the entire assembly was placed against a steel easel for spraying. The catalyst ink was added to a spray gun and applied to the substrate. Spray was applied for two seconds, then left to dry for ten seconds. The drying time allowed most of the solvent to evaporate, preventing the catalyst ink on the surface of the membrane from running. After 20 repetitions, the membrane was turned-over, and front-back aligned on a light table with the stencil to the magnetic chuck assembly and the process repeated on the opposite side.

3.6.4 GDL Deposition

The GDL mixtures were prepared according to the formulation described in section 3.5 just prior to application. A variant of the magnetic chuck was used to attach the stencil to the catalyzed membrane. The GDL material was then poured onto the assembly and trowelled off using a glass slide, resulting in a layer of GDL material with the same thickness as the stencil. A diagram of the process is shown in Figure 54.

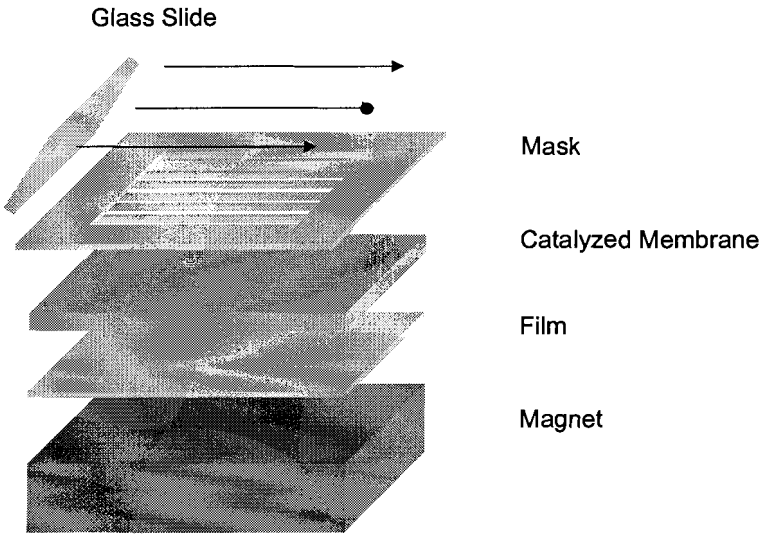

Figure 54:Application of GDL through stencil

Following the GDL application, the MEA was dried at 80 C for two hours to drive-off the solvent. The process was then repeated on the opposite face, and the membrane was dried at 80 C overnight to ensure no solvent remained trapped in any of the micro pores.

3.6.5 Gold Deposition

The gold layers are deposited to provide highly conductive paths for bulk current collection. Current must travel horizontally across the catalyst layer to reach the gold layer, where it was routed through the trace to the edge of the MEA. By depositing the bulk current collector directly on the MEA, we are able to build the flow fields from an insulating material, and neglect the requirements for compressive sealing and current collection.

The gold was sputter deposited through a stencil prepared in the same manner as the catalyst stencil. The stencils were aligned by hand under a microscope and transferred to a magnetic chuck prior to sputtering. A 250 nm thick layer of gold was deposited using sputtering. Two masks were patterned: the first mask provides the bulk current collection for

the electrodes, while he second mask patterned the electrode terminals for either series or parallel connection.

For a parallel connection, a single pad is located at the top and bottom of the electrodes. For series connections, offset pads, top and bottom are sputtered providing a method of wiring the fuel cell in series by shorting the pads through the substrate. In an integrated system, the current collectors would be directly attached to the power conditioning circuitry.

3.7 Channel Preparation and Assembly

Our flow fields can be made from an insulating material because bulk current collection was performed on the MEA. The channels were formed using a replica molding technique. The molds were fabricated from photo-patternable epoxy (SU-8 2100 from MicroChem Corp.) on silicon.

The SU-8 was spun on a silicon wafer or glass plate at ~700 rpm for 30 seconds. The film was allowed to relax for approximately five minutes then soft baked at 100 C for approximately 2 hours. Three consecutive times, the film was exposed to UV light for 45 seconds through an emulsion mask with the flow channel pattern and hard baked at 100 C for 15 minutes. The film was developed in SU-8 developer (MicroChem) at room temperature for approximately 1 hour with occasional gentle agitation, provided by hand. The developed SU-8 film was then passivated and silanized according to Schueller *et al.* [97].

The flow fields were cast directly onto the mold using Dow Corning Sylgard 182 polydimethylsiloxane (PDMS). The catalyst and compound were mixed according to the manufacturer's recommended process, using a 10 to 1 ratio. The mixture was sonicated for 3 minutes after mixing to remove bubbles. The mixture was poured over the mold

approximately 1 mm deep on a clean level surface. After the cast polymer relaxes, the mold and polymer were placed in a vacuum oven a room temperature and 30 inches-Hg pressure to remove bubbles before the silicone cures. After 2 hours under vacuum, the PDMS was cured at 110 C for 90 minutes. The cured flow fields can be removed from the mold by hand and the excess rubber cut away with a scalpel.

RTV silicone, a standard rubber adhesive, was used to seal the flow fields to the membrane. The adhesive can be painted directly onto the flow fields, or it can be spread in a thin layer on a flat substrate, and flow fields rolled over the film like a stamp. Once the adhesive was applied, the flow fields were affixed on the membrane by applying modest pressure and allowing the silicone adhesive to dry overnight.

3.8 Discussion

The fabrication technique described in this chapter is not the only micro fuel cell architecture proposed. Many other researchers have created micro fuel cells and micro fuel cell fabrication techniques. However, our design is the only design built on a full analysis of the unique characteristics of micro fuel cells, including manufacturing method, predicted performance, and mechanical properties. Our fuel cell is one of two inside-out fuel cell designs in the literature.

There are significant differences between our fuel cell and the inside-out design proposed by Shah *et al.* [18] exist. Their aim was to create a fuel cell using only MEMS processes. To do so, they used a thin film catalyst instead of a standard particle based catalyst and employed bulk Nafion. As we have shown, bulk Nafion is not a practical solution for inside-out fuel cells because deposited films cannot survive the rehydration cycle. The following key distinctions differentiate our fuel cell from the architecture described by Shah *et al.* [18].

1. *Precedence* The filing date of our patent predates the submission date of Shah's paper, which indicates we were the first to propose this architecture.

2. *Substrate* The hydration state of Shah's cell cannot change without the thin film electrodes and catalyst delaminating. While his results are reasonable for a short-term test, the performance of their fuel cell would rapidly degrade.

3. *Mask structure* By using ferromagnetic masks and a magnetic chuck we can ensure that stencil is flush with the substrate, permitting the use of solvent based layers. Although the PDMS stencils used by Shah are effective for masking sputter depositions, they are not sufficient for reliable patterning of liquid media.

4. *Electrode structure* The most pronounced difference between the design in [18] and ours is the electrode structure. We employ a thick and thin film structure as described in this chapter. Shah *et al.* use a two-layer grid structure. Within the outer gold grid, a tighter thin film platinum grid provides the three-phase interface. This thin film approach wastes electrolyte surface area. Using a three-layer approach with a standard catalyst layer we can achieve much higher catalyst efficiency and better surface utilization.

5. *Approach* Attempting to build an all silicon-MEMS micro fuel cell is prohibitively expensive manufacturing perspective. By pursuing a thorough analysis and a hybrid fabrication approach, we can overcome these cost shortcomings.

Although many other researchers have done excellent research, our design is the first inside-out architecture, which could lead to a mass production friendly process, based upon

sound design principles. Our fuel cell design is flexible, conformable, and mechanically robust. The inside-out architecture itself is not inherently flexible; however, the traditional plate and frame approach architecture is inherently not. While conceivable that an outside-in fuel cell could be made flexible, the inside-out is the most likely candidate because it is built on a flexible substrate. The thin gold film and particle based catalyst layer are flexible, but the flow fields and GDL are not inherently flexible. By selecting a particle based GDL with a flexible binder, and a flexible polymer flow field the entire system can be made flexible. This flexibility has advantages in applications that requires a conformable power source, or applications where mechanical reliability is required because the fuel cell is shock resistant.

3.9 Summary

By merging the specific numerical material requirements from chapter 2 with our analysis of manufacturing requirements, we have designed a unique fuel cell and fabrication technique, which provides a reasonable solution for the volume manufacturing and mechanical characteristics of micro fuel cells. New membrane and GDL materials were required to realize this design. A glass fiber supported membrane was created and analyzed, and found to provide acceptable mechanical and chemical performance. A particle-based castable anode GDL was created which met the conductivity and porosity requirements outlined by theory. To create the inside-out design, a stencil-based technique employing steel stencils and magnetic chucks was created. Catalyst, GDL and current collectors are sequentially deposited through stencils to form an MEA. Flow fields created with soft lithography were adhered to the stencil based MEA to create the fuel cell. We achieved a conformable micro fuel cell using hybrid traditional and micro fabrication techniques.

Chapter 4 Results and Characterization

4.1 Introduction

In chapter 3, we presented the fabrication process. This chapter contains a description of the fuel cells produced using the process in Figure 38. Qualitative and quantitative results for each step of the fuel cell components created in the fabrication process are provided as well as results for the fuel cells operating with both passive and active flow over the cathodes.

Fuel cell performance is characterized by its power output and efficiency. Fuel cells are in turn described by their power density and their performance losses within particular operating regimes. By identifying the primary loss regimes for a given fuel cell materials, architecture and fabrication processes can be redesigned to address shortcomings of the individual components. As initially outlined in chapter 1, fuel cell performance is usually characterized by three loss regimes: kinetic, Ohmic and mass transport.

Kinetic losses are electrochemical in origin, stemming from the activity of the catalyst employed in the fuel cell. Better catalysts yield lower potential drops due to smaller activation losses. However, the catalyst material is not the only consideration. The total available catalyst area has a significant impact on the overall kinetics of the fuel cell. Ohmic losses occur direct current flow in conductors. Maximizing the conductivity of the solid and liquid phases of the cell minimizes such Ohmic loss. Mass transport losses are due to by deficiencies in reactants at the catalyst sites, reducing the reaction efficiency. This shortfall can be caused by a scarcity of reactants or an overabundance of products obscuring the catalyst.

Fuel cell testing and characterization is a challenging task. Because fuel cells are complex, coupled systems, it is difficult to separate the causes of different performance degradation

effects. In this chapter, we present the performance of several fuel cell prototypes and analyze the performance to determine the causes of the departure from ideal. From these results we provide recommendations on the key aspects of the fuel cell design and material properties, which must be addressed in subsequent fuel cell designs.

4.2 Fabrication

Although the design considerations and fabrication principles have been discussed in the preceding chapters, the fabrication process is still in the research stage. Changes in material properties and the final architecture occurred because the lab scale manufacturing process led to substantial variation in pattern geometry and material parameters. The fabrication results are discussed in 4.2.2, detailing the properties of the fuel cells fabricated.

4.2.1 Performance Degradation Mechanisms from Fabrication

When evaluating fuel cell materials, fabrication processes, and architectures, we must distinguish between the potential performance of an architecture with a given set of materials and processes as presented in chapter 2 and the actual performance after irregularities in the fabrication techniques are taken into account.

4.2.1.1 Membrane Impact

The primary failure mode for the membrane fabrication was the introduction of pinholes during fabrication. Pinholes result in small leaks, allowing the fuel and oxidant to interact, causing a mixed potential, decreasing the open circuit voltage, as well as reducing the available catalytic surface area.

To reduce the impact of pinholes, membranes were screened using the testing apparatus described in chapter 3. Although this step ensured that membranes with high pinhole density

were disqualified from further processing, it could not completely eliminate potential losses. Some potential drop due to crossover will always exist. Fuel cells are routinely fabricated using Nafion 112, which has a leak rate of less than 10 μl/min, providing a useful floor for the impact of crossover on the overall fuel cell performance. All fuel cells tested used membranes with a crossover rate comparable to bulk Nafion 112. .

The second membrane based fuel cell performance degradation mechanism is the Ohmic resistance to proton transport across the membrane. Membrane resistance is usually described as a conductivity, which then must be matched with the membrane thickness, electrode dimension and current density to determine the potential drop. The fabrication process for used to make our membranes yielded stable membrane conductivities, based on theory and impedance tests as described in section 3.3.4. Even without specifically testing the membrane conductivity, which requires removing a portion of the active membrane area, we expect that the membrane conductivity lies between 30 and 40 mS/cm.

Because our membrane process is one of the most mature fabrication steps, the material properties were stable enough that the membrane should not have any unforeseen impact on the performance of the fuel cell. We expected an open circuit voltage between 0.85 and 0.95 V with hydrogen as a fuel and a passive air-breathing cathode.

4.2.1.2 Catalyst Impact

Because we used a proven fabrication process for catalyst layer deposition, the catalyst layer was expected to have little impact on the performance of the fuel cell system. The general catalyst morphology is not optimized; however, compared to the repeatability of the membrane preparation, GDL formulation, and deposition and patterning, the catalyst mature.

The only potential shortcoming with the catalyst layer is controlling its thickness. In traditional fuel cell manufacturing techniques, the catalyst layer is deposited on a carbon paper GDL. The platinum loading can be verified by driving off the solvent and weighing the electrode. The change in the electrode mass corresponds to the weight of the catalyst layer. If the loading is insufficient, additional catalyst can be deposited. For a catalyst-on-membrane system, solvent drive off also drives water from the membrane; therefore the change in mass no longer corresponds to the catalyst loading. Allowing the membrane to equalize with the ambient humidity overnight removes some uncertainty, but Nafion is strongly hygroscopic; therefore, changes in the relative humidity obscure the final net mass. Industrial scale production could overcome these shortcomings by careful calibration and control of the deposition rate through the nozzle; however we do posses the required equipment in our laboratory.

As an alternative method of measuring catalyst loading after deposition, we measured the thickness of the layer using a Zeiss microscope micrometer. Our target was a 20 μm thick layer as described in chapter 2. The micrometer has an accuracy of ± 2 μm per measurement, or a total accuracy of ± 4 μm for a depth measurement. Because both the membrane substrate and catalyst layer exhibit local thickness variations, the depth is difficult to measure. Several measurements over a large area are required to estimate the catalyst layer thickness. We estimate that our catalyst layers are, on average, between 10 and 30 μm thick. We are reasonably certain that all the electrodes are within this band, but local thickness variation is significant. The variation in thickness makes estimation of loading difficult.

4.2.1.3 GDL Impact

The GDL formulation and processes have not matured to the same degree as the other processes; therefore, the GDL parameters vary the most during fabrication. Because GDL development is in the early stage of research, significant variations in the material properties of the cast GDL exist.

The two key material properties of the GDL are the conductivity and porosity, which are linked. The greater the porosity, the lower the conductivity and vice-versa for a given GDL composition. Changes in GDL properties can be caused by the micro-morphology of the composite. The ideal material has significant local changes in density, providing clear open paths for both the electrical and gas phases. Optimization of this structure is similar to the optimization of the catalyst layer microstructure and is a thesis topic on its own. We have not optimized the composition of the GDL; instead we have attempted to estimate its impact by measuring the material properties *in situ*. We do not have the ability to measure the GDL porosity after deposition, but we can measure its conductivity.

Although we do not have sufficient control over the GDL process to ensure consistent properties, we have attempted to control for losses due to GDL fabrication, by testing the total conductivity of the system after GDL and gold deposition. We cannot correct the conductivity after measurement, but it provides a baseline for the estimation of Ohmic losses described in chapter 2.

4.2.1.4 Patterning Impact

Because the patterning is performed using a series of stencil-based depositions, the biggest fabrication shortcoming is over-spray or leakage of the depositing medium beyond the edge of

the stenciled pattern. This problem could be exacerbated by poorly designed or fabricated stencils, as an overetched stencil would decrease the margin for error due to overspray.

The gold deposition occurs in a dry environment, therefore gold overspray is caused by the shape of the stencil, and the quality of contact between stencil and the substrate, not local deformations of the membrane due to local changes in hydration state. Because we compensated for the stencil overetch during the design process, the stencil itself does not substantially contribute to the patterning error. The stencil was attached to the substrate using a magnet, which provides a reasonably consistent adhesion between substrate and stencil across the stencil surface; this method minimizes the overspray due to a poor stencil substrate interface. Any significant errors in the gold deposition are due to the alignment of the gold stencil to the preceding layers. Because the stencil is aligned under a microscope, precise alignment is possible if handling the stencil-substrate-jig assembly does not alter the alignment during transport between the microscope and the sputterer.

Catalyst spray deposition can have significant errors if the ink is too wet when it strikes the substrate, because it can flow under capillary force through small channels formed by irregularities in the membrane surface. To mitigate the potential for ink creep, we attempted to minimize the amount of solvent remaining by the time the spray strikes the substrate. The catalyst was spray deposited using an automotive touchup gun at 40 psi. The substrate was heated on a hotplate to 60 C, to drive off solvent after deposition. Depositions were performed in coats, with each coat lasting 5 s, and 20 s between each coat.

The GDL has the greatest potential for patterning errors. Because the long carbon rods clog the nozzle, the ink cannot be deposited by spray deposition. Instead, the GDL is deposited using a doctor-blade casting technique, which can be effective for narrow ranges of

viscosities, constituents, and solvents. The suspension must be as thick as possible to prevent creep during drying, but thin enough to spread evenly. GDL leakage causes shorting between the electrodes, forcing the fuel cell to be run in parallel.

4.2.1.5 Assembly Impact

Because the PDMS formulation used for the flow fields is transparent, the quality of the flow field can be directly observed. Bubble inclusions or other visible imperfections disqualified the flow field. Alignment was also facilitated by the transparency of the flow field. The largest hazard in fuel cell assembly was the adhesive overflow to the substrate, which blocked the pores in the GDL. To mitigate this effect, the flow fields in these trials were adhered around the edges only. The flow fields are attached to the GDL and membrane by tension in the rubber, providing a short circuit flow path in some configurations.

4.2.2 Fuel Cells Fabricated

We fabricated four fuel cells. Two of the fuel cells were tested with both passive and active cathodes, which required an additional fabrication step to attach a flow field to the cathode side. The fuel cells were created to test the impact of the two material advances we had made: the composite membrane and castable GDL. Four cells were fabricated in order to test the impact of the membrane on performance. Both carbon and silver anodes were measured to baseline the impact of the GDL composition and separate it from the membrane impact. The performance of the fuel cell with silver and carbon anodes was examined under passive and active conditions to understand the impacts of conductivity and porosity on the performance.

4.2.2.1 Fabrication Results

Several membranes were fabricated using the processes described in chapter 3. All membranes were tested in the leak testing apparatus described in chapter 3, section 3.3.6. Any membrane with a leak rate greater than 25 μl/min was removed from the process. The area of the membrane tested was recorded with a light pencil mark. The catalyst layers were deposited within the marked region to ensure that area occupied by the cell was leak free.

Pattern transfer through the stencils of the catalyst, gold, and the silver anode GDL layers was within 10% of the width of the stencil. However, the carbon only catalyst layer had a tendency to spread under the stencil. We investigated this behavior and found that the activated charcoal component of the GDL was spreading, while the rods and flakes stayed relatively intact. We suspect that the morphology of the silver flakes causes them to adhere more strongly to the XC-72 carbon than the carbon flakes, reducing the amount of XC-72 available to flow. The result was connections between electrodes on the cathode side of all cells. Consequently, we chose to wire all the cells in parallel rather than attempt to mechanically separate the electrodes post fabrication, which is technically possible, but would usually result in permanent damage to the membrane.

After gold deposition, standard wire-wrap wires were attached to the gold electrodes using the carbon GDL material. The carbon GDL material is not an ideal adhesive, however, it is known to be electrochemically inert [98], therefore, mechanical strength was sacrificed for predictable electrochemical behavior. Because the contact with the wire was poorer than with a standard silver epoxy adhesive, additional resistance was introduced, reducing the overall efficiency. In the future, a better formulation for the adhesive must be found that increases mechanical strength and decreasing contact resistance. Flow fields were attached to the

membranes using silicone adhesive. Two coats of adhesive were applied, the first to affix the membrane to the flow field and the second to ensure that no leaks were present. Images of a completely assembled fuel cell are shown in Figure 55.

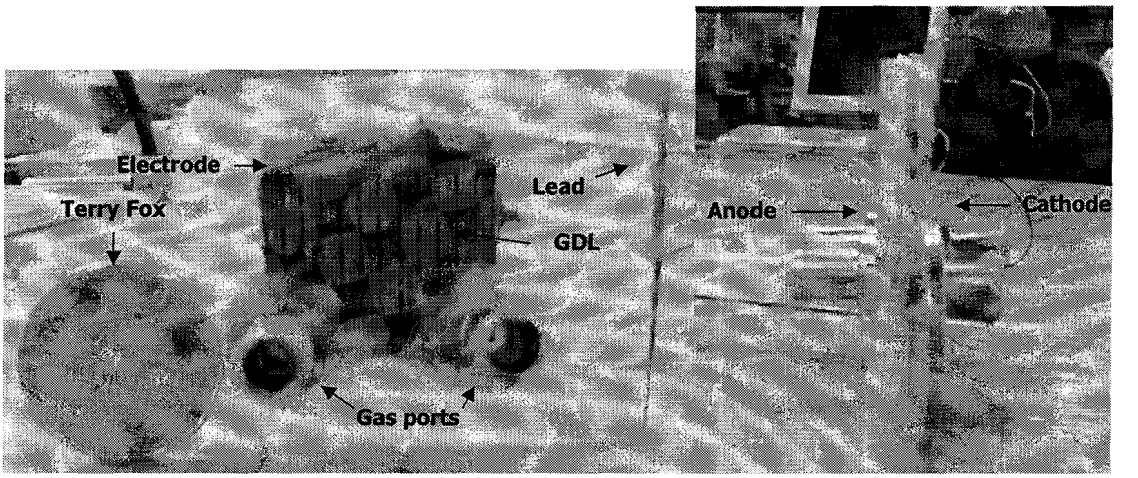

Front view Side view

Figure 55:Front and side views of the fully fabricated fuel cell

A loonie is included in Figure 55 to provide a sense of scale. The striations are the electrodes of the cell. The stainless steel nubs are the interface between the micro flow field and the test station. The cell is shown in its final configuration, with flow fields on both sides, in preparation for forced air characterization. The connecting wires can be seen extending from the right of the cell out of the picture. The connecting tubes have been removed from the cathode (front/right) of the fuel cell, to provide an unobstructed view. The quarter inch silicone tubing used to connect the cell to the test station can be seen extending from the anode (back/left) side of the elevation view. The active area is slightly larger than the loonie, and the cell is slightly thicker. An excess of silicone adhesive can be seen surrounding the cathode connection nubs, clearly illustrating that this was a lab prototype.

4.2.2.2 Electrode Resistance

The electrode resistance of each cell was measured after fabrication. The resistance across the electrodes was measured, which can be used to estimate to the edge collection losses that the cell would experience. The short circuit current was estimated from these resistances by assuming 0.7 V as the potential at the start of the Ohmic region. Table 19 summarizes the measured resistances and the expected short circuit currents. The final column indicates the ambient relative humidity would cause the fuel cell to flood at the calculated short-circuit current (SCC) and room temperature. The short circuit current corresponds to the greatest current density and therefore the greatest flux of water vapor out of the membrane. If the fuel cell is not expected to flood at the expected SSC, 100% RH is entered.

Table 19:Measured electrode resistances and expected performance based on electrode resistances

Configuration	Anode Resistance (Ω)	Cathode Resistance (Ω)	Expected SCC (A/cm^2)	Expected Minimum SCC (A/cm^2)	Flooding (% RH)
Nafion-carbon	10.5	25.8	0.0080	0.0040	100%
Nafion-silver	1.5	7.1	0.034	0.017	90%
Composite-carbon	2.5	14.5	0.017	0.0086	90%
Composite-silver	11.2	13.2	0.012	0.0060	100%

The values in Table 19are the predicted values based on the approximation we derived in equation (47) and the worst-case maximum described in equation (35). This table contains Ohmic losses only, but based on the resistance of the carbon GDLs, we expected the Ohmic losses to dominate. This calculation does not include the Ohmic losses due to the membrane, protonic and electronic losses within the catalyst layer, or the contact resistances between the GDL and catalyst layer. We expect those losses to be small with respect to the cathode losses due to edge collection. The final column in Table 19 contains the relative humidity at which

the cell would experience flooding. Our calculations indicate that little to no flooding should be observed for the cells given the high electrode impedances.

4.3 Experimental

In this section, the polarization experimental results performed on the prototypes described in the preceding sections are described. Both the polarization curve and its derivative were analyzed in an attempt to understand the behavior of the fuel cell and possible methods of improving its performance.

4.3.1 Experimental Setup

The fuel cell was tested using a Teledyne Medusa RD test station, which provided a constant and controlled humidified hydrogen gas stream at 100 mL/min and 30 C. When the gas reached the cell it had cooled to room temperature. Because the station's load bank does not have sufficient resolution at lower power densities, an external load and measurement apparatus was used, a Solatron SI 1287 potentiostat, which performed load stepping and potential and current measurements. The testing setup is diagramed in Figure 56.

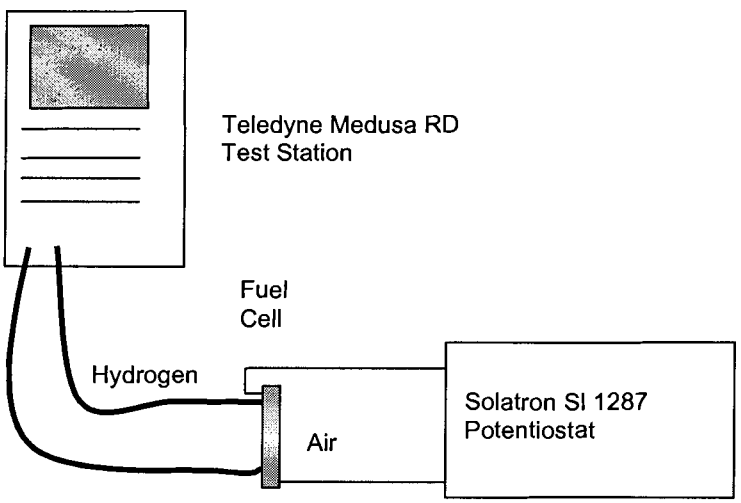

Figure 56: Experimental setup

Each cell was conditioned for 30 minutes at OCV then run through three load profiles, with ten minutes between each load profile. The cells were tested over a period of three days with an ambient temperature of 22 C and a relative humidity between 40 and 50%, and the voltage and current were recorded for each run.

4.3.2 Passive Cathodes

Most micro fuel cells are designed to operate with a passive cathode, where mass transport of reactants and products at the cathode occurs through diffusion with the ambient air. Passive operation is preferred for characterizing micro fuel cells because passive operation is indicative of actual operating conditions. Active operation can be employed to eliminate variables when characterizing the system; however, the ultimate behavior of the system is determined by its passive profile.

4.3.2.1 Nafion Membranes

We used Nafion membranes as a control condition to compare with our in-house supported membranes. Although Nafion is not mechanically stable enough for practical inside-out fuel cell design, some prototypes can hold together long enough to create a polarization curve [18]. This Nafion-based cell result provides important baseline data for the operation of the fuel cell.

4.3.2.1.1 Silver Anode

In order to reduce the impedance for edge collection to the level recommended by the analysis we performed in chapter 2, we employed a silver anode. The silver anode should reduce the losses to the extent that only the cathode losses are relevant. Two polarization runs are shown in Figure 57. The third run has been removed because the GDL and part of the

cathode layer delaminated from the membrane destroying the cell, as we predicted, between the second and third trials.

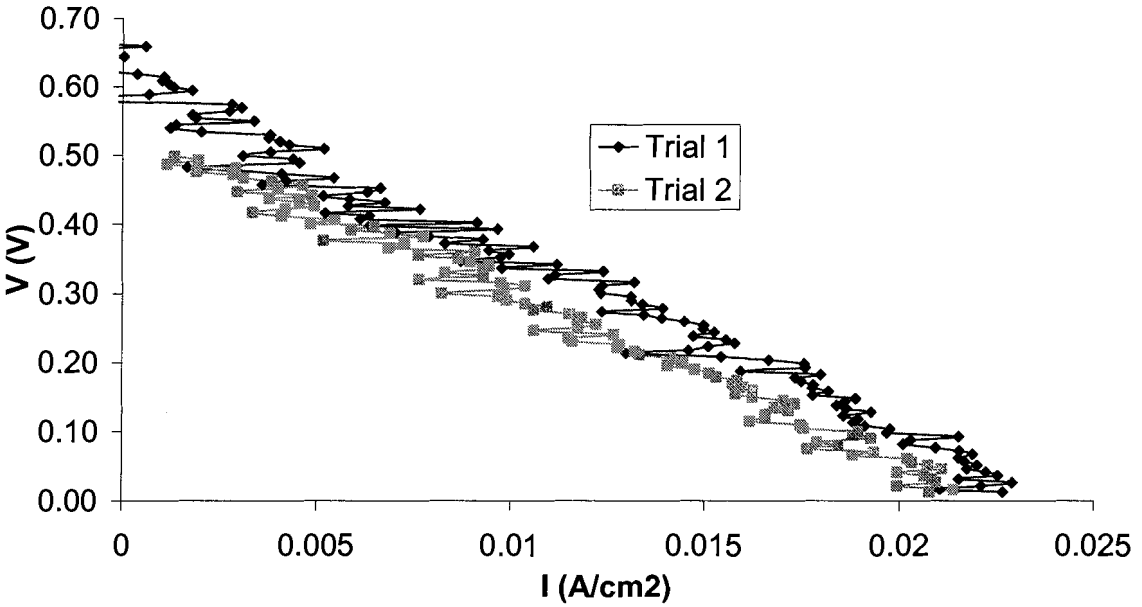

Figure 57:Silver anode bulk Nafion membrane passive cathode polarization curve

The graph has a short circuit current of between 20 and 23 mA/cm^2, although evaluating the actual value was difficult because the signal is obscured by noise. The losses were primarily Ohmic, and no flooding occurred, although it difficult to draw firm conclusions from such as noisy signal.

Several characteristics are immediately obvious from this graph. The open circuit voltage is low, which could be due to a partial delamination, silver contamination on the cathode, leaks through the seal with the membrane, or as a side effect of the noise. This level of noise is unusual for a polarization signal. In fact, the noise is a property of the system rather than random noise introduced by the test station or potentiostat. Several effects can generate noise of this magnitude. The most common cause is flooding, but the noise occurs throughout the signal, instead of only at higher current densities. Contamination or transport of silver to the

cathode could cause an unstable mixed potential, which might cause this degree of fluctuation and explain the low OCV. A pinhole in the membrane introduced during processing could also cause this kind of response, reducing the open circuit potential, and consuming some active area, changing the amount of catalyst available from sample to sample. The delamination could have caused the noise if sections of catalyst layer were moving in and out of protonic contact with the membrane during the test. However, it is difficult to conclude from the available data what causes the noise in the signal.

Significant degradation is evident from the first data set to the second, which was likely caused by the slow delamination of the GDL from the rest of the cell. This mechanism was the most likely explanation because the cell completely delaminated after the second test. The power curves corresponding to the polarization curves in Figure 57 are shown in Figure 58.

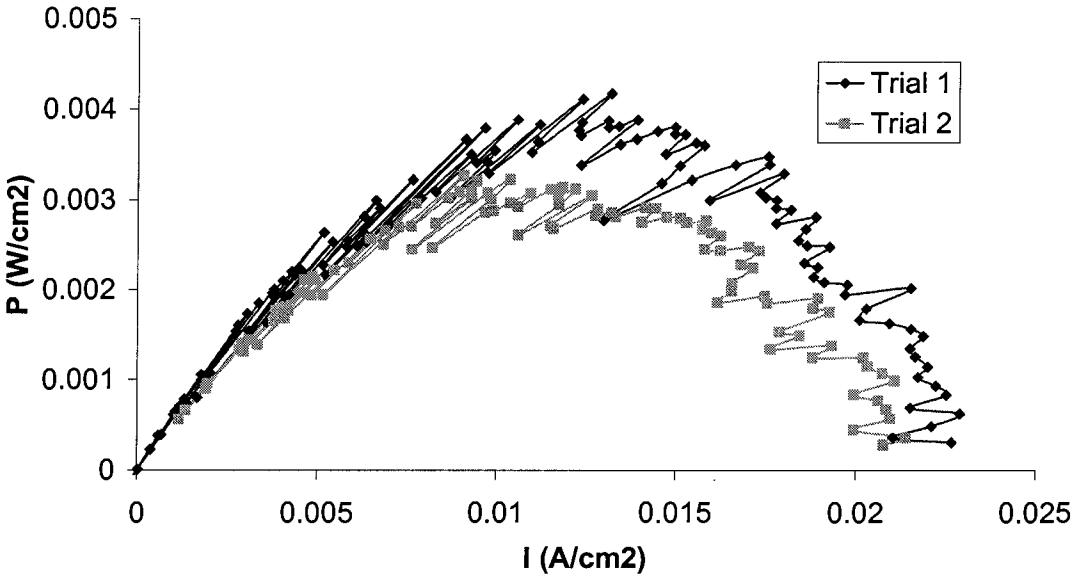

Figure 58:Silver anode bulk Nafion membrane passive cathode power curve

A peak power of over 4 mW/cm^2 was achieved. Although this is much lower than we had hoped for, it is consistent with the low conductivity of the cathode. The noise in the power curves is consistent with the noise in the polarization curves.

4.3.2.1.2 Carbon Anode

The carbon anode was introduced as a control for the silver anode, which had a much higher conductivity, but the possibility of electrochemical contamination. We expected the carbon anode to exhibit poorer performance than the silver electrode because of the much lower conductivity of the carbon anode. A direct comparison between silver and carbon for the Nafion case is difficult to determine because of the uncertain degradation experienced by the GDL during the delamination process. The polarization curves for the Nafion membrane carbon anode fuel cell are shown in Figure 59.

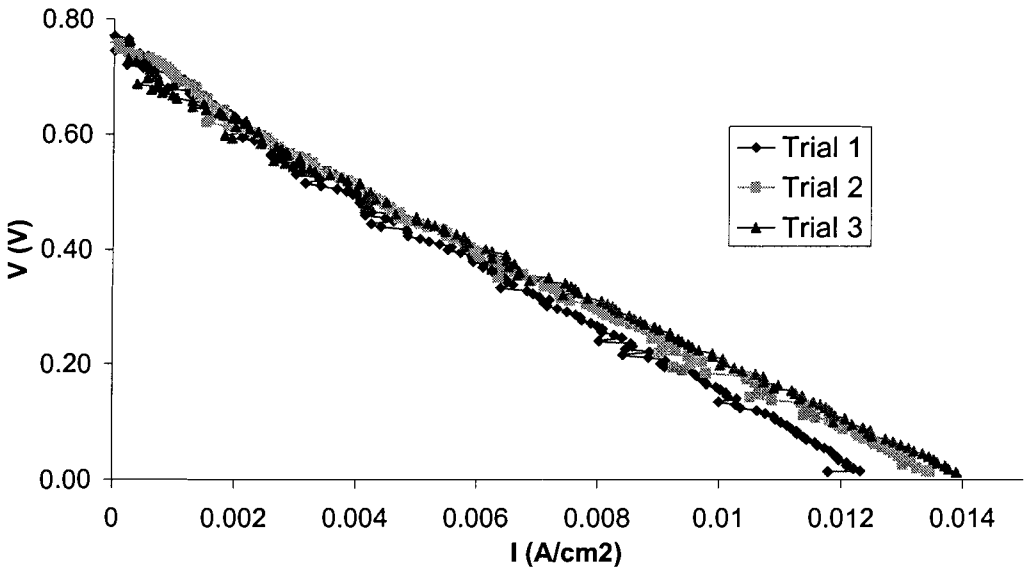

Figure 59:Carbon anode bulk Nafion membrane passive cathode polarization curve

The fuel cell exhibits a higher Ohmic loss than the silver anode case, but not as significant as predicted. The short circuit current is between 12 and 14 mA/cm^2, again low, but

reasonable. The fuel cell did not exhibit significant flooding, as expected, this is apparent from the generally linear profile of the polarization curve; there were no higher order losses at high current densities. This curve is significantly less noisy than the previous curve. While some noise is present, it is much less pronounced than in the previous curve. Superficially, the difference is the presence of silver at the anode, which implies that there is intermittent transport of silver across the Nafion to the cathode, which oxidizes and decreases the available current. Some degradation can be seen between the first two and the final curves. While sitting on a lab bench overnight after the tests were completed, the cell delaminated. We hypothesize that the dimensional change due to drying caused the delamination. The power curves for the carbon anode Nafion cell are shown in Figure 60.

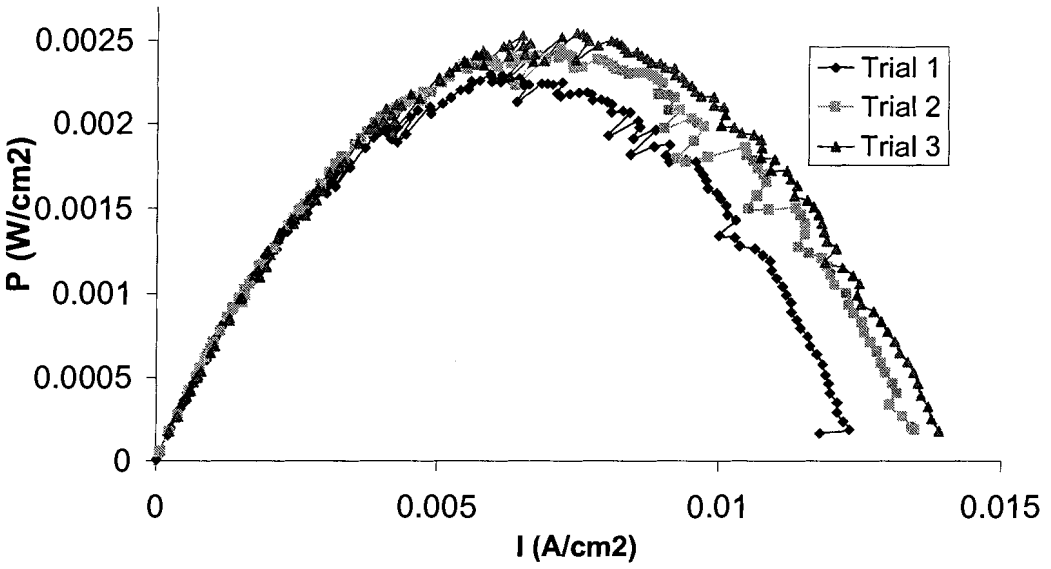

Figure 60:Carbon anode bulk Nafion membrane passive cathode power curves

A maximum power of approximately 2.5 mW/cm^2 was achieved, with reasonable repeatability. We suspect the final curve is highest because the membrane is better hydrated because of the previous tests producing water at the cathode. As expected, the power is lower than the silver anode. The curves are significantly less noisy than the silver anode Nafion

membrane configuration, but noise is still present in the signal. The two Nafion trials provided a control for the composite systems.

4.3.2.2 Composite Membranes

We created composite membranes to stabilize the Nafion and prevent the delamination observed in both of the Nafion-117 fuel cells tested in the previous section. Although the conductivity of the membranes is approximately half of the conductivity of Nafion, the impedance of the cathode is significantly higher than the impedance of the membrane and should therefore dominate the losses.

4.3.2.2.1 Silver Anode

Because the cathode in the composite membrane, silver anode fuel cell configuration is particularly non-conductive, the performance of the cell is expected to be poor, and entirely dominated by the carbon anode. The polarization curve for the silver anode, composite membrane cell is shown in Figure 61.

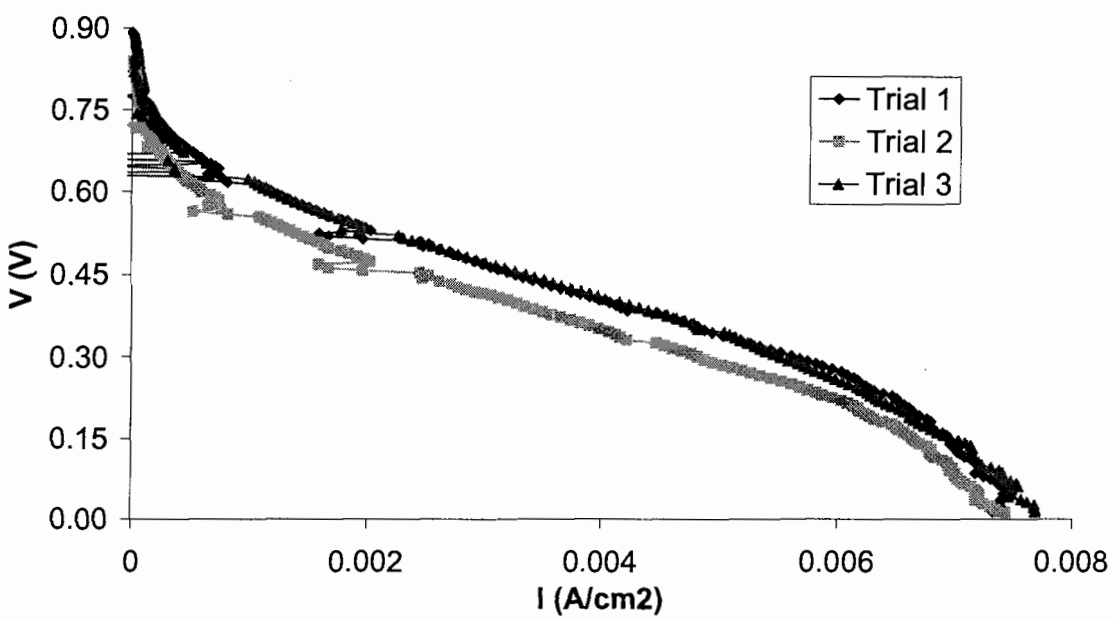

Figure 61:Silver anode composite membrane passive cathode polarization curves

The curve reaches a short circuit current of between 7 and 8 mA/cm^2. This performance is particularly poor, but reasonably repeatable; therefore it cannot be dismissed as anomalous. The OCV is more respectable, lying between 0.8 and 0.9 V for all the trials. The respectable OCV indicates a well-sealed cell with a low-crossover and stable membrane. Perhaps the most striking characteristics of these curves are the obvious roll-off above 6.5 mA/cm^2 indicative of flooding; however, flooding is unexpected below 100 mA/cm^2. This flooding at extremely low current is startling, but consistent across all three curves. There are two probable explanations: the composite membrane has unorthodox transient water properties; or the actual porosity of the GDL in this particular instance is much smaller than calculated. Because neither of the Nafion cells experienced flooding, we can surmise that the GDL is not generally of low porosity, but we cannot neglect the probable variation in GDL quality from sample to sample. The power curves for the silver anode on composite membrane cell are shown in Figure 62.

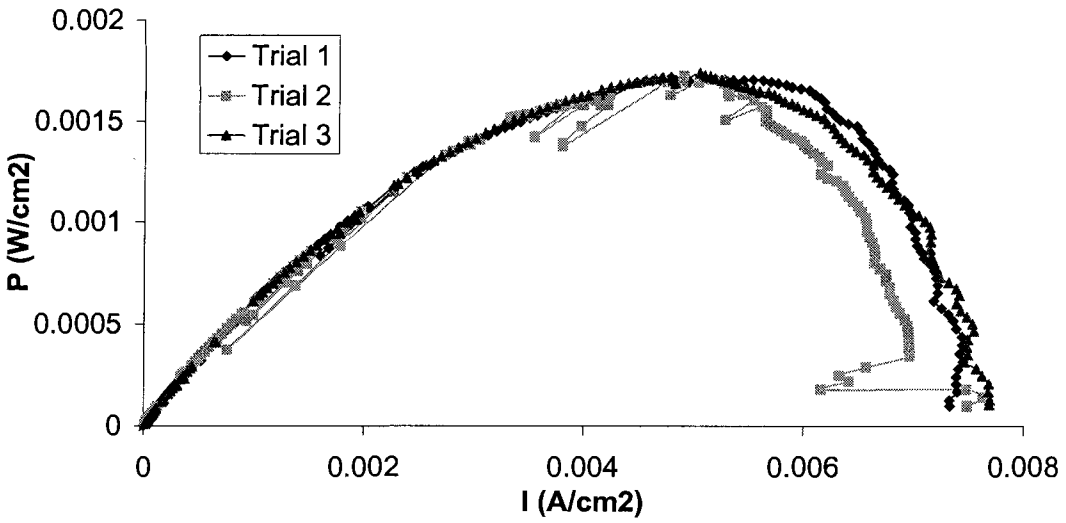

Figure 62:Silver anode composite membrane passive cathode power curves

The cell achieves a maximum power density of approximately 1.7 mW/cm^2 repeatably. While the cell might have reached 2 mW/cm^2 without flooding, the performance is clearly only of academic interest because it is well short of the specifications outlined in chapter 1. Determining the overall impedance and the contribution of the mass transport is of critical importance in determining the source of the poor performance. All three curves follow the same trends, however, the second curve exhibits a DC offset. This is usually indicative of higher crossover; however, because it is the middle trial, the offset is unlikely due to crossover, as pinholes don't generally repair themselves. The slightly lower overall performance could also indicate a flooded region, decreasing the actual catalytic area, and therefore reducing the surface current density.

4.3.2.2.2 Carbon Anode

The carbon anode composite membrane prototype was created as a control for the silver anode composite membrane, as well as to evaluate the impact of membrane type with GDL type to aid in design impact analysis. The resistance of each of the carbon GDLs was significantly less than the resistance of the anode cathode layer. Although the resistance of each electrode is less than the cathode of the silver anode cell tested, the total resistance of the cell is higher than the silver-carbon cell, which should still result in a measurable performance increase over the carbon only cell. The polarization curves for the carbon anode on composite membrane cell are shown in Figure 63.

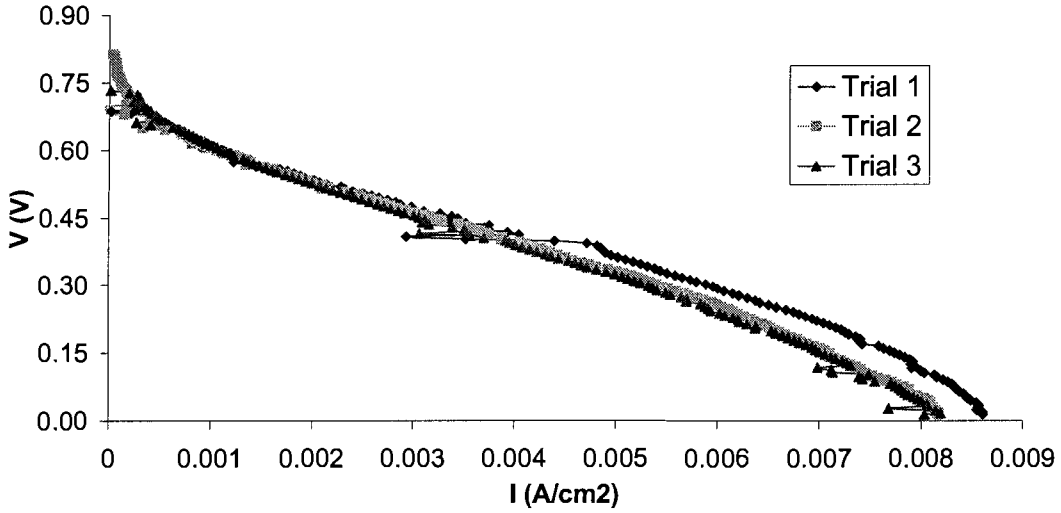

Figure 63:Carbon anode composite membrane passive cathode polarization curves

The carbon only cell has a lower OCV of between 0.7 and 0.8V, which is likely explained by a leak in the membrane or the cell seal. Because of the qualification testing of the membrane, a leak in the seal seems more likely. The cell reaches a short circuit current of between 8 and 9 mA/cm^2. On the surface this performance exceeds the silver anode cell. However, while some flooding is indicated by the slight roll-off above 7 mA/cm^2, the impact is clearly not of the same magnitude as in the silver anode case. This difference in flooding behavior likely indicates a difference in porosity between the two GDL formulations. However, neither formulation meets the requirements determined in chapter 2. The power curves for the passive trial of the carbon anode on composite membrane prototype are shown in Figure 64.

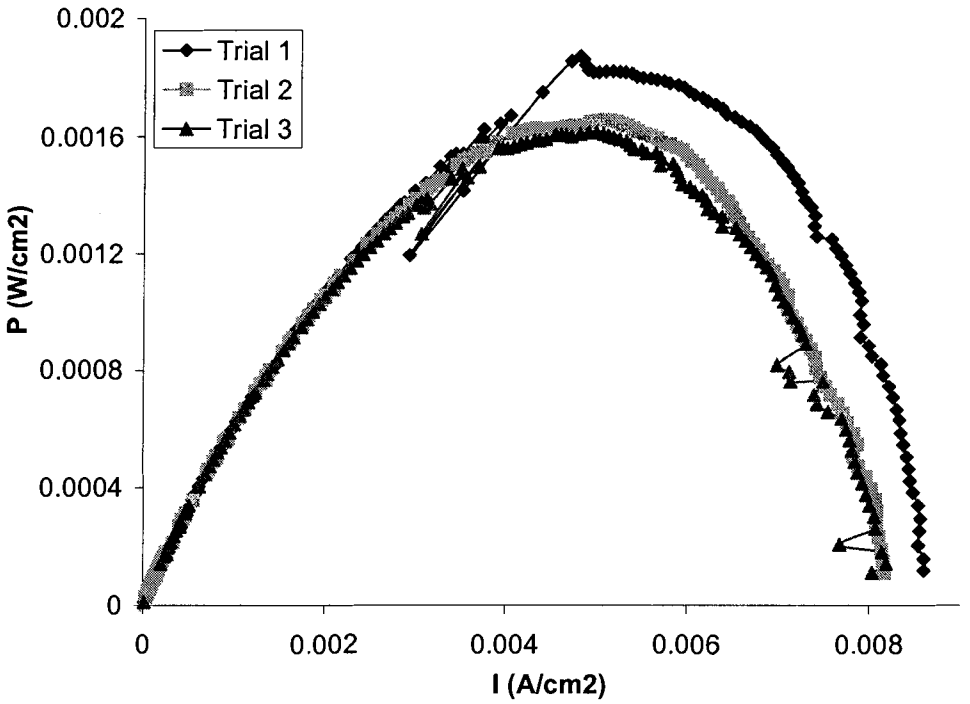

Figure 64:Carbon anode composite membrane passive cathode power curves

Peak power densities of between 1.5 and 1.8 mW/cm^2 were recorded. The power density is almost equal to the power density recorded in the silver anode trial. This result would indicate that the impedances in each case are approximately equal. However, we know that the impedance of the silver anode cell is lower. Another impedance must be present in the anode cell to explain the difference in measured impedances; this impedance could be an impact of the mass transport limitation exhibited in Figure 63.

4.3.3 Active Cathodes

Although micro fuel cells would not use forced air during operation, forced air operation can provide useful information about characteristics of the fuel cell by reducing the impact of mass transport, and allowing control of the humidity at the cathode. In these experiments, we employed humidified air at room temperature at 100 mL/min to provide an excess of air to the

cathode. Both the carbon and silver anode on composite membrane were tested, and the results are presented in this section.

4.3.3.1 Silver Anode

The same cell used in the previous experiments had flow channels added to the cathode and the same experiment was repeated with forced air at the cathode. The forced air should minimize the mass transport effects seen in the previous tests. The polarization curves for the forced air trial of the silver anode cell are shown in Figure 65.

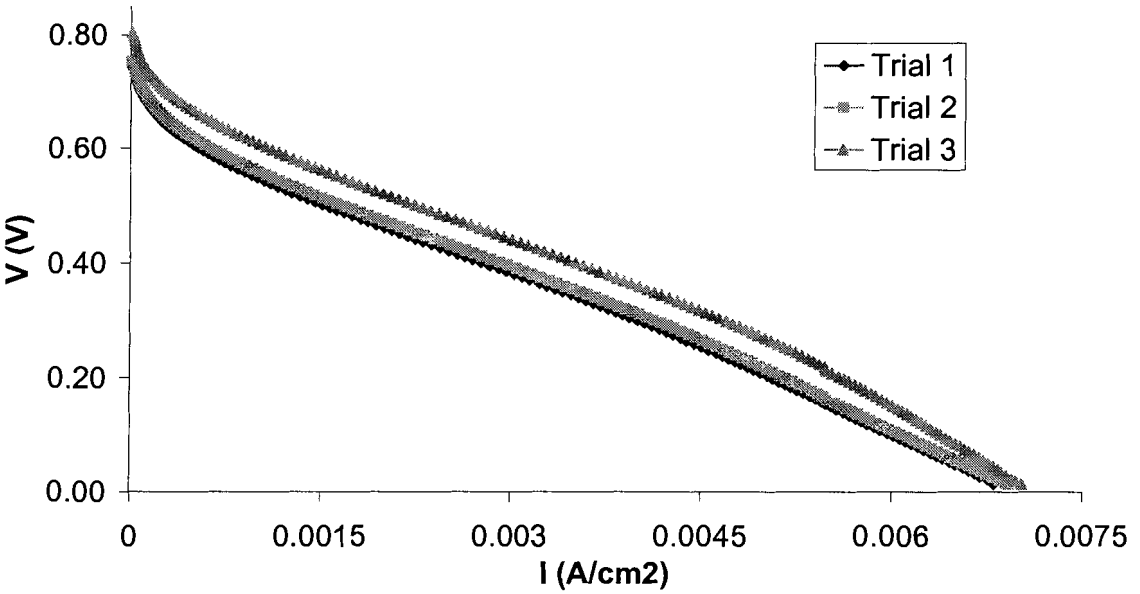

Figure 65:Silver anode composite membrane active cathode polarization curves

Although the forced air did reduce the impact of the mass transport losses, a subtle tailing off is still evident in all curves in Figure 65, indicating that mass transport was still impacting the performance. This data reinforces our hypothesis that the GDL is not as porous as designed. A drop in open circuit voltage to between 0.7 and 0.8 V was shown in Figure 65 from the passive cathode experiment, indicating the presence of a leak either through the

membrane or through the seals introduced during the addition of the cathode flow field. The power curves corresponding to the silver anode forced air cathode is shown in Figure 66.

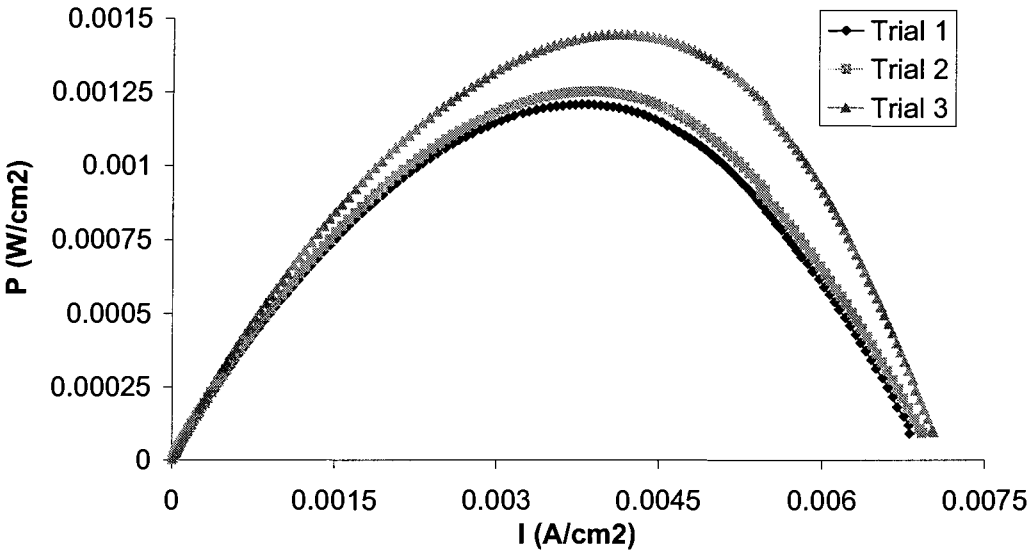

Figure 66:Silver anode composite membrane active cathode power curves

The power performance of the cell degraded slightly, from the passive cathode case. The decrease in power output was proportional to the open circuit voltage drop. The peak power for the closed cathode silver anode cell is between 1.2 and 1.4 mW/cm^2. Evidence of continued flooding is present in this diagram. If no flooding were present, the polarization would be linear in the Ohmic region, and the power, the product of potential and current, would have a parabolic form. Because the trailing edge of the power curve is slightly flattened away from an ideal parabola, we can deduce that mass transport limitations exist. Given that this trial employs forced air at the cathode, mass transport limitations are likely due to flooding closing existing pores.

4.3.3.2 Carbon Anode

The carbon anode control proved to have significantly better performance with respect to the silver anode cell than we initially anticipated. The carbon on composite membrane represents a performance floor for the architecture and materials. The forced air polarization curves for the carbon anode on composite membrane cell are shown in Figure 67.

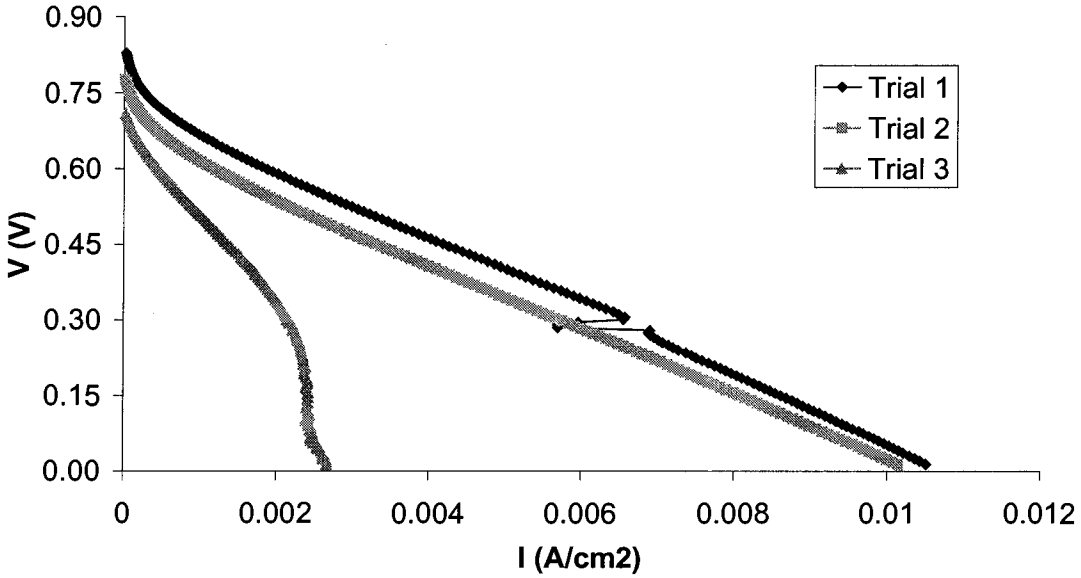

Figure 67:Carbon anode composite membrane active cathode polarization curves

A slight increase in the OCV between the carbon anode passive and forced air systems was expected because of the slightly higher partial pressure of oxygen. The new OCV was between 0.75 V and 0.8 V, neglecting the third trial where a bubble of water passed from the test station into the cell. The discontinuity near 7 mA/cm^2 in the first curve was caused by an experimenter bumping the apparatus and jostling the test leads. However, as the nonlinearity was entirely artificial we included the experimental data. The short circuit current reached 10 mA/cm^2 for the first and second trials. Figure 68 shows the power curves for the carbon anode active cathode case.

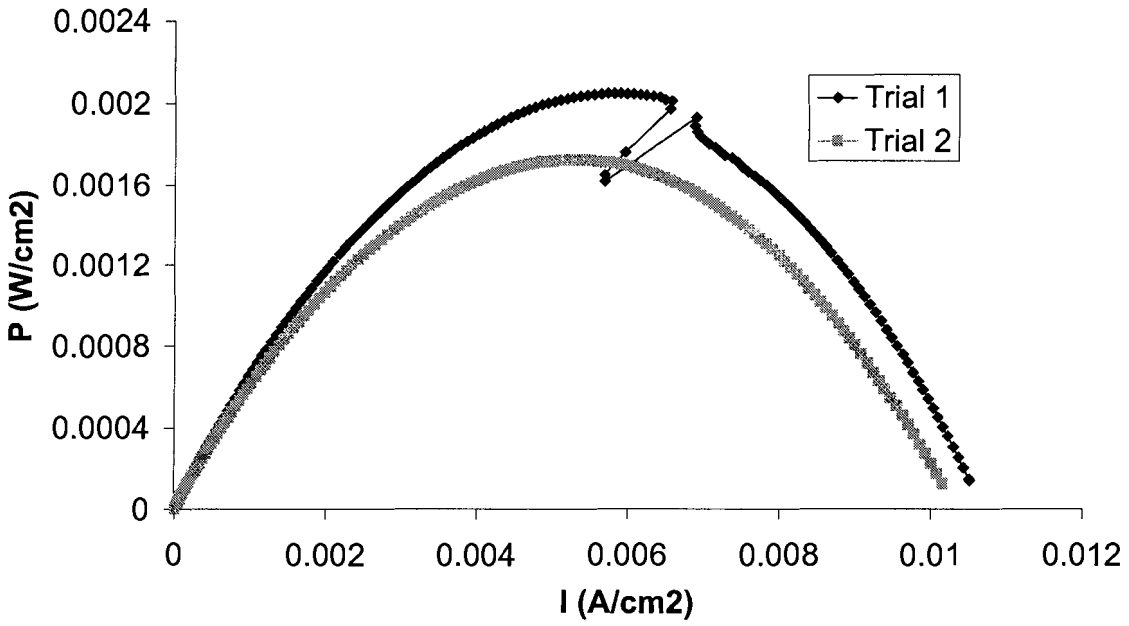

Figure 68:Carbon anode composite membrane active cathode power curves

The peak power is between 1.5 and 2 mW/cm^2. This result is superficially consistent with the theoretical limitations in Table 19, but is still lower than expected. The forced air has significantly smoothed the curve, supporting our hypothesis that some of the noise in the passive signals is due to transient mass transfer effects. To make any definitive conclusions about the cell behavior, the relative impacts of mass transport and Ohmic losses need to be isolated. To isolate the relative impacts of the Ohmic and mass transport contributions, the superimposed effects must be isolated. Although it is impossible to directly uncouple the effects, taking the derivative will reduce the impact of the linear Ohmic losses and enhance the impact of the nonlinear mass transport losses.

4.3.4 Polarization Curve Derivatives

The numerical derivative of a curve can yield information that is not readily apparent in the parent function. Polarization curves are no exception. By taking the derivative of a polarization curve, the nonlinear portions are enhanced, while the linear contributions are

diminished and any constant systematic errors are removed; however, noise is amplified. If the noise is due to the experimental apparatus, the noise amplification can be an undesirable side effect; however, if the noise is due to periodic system effects such as small pockets of liquid intermittently forming in the catalyst layer and transporting out through the GDL under capillary forces, the noise-amplification properties of the derivative can be informative. An ideal polarization curve derivative is shown Figure 69.

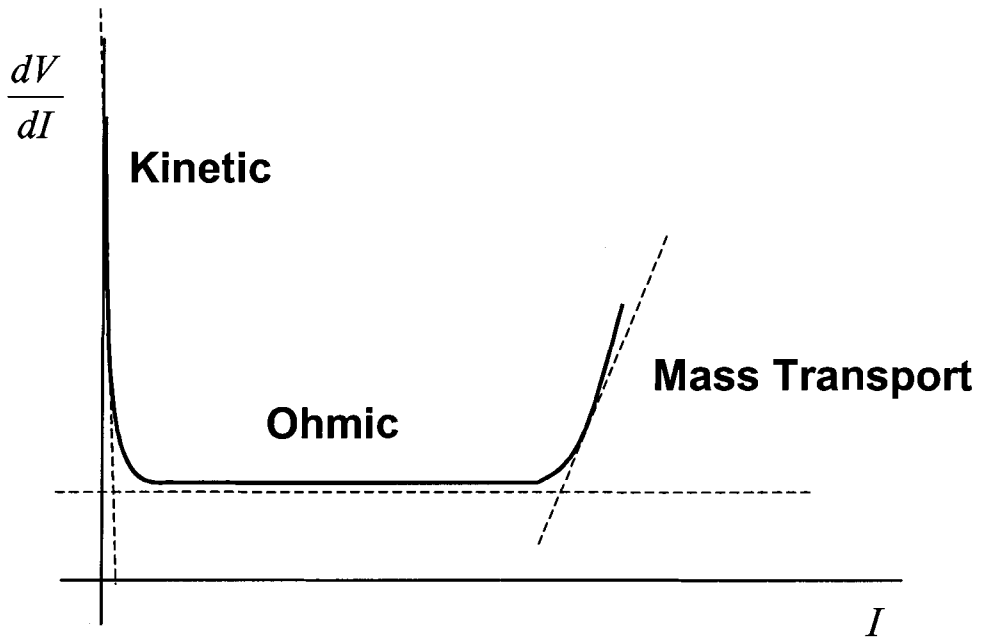

Figure 69:Idealized polarization curve derivative

The behavior of this curve is strongly dependant upon the material parameters of the cell and the operating conditions the cell is exposed to. To calculate reasonable bounds for the nonlinear slopes, we have used the output of our simulation covered in section 2.5.4 to generate asymptotes for the kinetic and mass transport region. The kinetic region had a significant slope of –100 Ω/A, while the mass transport region has a modest slope of 2 Ω/A.

The derivative is characterized by three distinct zones, similar to the polarization curve, corresponding to kinetic, Ohmic, and mass transport limited operating regimes. However, the

behavior of the curve in these regions differs. The kinetic region is almost unchanged, as the derivative of an exponential is another exponential. The plot of the Ohmic region exhibits a constant plateau, because resistive losses are linear, and the mass transport limited losses are defined by a negative exponential, so there is a sign change from decreasing voltage to increasing impedance, but everything else remains the same.

In addition to the three major zones described above, there are three transition zones. In the first transition zone, the impact of kinetic or activation losses decreases, and gives way to losses from Ohmic heating. This transition region is characterized by a local minimum, which corresponds to the transition point between Ohmic and kinetic losses. The second transition region corresponds to an increasing mass transport loss impact. Unlike the polarization curve, small changes in mass transport impedance are amplified over the constant value Ohmic losses, making it simpler to identify the point where mass transport begins to affect the fuel cell.

Because we have defined the derivative as the change in voltage over the change in current, the derivative of the polarization curve is the instantaneous impedance of the fuel cell. The average value of the constant region can therefore be considered as the net contribution of all Ohmic loss mechanisms, or the overall effective resistance of the cell.

4.3.4.1 Passive Cathodes

Passive cathodes are more likely to experience mass transport fluctuations than active cathodes, so we would expect to see an earlier contribution from the mass transport losses. Therefore, we would expect the behavior of the passive cathodes to mimic the graph shown in Figure 69. Polarization derivatives for a carbon anode on Nafion, and silver anode on composite membrane are shown in Figure 70 and Figure 71.

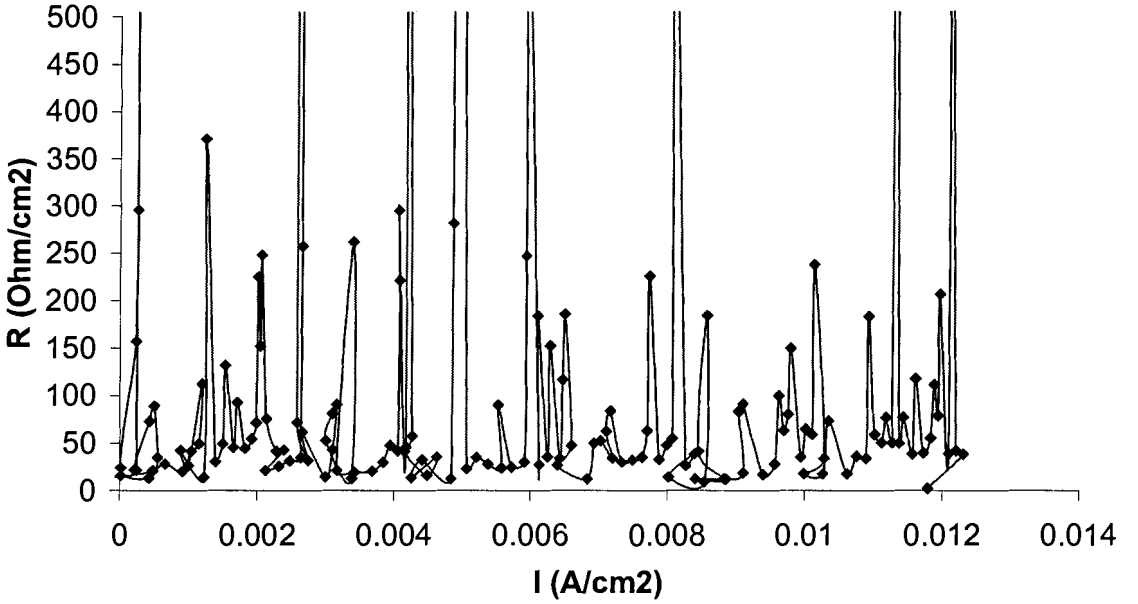

Figure 70:Carbon anode Nafion membrane passive cathode polarization curve derivative

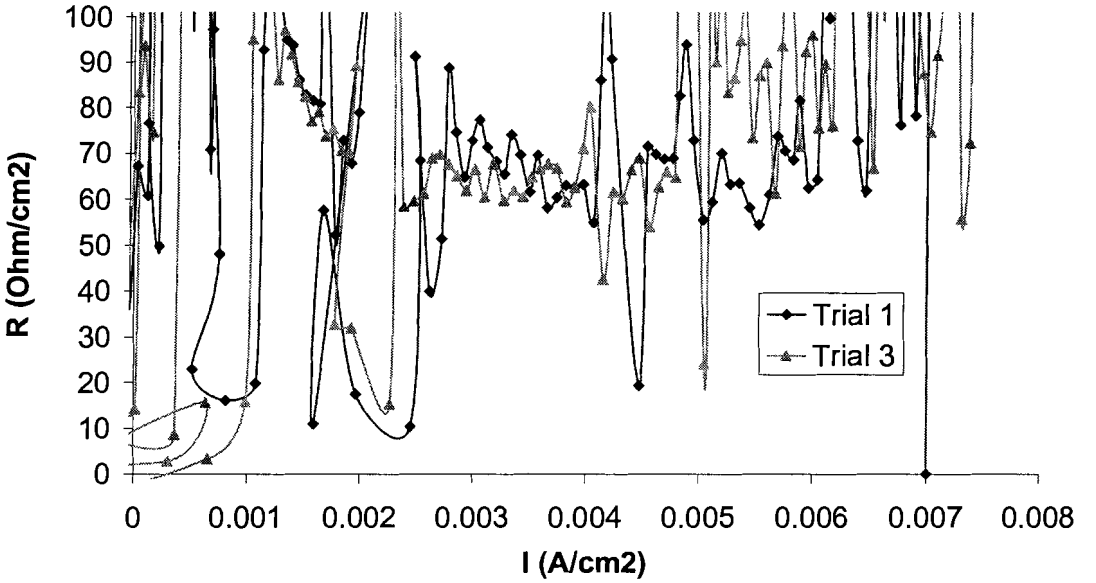

Figure 71: Silver anode composite membrane passive cathode polarization curve derivatives

The noise was present throughout the signal, obscuring the expected behavior. Derivative values extend well beyond limits shown in the graphs for some points; these values have been

truncated to demonstrate the behavior of the majority of the signal. The behavior cannot be due to silver, as the noise is present in the carbon anode as well. The noise cannot be due to (but may be exacerbated by) the composite membrane as the behavior is also present in the Nafion-based system. In fact, this behavior was observed across all the passive cathode experiments we have performed. We must conclude that the noise is due to mass transport effects in the cathode. Although we do not have a theoretical basis to explain this behavior, the most logical assumption would be sporadic accumulation of products in local areas, which cannot be instantaneously cleared and results in a small reduction in current density. Our simulations assume steady state operation and would not reveal this behavior. This behavior was indicated in the polarization data, but easily dismissed as random noise until the derivative was taken and the pervasiveness of the effect became apparent.

4.3.4.2 Active Cathodes

The derivative behavior in active cathodes should be similar to Figure 69, with a delayed onset of mass transport limitations. It should be easier to identify the effective resistance for the silver and non-silver anode cells, because their polarization curves appear qualitatively smoother than the passive air breathing curves. The derivative curves for active cathode circulation for the carbon and silver anode configurations are shown in Figure 72 and Figure 73, respectively.

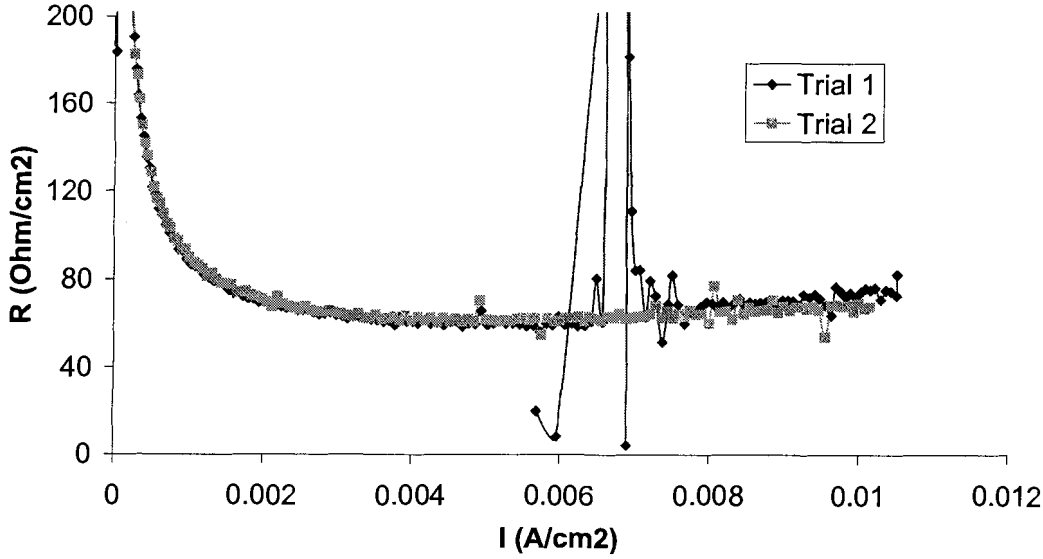

Figure 72:Derivatives of the carbon anode composite membrane active cathode polarization curve

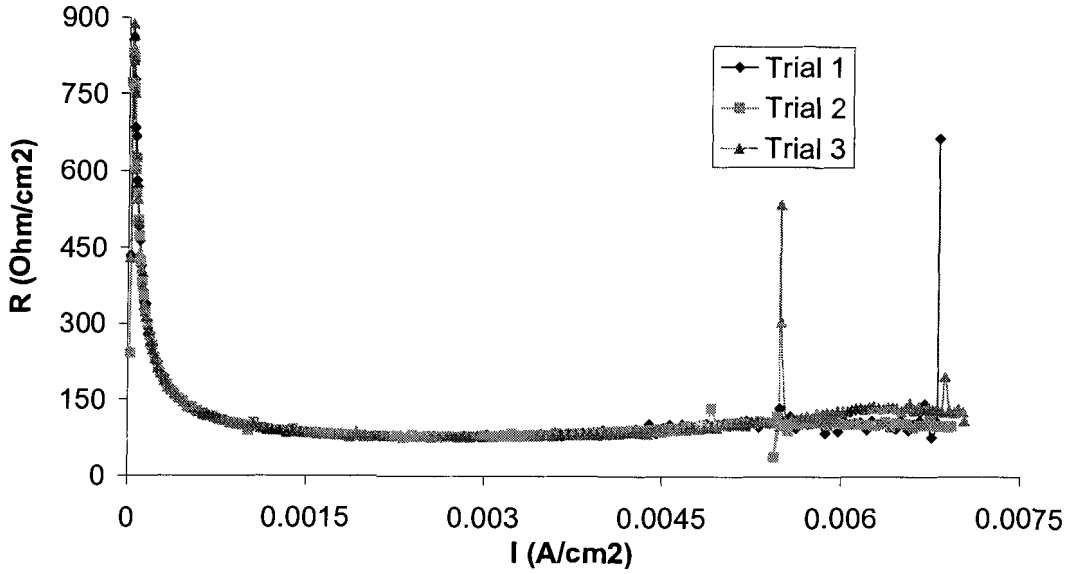

Figure 73:Derivatives of the silver anode composite membrane active cathode polarization curve

As expected, significantly less noise, and correspondingly smoother derivative signal were present in the active cathode case. The mean resistances are 2-3 orders of magnitude higher than in a highly tuned macro PEM stack. One order of magnitude could have been acceptable

as micro fuel cells are expected to run at much lower current densities. The current Ohmic losses are too large for any practical application. The derivative also shows that the onset of mass transport limitation occurs at only 4 mA/cm^2 in the silver anode case, and 6 mA/cm^2 in the silver anode case, much earlier than expected given our estimates of the GDL porosity. The simplest explanation for this discrepancy is that the porosity of our GDL is significantly lower than estimated.

Unexpectedly, the carbon anode had a lower characteristic resistance than the silver anode, even though the four point probe measurements of the electrode showed a much smaller total resistance for the silver anode than the carbon anode, and a correspondingly smaller total resistance. To make a more direct comparison of the material data to the polarization curves, Figure 72 and Figure 73 have been regraphed in Figure 74 and Figure 75 to show total resistance of the electrode versus total current, which should correspond to data presented in Table 19. The steep decline due to the kinetic losses at low current densities have been cropped and to amplify effects in the Ohmic and mass transport regions.

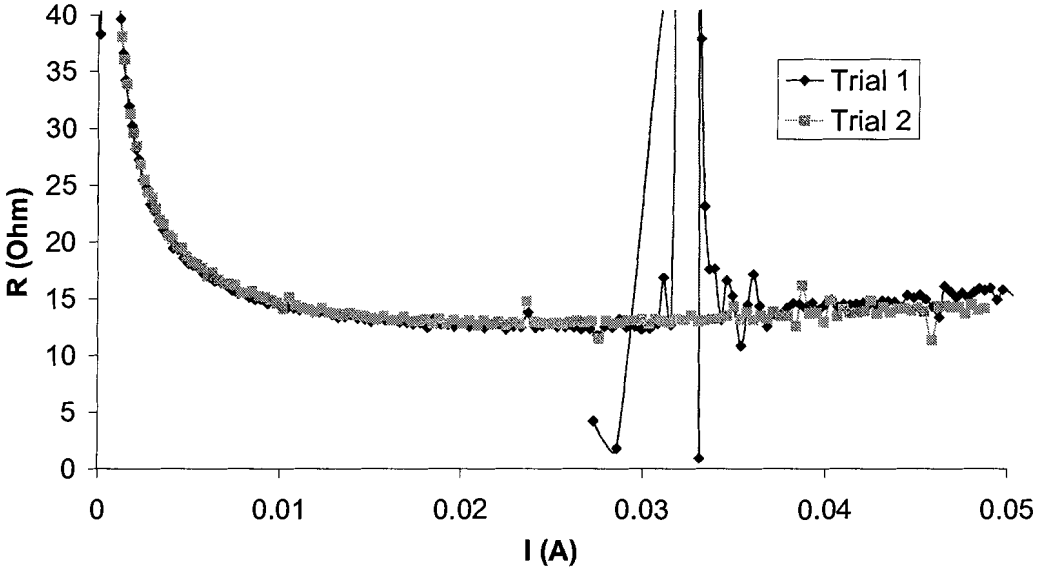

Figure 74:Carbon anode composite membrane active cathode total current polarization curve derivatives

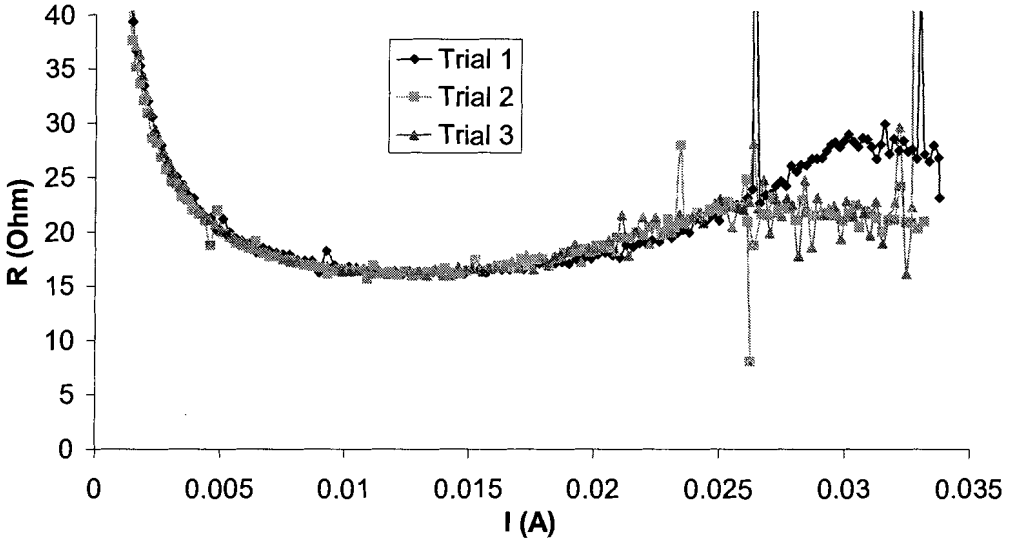

Figure 75:Silver anode composite membrane active cathode total current polarization curve derivatives

The total resistance of the carbon anode electrode is approximately 13 Ω, and the total resistance of the silver anode is 17 Ω. The measured resistance was 12.2 Ω and 8.45 Ω respectively and the equivalent resistance for an edge-collected cell as calculated from the

estimate in chapter 2, section 2.4. In both cases the contribution from the membrane should be small compared to the electrode resistance. However, the silver anode system is inconsistent with both theory and measurement. There are two possible explanations for this discrepancy.

First, while related literature [27, 29] and experiments at the Institute for Fuel Cell Innovation seem to indicate that silver is electrochemically compatible with the anode environment, it is possible that some unknown secondary processes occurs, causing a large enough mixed potential to appear as an additional contact resistance. In the simulations we assumed a perfect interface between the catalyst layer and the GDL. Second, it is possible that the silver GDL has poor contact with the catalyst layer, while the carbon GDL does. This resistance would not be detectable with a resistance measurement because the GDL and thin film and catalyst layer are in parallel. A large resistance between the catalyst layer and GDL would not contribute significantly to the overall resistance because the net resistance as measured by the ohmmeter would be dominated by the low resistance thin-film and GDL layers. We ignored contact resistances between layers because we assumed that layers, which were cast on top of each other, would have low contact resistances.

4.4 Discussion

Several points of discussion were presented in this section. The performance of the fuel cells was much poorer than we expected, primarily attributed to Ohmic losses, attributed to the low conductivity of the carbon cathode layer. However, these losses are larger than predicted by both our edge-collected loss approximation and the worst-case approximation. Finally, the mass transport of water away from the cathode was impeded to a greater extent than predicted, likely due to lower porosity of the GDL, but it could also be due to lower back diffusion of

water in the membrane, due to the lower Nafion loading in the composite, because mass transport limitations were not observed in the Nafion system.

The primary reason for the lower than expected performance was the low conductivity of the cathode. Initially, we had intended to use the silver GDL on both poles of the fuel cells. However, work by other researchers in our lab [98], indicates that silver is not generally stable on a fuel cell cathode, and can cause severe performance degradation by generating a mixed potential and consuming electrical power to oxidize silver instead of producing power, even though evidence exists in the literature that silver is chemically compatible with the fuel cell environment [27, 29]. If silver had been used on both the anode and cathode, the resistance of the cell would have been at most 1 Ω, meeting the requirements outlined in chapter 2. Instead, the carbon only cathode had resistances ranging between 5 and 20 Ω, an increase of over an order of magnitude, and constitutes the primary cause for the poor performance of the cell. Future research must identify a more conductive and fuel cell compatible cathode material, which will meet the requirements described in chapter 2. Gold is an obvious candidate, but its cost is prohibitive. Gold coated carbon fibers or flakes are also excellent candidates, however, they are not readily available. While gold coated fibers would have a lower cost than solid gold, experimentation would be required to determine if the gold coated fibers improved conductivity sufficiently at sufficiently low gold loading.

Most of the performance shortcomings can be attributed to the low conductivity of the carbon GDL; however, additional Ohmic losses are evident. In particular, the silver anode system has significantly higher Ohmic losses than would be predicted from the measured resistance, possibly due to leaching of silver ions across the membrane to the cathode. We have extracted the net Ohmic losses by taking the derivative of the polarization curve, an

uncommon step in fuel cell analysis, but helpful in determining the underlying effects creating the curve.

Several possible mechanisms exist for introducing this resistance. Ohmic losses through the catalyst layer in both the solid and ionic phases can be significant. However, these losses were not included in the simulations in chapter 2. Additionally, the magnitude of the losses in the catalyst layer was insufficient to explain the losses observed here. Contact resistance between the connecting wire interface and the electrode is included in the resistance measurement; therefore the larger cell resistance cannot be attributed to static contact resistance between wire and electrode. However, considerable mechanical play exists in the connecting wire, which could lead to a variable and generally increasing contact resistance, implying the change in impedance is one of circumstances, not an underlying issue with the model or materials. In the models in chapter 2, we assumed perfect contact between the catalyst layer and GDL; no potential drop occurred across the interface. This assumption was reasonable given that the layers were composed of similar materials deposited on one-another during fabrication instead of mechanically affixed. This assumption may not hold true in practice, given that regions of high impedance along the interface due to poor interlayer adhesion, local micromorphological mismatches or a settling of the insulating binder toward the interface occurs. Any of these effects could create a high contact resistance along the GDL/carbon interface. The impact of the catalyst layer resistance would not be present in the resistance measurement because the catalyst is in parallel with the GDL and gold in this configuration, and has a much higher resistance, therefore the measurement will generally capture the high conductivity branch. Finally, it is possible that the assumptions underlying the edge collection calculations are wrong, and that there are electrochemical effects that occur

under conditions of high Ohmic loss, which add to the impact of the Ohmic losses. However, given that this explanation contradicts the superposition of losses assumption in almost all the fuel cell literature, this explanation seems unlikely. The additional Ohmic losses are likely a combination of degradation and contact resistances within the cell over the duration of testing.

The mass transport effects observed in the composite membrane fuel cell were much more severe than predicted by theory. The onset of flooding occurred at a current density an order of magnitude smaller than predicted by theory for the operating conditions. Most of this shortcoming was due to a lower than anticipated porosity of the GDL. Although the mass fraction calculations were correct, the distribution of the pores might not be consistent with good mass transport through the membrane. The underlying assumption of the mass fraction method is the pores are normally distributed, allowing a reasonable mapping from solid content to effective diffusion coefficient. If the distribution were based on a high number of small pores, the tortuosity would increase, decreasing the effective diffusion coefficient. If the distribution favored a few very large pores, the dispersion of gases would be primarily through the catalyst layer, increasing the diffusion length. The composite membrane could have contributed to the mass transport problems. While we have no direct evidence that the membrane's water transport property impacts the onset of flooding at low current densities, neither of the Nafion cells showed evidence of flooding. The composite membrane might have different transient water transport and retention properties, the current density appears too low to affect the water transport and retention properties of the membrane.

4.5 Summary

We fabricated a series of fuel cells based on the general design outlined in chapter 3, and their performance was tested using a commercial fuel cell test station. The results obtained in

these tests were worse than predicted. Because the carbon GDL electrodes could not achieve the conductivity outlined in the requirements outlined in chapter 2, the fuel cells did not achieve the desired performance. Peak power densities between 2 and 4 mW/cm^2 were achieved. Although most of the losses were due to the carbon GDL, some Ohmic losses could not be accounted for in the measurements. These losses are most likely due to a combination of changing contact resistances throughout the cell. Flooding occurred earlier than expected, likely due to a lower than anticipated porosity in the GDL, and potentially exacerbated by the water transport properties of the composite membrane. Although the fabrication process and experiments failed to produce a commercially viable fuel cell, they did provide a proof of concept for our design and new avenues of research for refinement of the inside-out fuel cell architecture.

Chapter 5 Summary and Conclusions

5.1 Summary

This research detailed the systematic design and fabrication of a flexible micro fuel cell using a hybrid MEMS technique. We developed the design through the analysis of the state-of-the-art in fuel cell design, and an analysis of the theoretical performance boundaries of micro fuel cell design through both analytical and FEA methods. The derived design required new materials, which were thoroughly characterized prior to fuel cell testing. The fuel cell itself was put through a range of tests to determine the overall performance and to discover which components of the fuel cell cause the losses. The work has lead to a new architecture, fabrication techniques, theory and analysis of micro fuel cells.

5.1.1 Micro fuel cell taxonomy and problem statement

Our analysis of the fuel cell literature led to a classification system where an individual fuel cell could be classified by architecture and fabrication technique. By examining the advantages and disadvantages of each fuel cell architecture we concluded that the best candidate for very small fuel cells was an inside-out fuel cell architecture, and identified material and process shortcoming that must be addressed through new research.

5.1.2 Theory and Simulation

We analyzed three key areas in micro fuel cell design: the minimum flow field dimension based on micro fluidics; the Ohmic losses due to edge collection geometry; and the impact of electrode geometry, physical structure, and environment on passive cathodes. Results from this analysis were combined with the general requirements elucidated in the literature to derive quantitative requirements for the fuel cell design.

5.1.3 Design and Fabrication

The design and fabrication of our fuel cell was based on the combination of the operational constraints derived in chapter 2 and the general constraints in chapter 1. Our examination of the potential fabrication techniques and architectures has led us to conclude that the inside-out fabrication technique has the most long-term promise, but requires a dimensionally stable membrane for the substrate and a castable GDL. The fabrication process was chosen to provide acceptable resolution at minimum cost, by using a hybrid fabrication technique where the tool and die is fabricated using MEMS techniques and the cell itself is fabricated using more traditional manufacturing techniques.

5.1.4 Results

Given the low conductivity of the carbon GDLs, the results were poorer than specified in chapter 1, and predicted in chapter 2. The maximum power densities for the 6 test configurations were between 1.5 and 4 mW/cm^2, over an order of magnitude less than the requirements for this stage of research. Using the derivative of the polarization curve to determine the relative impact of the different loss regimes, we found that the losses exceeded the Ohmic drop anticipated from the carbon GDL alone. The additional Ohmic drop could be due to higher than expected contact resistances between the catalyst and GDL layers and/or degradation of the contact between the electrodes and the bonding wire. Flooding occurred earlier than expected, likely due to a lower than expected porosity in the GDL potentially exacerbated by the transient water transport properties of the membrane. If flooding occurred early enough it could begin to impact the performance of the fuel cell before the Ohmic losses. This effect would result in derivative curves similar to those shown in chapter 4, where no constant region exists. Although the prototypes failed to achieve the power requirements

necessary for a commercial system, they demonstrated feasibility and opened new avenues of research in material design for micro fuel cell systems.

5.2 Contributions

Our research has lead to a single major contribution: the creation of a new flexible inside-out fuel cell technology. Our fuel cell is unique and has a solid scientific base in both theoretical and practical analysis. The research leading to the major contribution was composed of five complementary contributions:

- A micro fuel cell architecture and fabrication taxonomy;
- An analysis of micro fuel cell electrode design;
- The architecture of the fuel cell itself;
- A hybrid MEMs technique used to fabricate the fuel cell; and
- The membrane and GDL materials.

5.2.1 Taxonomy

Although not a research topic in and of itself, the taxonomy provides a valuable overview and classification system that can be used to analyze the relative merits of different micro fuel cell architectures and fabrication processes. While [9] has examined the role of electrode configurations, nobody has summarized and codified both fabrication technique and structure of micro fuel cells. The taxonomy can be used to inform fuel cell design and fabrication research and provide a common vocabulary for describing micro fuel cell design.

5.2.2 Electrode analysis

The lower than expected performance of most micro fuel cells reported in the literature can be attributed to the poor performance of the electrodes. The electrodes either have too high an impedance or to low a porosity. By deriving a new approximation for the edge collection Ohmic losses and performing a FEA analysis on the impact of passive mass transport on electrode flooding, we were able to derive physical parameters for the fuel cell dimensions and GDL properties. Most of the academic fuel cell systems do not present any theoretical background for their designs.

5.2.3 Architecture

By combining the theoretical analysis of electrode behavior with the qualitative analysis of the state of the art, we were able to design a unique micro fuel cell architecture. We have one of two inside-out fuel cell architectures reported in the literature. However, our fuel cell is built using an optimized electrode macro structure and standard fuel cell platinum-carbon catalyst. The combination of an inside-out design and material choices allow us to create a flexible fuel cell. Our fuel cell has the unusual mechanical properties of flexibility, mechanical robustness, allowing the possibility to manufacture using a reel-to-reel type printing process.

5.2.4 Fabrication Technique

The fabrication technique is closely related to the architecture: new fuel cell designs required new fabrication techniques to realize them. The fabrication technique we have developed uses a hybrid-MEMS technique to create the cell, maintaining the required resolution while gaining the manufacturability of traditional techniques. Hybrid-MEMS techniques are particularly suited to micro fuel cell design, because traditional fuel cell

techniques cannot achieve the necessary resolution to create flat stacks of strip cells for portable applications; and silicon MEMS techniques cannot create micro fluidic devices with long length scales economically. Other researchers use either silicon MEMS techniques to fabricate the flow field and current collectors and standard MEAs, or they use complicated fabrication techniques characterized by sequential CVD and DRIE processes. Our process is one of the only documented processes to provide sufficient resolution with low cost manufacturing techniques.

5.2.5 Materials

Neither traditional fuel cell materials, nor the ceramic materials commonly used in MEMS systems are entirely appropriate for the fabrication techniques and architecture described in this thesis. To realize the architecture, we created two new materials. First, a supported membrane was required to provide a stable substrate for functional layer depositions. Our membrane has unique mechanical properties, which give it exceptional stability under varying hydration levels, and significantly better mechanical properties than other membranes reported in the literature. Second, we have created applied and tested a castable GDL created by other researchers in our lab. Our flexible conductive GDL is unusual and allows our fuel cell the high degree of mechanical flexibility and robustness that makes it mechanically useful.

5.3 Future Work

Most research leaves more questions posed than answers found. The cycle of research leads from one problem to another, and fuel cell research is no exception. Although the phenomena underlying fuel cells have been known for over a century, fuel cell technology is a new an emerging engineering discipline. There are significant questions remaining with

respect to the fabrication, performance, and durability of fuel cells. The research described in this thesis has addressed problems in micro fuel cell implementation involving architecture, fabrication, and materials. Open research questions have been identified in the context of optimizing the performance of the existing architecture, and new research areas in passive water management, impedance mapping of edge collected cells, and hybrid manufacturing.

5.4 Conclusions

We have created a new fuel cell architecture and fabrication technique based on a hybrid MEMS fabrication techniques and supported by theoretical analysis. Although we were able to make significant advances in the fabrication and membrane materials, our cathode gas diffusion layer material was insufficiently conductive and porous for commercial fuel cell performance. Our modeling and analysis showed that the fuel cell could work if materials with proper characteristics can be found.

Our initial intent was to design a new fuel cell fabrication process that could achieve the volumetric requirements, with enhanced mechanical properties, and amenable to mass production. Although we have achieved that goal, the new architecture and fabrication process required new materials. Despite all the advances over the last decade, fuel cells are still material-centric systems. The material advances, which gained fuel cells new interest and acclaim, were primarily empirical. Changing the fundamental fuel cell architecture requires new materials based on the same empirical techniques. Substantial materials advances for all fuel cell components will be required if any fuel cell is to achieve commercial success. New architectures must inform the materials research effort. In creating our new fuel cell architecture, we have advanced the state of the art in fuel cell design and posed new materials research questions.

References

1. J. Larminie, A. Dicks *Fuel Cell Systems Explained* John Wiley & Sons, Chichester, 2000.

2. S.J.C. Cleghorn, C.R. Derouin, M.S. Wilson, S. Gottesfeld "A printed circuit board approach to measuring current distribution in a fuel cell," *Journal of Applied Electrochemistry*, 28, 2000, pp. 663-672.

3. X. Ren, P. Zelenay, S. Thomas, J. Davey, S Gottesfeld "Recent advances is direct methanol fuel cells at Los Alamos National Laboratory," *Journal of Power Sources,* 86, 2000, pp. 111-116.

4. G. McLean, N. Djilali, M. Whale, T. Niet, "Application of micro-scale techniques to fuel cell systems design," *10th Canadian Hydrogen Association Conference* Quebec 2000, pp. 760-768.

5. S.C. Kelly, G.A. Deluga, and W.H. Smyrl, "A miniature methanol/air polymer electrolyte fuel cell," *Electrochemical and Solid-State Letters* 3 (9), 2000, pp. 407-409.

6. R. Hockaday, M. DeJohn, C. Navas, P. Turner, H Vaz, L Vazul, "Development of Micro-Fuel Cells™ for Cellular Telephones," *International Conference with Exhibition-Fuel Cell 2000*, 2000, pp. 37-44.

7. W. Y. Sim, G. Y. Kim, S. S. Yang, "Fabrication of micro power source (mps) using a micro direct methanol fuel cell (udmfc) for the medical application," *14th IEEE International Conference on Micro Electro Mechanical Systems,* 2001, pp.341-4.

8. S.J Lee, A. Chang-Chien, S.W. Cha, R. O'Hayre, Y.I. Park, Y. Saito, F.B. Prinz "Design and fabrication of a micro fuel cell array with "flip-flop" interconnection," *Journal of Power Sources,* 112, 2002, pp. 410-418.

9. J.P. Meyers, H.L. Maynard, "Design considerations for miniaturized PEM fuel cells," *Journal of Power Sources*, 109, 2002, pp. 76-88.

10. K.B. Min, S. Tanaka, M. Esashi, "MEMS-based polymer electrolyte fuel cell," *Electrochemistry*, 70 (12), pp. 924-927.

11. Heinzel, C. Hebling, M. Muller, M. Zedda, C. Muller, "Fuel cells for low power applications," *Journal of Power Sources*, 105, 2002, pp. 250-255.

12. S.C. Kelley, G.A. Deluga, W.H. Smyrl "Miniature fuel cells fabricated on silicon substrates," *AIChE Journal* 48 (5), 2002, pp.1071-1082.

13. K. Ishida, T. Okada, M. Ishida, "Micro-tubular direct methanol fuel cells for portable applications," *Electrochemistry*, 70 (12) 2002, pp. 975-979.

14. G. D'Arrigo, C. Spinella, G. Arena, S. Lorenti, "Fabrication of miniaturized Si-based electrocatalytic membranes," *Materials Science and Engineering C,* 23, 2003, pp. 13-18.

15. A.F. Jankowski, J.P Hayes, R.T. Graff, J.D. Morse, "Micro-fabricated thin-film fuel cells for portable power," *Symposium V on Materials for Energy Storage, Generation and Transport*, 2002, pp. 93-98.

16. G.A. Tompsett, M.S. Brown, C. Finnerty, N.M. Sommes, K. Kendall, "Design of a tubular micro-SOFC demonstration system," *Fourth European Solid Oxide Fuel Cell Forum*, July 2000, pp. 13-18.

17. J. Yu, P. Cheng, Z. Ma, B. Yi, "Fabrication of miniature silicon wafer fuel cells with improved performance," *Journal of Power Sources,* 124, 2003, pp. 40-46.

18. K. Shah, W.C. Shin, R.S. Besser, "A PDMS micro proton exchange membrane fuel cell by conventional and non-conventional microfabrication techniques," *Sensors and Actuators B, 97, 2004, pp. 157-167.*

19. Y.H. Seo and Y.H. Cho, "MEMS-based direct methanol fuel cells and their stacking using a common electrolyte sandwiched by reinforced microcolumn electrodes," *IEEE International Conference on MEMS 2004,* pp. 65-68.

20. R. O'Hayre, D. Braithwaite, W. Hermann, S.J. Lee, T. Fabian, S.K. Cha, Y. Saito, F.B. Prinz, "Development of portable fuel cell arrays with printed-circuit technology," *Journal of Power Sources,* 124, 2003, pp. 459-472.

21. G. Mozsgai, J. Yeom, B. Flashbart, M. Shannon, "A silicon micromachined direct formic acid fuel cell," *12th International Conference on Solid State Sensors, Actuators and Microsystems, Boston, 2003,* pp. 1738-1741.

22. T.J. Yen, N. Feng, X. Zhang, G.Q. Lu and C.Y. Wang, "A micro methanol fuel cell operating at near room temperature," *Applied Physics Letters,* (83), 19, pp. 4056-4058.

23. Y. Kubo, "Micro fuel cells using carbon nanohorns: A portable power source for a ubiquitous society," International *Symposium on Microelectronics,* 2003 pp. 549-553.

24. E.R. Choban, L.J. Markoski, A. Wiekowski, P.J.A. Kenis, "Microfluidic fuel cell based on laminar flow," *Journal of Power Sources,* 128, 2004, pp. 54-60.

25. H. Qiao, M. Kunimatsu, T. Okada, "Pt catalyst configuration by a new plating process for a micro tubular DMFC cathode," *Journal of Power Sources*, 139, 2005, pp. 30-34.

26. H.S. Young, H.C. Young, "Design, fabrication and characterization of miniature direct methanol fuel cells using platinum-sputtered microcolumn electrodes with limited fuel source," *Sensors and Materials* 16 (6), 2004, pp. 277-289.

27. S.S. Hsieh, C.F. Huang, J.K. Kun, H.H. Tsai, S.H. Yang, "SU-8 flow field plates for a micro PEMFC," *Journal of Solid State Electrochemistry*, 9, 2005, pp. 121-131.

28. J.L. Cohen, D.A. Westly, A. Pechenik, H.D. Abruna, "Fabrication and preliminary testing of a planar membraneless microchannel fuel cell," *Journal of Power Sources*, 139, 2005, pp. 96-105.

29. S.H. Chan, N.T Nguyen, Z. Xia, Z. Wu, "Development of a polymeric micro fuel cell containing laser-micromachined flow channels," *Journal of Micromechanics and Microengineering,* 15, 2005, pp. 231-236.

30. T. Frey, K.A. Friedrich, L. Jorissen, J. Garche, "Preparation of direct methanol fuel cells by defined multilayer structures," *Journal of the Electrochemical Society*, 152 (3), 2005, pp. A545-A551.

31. C.K. Dyer, "Replacing the battery in portable electronics," *Scientific American*, July 1999, pp. 88-93.

32. K.V. Sharp, R.J. Adrian, J.G. Santiago, J.I. Molho, "Liquid flow in micro channels," *The MEMS Handbook,* ed. M. Gad-el-Hak, CRC Press LLC, 2002, London.

33. *Encyclopedia of chemical technology. 4th ed.* Kirk-Othmer.

34. J. Harley, H. Bau, J.N. Zemel, and V. Dominko, "Fluid flow in micron sized channels," *Proceedings of Micro Electro Mechanical Systems*, 1989, pp. 25-28.

35. J. Pfahler, J. Harley, H. Bau, and J.N. Zemel, "Gas and liquid flow in small channels," *Micromechanical Sensors, Actuators and Systems*, Vol. 32, 1991, pp. 49-60.

36. S.M. Flockhart and S.J. Yang "Numerical analysis of fluid flow in channels of micron dimension," *IEE Colloquium on Microengineered Components for Fluids,* 1996, pp. 2/1-2/3.

37. E.R. Arkilic, M.A. Schmidt, and K.S. Breuer, "Gaseous slip flow in long microchannels," *Journal of Microelectromechanical Systems,* Vol. 6, No. 2, 1997, pp. 167-178.

38. E.R. Arkilic, K.S. Breuer, and M.A. Schmidt, "Mass flow and tangential momentum accommodation in silicon micromachined channels," *Journal of Fluid Mechanics,* vol. 437, 2001, pp. 29-43.

39. I. Papautsky, J. Brazzle, T.A. Ameel, and A.B. Frazier, "Microchannel fluid behavior using micropolar fluid theory," *Proceedings of Micro Electro Mechanical Systems,* 1998, pp. 544-549.

40. M. Gad-el-Hak, "the fluid mechanics of microdevices – the Freeman Scholar lecture," *Journal of Fluids Engineering* Vol. 121, March 1999, pp. 5-33.

41. M. Gad-el-Hak, "Flow physics," *The MEMS Handbook*, ed. M. Gad-el-Hak, CRC Press, London, 2002.

42. G.M. Mala and D.Q. Li, "Flow characteristics of water in microtubes," International Journal of Heat and Fluid Flow, 20, 1999, pp. 142-148.

43. H.A. Stone and S. Kim "Microfluidics, basic issues and challenges," *AIChE Journal* Vol. 47, No. 6, pp. 1250-1254.

44. G.T.A. Kovacs, *Micromachined Transducers Sourcebook,* McGraw-Hill, Boston, 1998.

45. P. Argyropoulos, K. Scott, W.M. Taama, "Modeling pressure distribution and anode/cathode streams vapor-liquid equilibrium composition in liquid feed direct methanol fuel cells," *Chemical Engineering Journal*, 78, 2000, pp. 29-41.

46. J.L Xu, P. Cheng, T.S. Zhao, "Gas-liquid two phase flow regimes in rectangular channels with mini/micro gaps," *International Journal of Multiphase Flow,* 25, 1999, pp. 4111-432.

47. M. Lee, Y.Y. Wong, M. Wong, Y. Zohar, "Size and shape effects on two-phase flow patterns in microchannel forced convection boiling," *Journal of Micromechanics and Microengineering,* 13, 2003, pp. 155-164.

48. L. Jiang, M. Wong, Y. Zohar, "Phase change in microchannel heat sink under forced convection boiling," Micro Electro Mechanical Systems, 2000, pp. 397-402.

49. I. Hapke, H. Boye, J. Schmidt, "Flow boiling of water and n-heptane in micro channels," *Microscale Thermophysical Engineering,* 6(2), 2002 pp. 99-115.

50. W. Qu, I. Mudawar, "Prediction and measurement of incipient boiling heat flux in micro-channel heat sinks," *International Journal of Heat and Mass Transfer,* 45, 2002, pp. 3933-3945.

51. C.J. Kim "Microfluidics using the surface tension force in microscale," *Microfluidic Devices and Systems III,* 4077, 2000, pp. 49-55.

52. D. Xu, T.Y. Ng, L.S. Pan, K.Y. Lam, and H. Li, "Numerical simulations of fully developed turbulent liquid flows in micro tubes," *Journal of Micromechanics and Microengineering,* 11, 2001, pp. 175-180.

53. S.Y.K. Lee, M. Wong, Y. Zohar, "Pressure losses in microchannels with bends," *IEEE International Conference on Micro Electro Mechanical System 2001,* pp. 491-494.

54. R. Bradaen, K. Promislow, and B. Wetton, "Transport phenomena in the porous cathode of a proton exchange membrane fuel cell," *Numerical Heat Transfer, Part A,* 42, 2002, pp. 121-138.

55. K. Scott, W.M. Taama, P. Argyropoulos, "Engineering aspects of the direct methanol fuel cell system," Journal of Power Sources, 79, 1999, pp. 43-59.

56. K. Scott, W. Taama, J. Cruickshank, "Performance of a direct methanol fuel cell," *Journal of Applied Electrochemistry,* 28, 1998, pp. 289-297.

57. J. Cruickshank and K. Scott, "The degree and effect of methanol crossover in the direct methanol fuel cell," *Journal of Power Sources*, 70, 1998, pp. 40-47.

58. K. Sundmacher and K. Scott, "Direct methanol polymer electrolyte fuel cell: Analysis of charge and mass transfer in the vapor-liquid-solid-system," *Chemical Engineering Science,* 54, 1999, pp. 2927-2936.

59. A.A. Kulikovsky, J. Divisek, A.A. Kornyshev, "Two-dimensional simulation of direct methanol fuel cell: a new (embedded) type of current collector," Journal of the Electrochemical Society, 147 (3), 2000, pp. 953-959.

60. AA. Kulikovsky, "Numerical simulation of a new operational regime for a polymer electrolyte fuel cell," *Electrochemistry Communications,* 3, 2001, pp. 460-466.

61. J.P Meyers and J. Newman, "Simulation of a direct methanol fuel cell iii: design and optimization," *Journal of the Electrochemical Society*, 149 (6), 2002, pp. A729-A735.

62. J.P. Meyers, and H.L. Maynard, "Design considerations for miniaturized PEM fuel cells," *Journal of Power Sources*, 109, 2002, pp. 76-88.

63. K.T. Jeng and C.W. Chen, "Modeling and simulation of a direct methanol fuel cell anode," *Journal of Power Sources,* 4938, 2002, pp. 1-9.

64. L.B. Rothfeld, "Gaseous counter diffusion in catalyst pellets," *American Institute for Chemical Engineers Journal*, Vol. 9, No. 1, 1964, pp. 19-24.

65. C. W. Hall, *Laws and Models: Science Engineering and Technology*, Boca Raton, CRC Press, 2000.

66. S.J. Farlow, *Partial Differential Equations for Scientists and Engineers*, New York Dover Publications, 1993.

67. D.P. Dewitt *Fundamentals of Heat and Mass Transfer*, New York, John Wiley and Sons, 1996.

68. S.I. Sandler *Chemical Engineering and Thermodynamics*, New York, John Wiley and Sons, 1999.

69. A.J. Smits, *A Physical Introduction to Fluid Mechanics*, New York, John Wiley and Sons, 2000.

70. A.Z. Weber and J. Newman, "Modeling transport in polymer-electrolyte fuel cells," *Chemical Reviews*, 104, 2004, pp.4679-4726.

71. C.Y. Wang, "Fundamental models for fuel cell engineering," *Chemical Reviews*, 104, 2004, pp. 4727-4766.

72. B.R. Sivertsen, N Djilali "CFD-based modeling of proton exchange membrane fuel cells," *Journal of Power Sources*, 141, pp. 65-78.

73. Comsol, AB. *FEMLAB 3.0 Chemical Engineering Module Manual, 2004.*

74. *CIA World Fact Book*, quoted on www.climate-zone.com/climate/united-states

75. *Canadian climatalogical database* quoted on climate.weatheroffice.ec.gc.ca/climate_normals/index_e.html

76. K. Raznjevic *Handbook of Thermodynamic Tables* Begell House, Inc. New York, 1995.

77. J. Larmine and A. Dicks, *Fuel Cell Systems Explained* New York, John Wiley and Sons, 2000.

78. B. Bahar, A.R. Hobson, J.A. Kolde, D. Zuckerbrod, "Ultra-thin integral composite membrane," *U.S. Patent 5,547,551*, 1996.

79. J. Denton, J.M. Gascoyne, G.A. Hards, T.R. Ralph, "Composite membranes," *U.S. Patent 6,042,958*, 2000

80. C. Liu, C.R. Martin, "Ion-transporting composite membranes ii: ion transporting mechanism in Nafion-impregnated Gore-Tex membranes," *Journal of the Electrochemical Society*, 137, 2, 1990, pp. 510-515.

81. C. Liu, C.R. Martin, "Ion-transporting composite membranes iii: selectivity and rate of ion transport in Nafion-impregnated Gore-Tex membranes prepared by a high-temperature solution casting method," *Journal of the Electrochemical Society*, 137 (10), 1990, pp. 3114-3120.

82. M.W. Verbrugge, R.F. Hill, E.W. Schneider, "Composite membranes for fuel cell applications," *AiChE J,* 38, 1992, pp. 93-100.

83. K.M. Nouel and P.S. Fedkiw, "Nafion-based composite polymer electrolyte membranes," *Electrochemica Acta* Vol. 43, 16-17, 1998, pp. 2381-2387.

84. S.H. Kwak, D.H. Peck, Y.G. Chun, C.S. Kim and K.H. Yoon, "New fabrication method of the composite membrane for polymer electrolyte membrane fuel cell," *Journal of New Materials for Electrochemical Systems,* 4, 2001, pp. 25-29.

85. J.S. Jiang, D.B. Greenberg, J.R. Fried, "Preparation of a Nafion composite membrane using a porous Teflon support," *Journal of Membrane Science*, 132, 1997, pp. 273-276.

86. J. Shim, H.Y. Ha, S. A. Hong, I.H. Oh, "Characteristics of the Nafion ionomer-impregnated composite membrane for polymer electrolyte fuel cells," *Journal of Power Sources,* 109, 2002, pp. 412-417.

87. M. Pan, X.S. Yang, C.H. Shen, R.Z. Yuan, "Fiber reinforced sulphinated SBS proton exchange membranes," *Proceedings of the 3rd China Cross-Strait Conference on Composite Materials*, Wuhan, China, May 7-11, 2003, pp. 385-390.

88. M. Yoshitake, E. Yanagisawa, T. Naganuma, "PEMFC Development at Ashahi Glass Co. Ltd." *New Materials for Batteries and Fuel Cells Symposium*, April 5-8, 1999, San Francisco, pp.213-217.

89. F. Liu, B. Yi, D. Xing, J. Yu, H. Zhang, "Nafion/PTFE composite membranes for fuel cell applications," *Journal of Membrane Science,* 212, 2003, pp. 213-223.

90. K. Stanley, E. Czyzewska, L. Fan, J. Wu, A. Parameswaran, "A novel micro fuel cell topology for high speed manufacturing," *Small Fuel Cells 2004*, Washington DC.

91. Q. Deng, C. A. Wilkie, R. B. Moore, K. A. Mauritz, "TGA-FTIR investigation of the thermal degradation of Nafion® and Nafion®/[silicon oxide]-based nanocomposites," *Polymer*, 39 (1998) pp. 5961.

92. S. K. Tiwari, S. K. Nema, Y. K. Agarwal, "Thermolytic degradation behavior of inorganic ion-exchanger incorporated Nafion-117," *Thermochimica Acta*, 317 (1998) pp. 175

93. S. Koter, P. Piotrowski, J. Kerres, "Comparative investigations of ion-exchange membranes," *Journal of Membrane Science*, 153, 1999, pp. 83-90.

94. *DuPont Nafion PFSA Membranes N-112, N3-1135, N-115, N-117, NE-1110 Perfluorosulfonic Acid Polymer,* Product Information, NAE 101, DuPont Fluoroproducts, 2004.

95. *DuPont Nafion PFSA Membranes NRE-211 and NRE-212 Perfluorosulfonic acid polymer*, Product Information NAE201, DuPont Fluoroproducts, 2004.

96. Allen J. Bard, Larry R. Faulkner, *Electrochemical Methods: Fundamentals and Applications*, New York, Wiley, 2001.

97. O.J.A. Schueller, D. C. Duffy, J.A. Rogers, S.T. Brittain, G.M. Whitesides, "Reconfigurable diffraction gratings based on elastomeric microfluidic devices," *Sensors and Actuators A* 78, 1998, pp. 149-159.

98. Abel, K; Navessin, T.; Xie, Z.; Shi K.; and Holdcroft, S. *Evaluation of MEA for Micro Fuel Cell Based on Patents (U.S. 2004/0053100 A1 and U.S. Provisional Patent 60/565,834*, Technical Report-NRC-IFCI.